SINGLE MOLECULE DETECTION ON THE CELL MEMBRANE

WITH

NEAR-FIELD SCANNING OPTICAL MICROSCOPY

Promotiecommissie:

prof. dr. P. J. Kelly (voorzitter)	University of Twente
prof. dr. N. F. van Hulst	University of Twente
dr. M. F. García-Parajó	University of Twente
dr. T. M. Jovin	Max Planck Institute for Biophysical Chemistry
prof. dr. Th. Schmidt	Leiden University
prof. dr. C. G. Figdor	Nijmegen Center for Molecular Life Sciences
prof. dr. V. Subramaniam	University of Twente
prof. dr. ing. D. H. A. Blank	University of Twente

The work described in this thesis has been financially supported by the Technology Foundation STW of the Netherlands (Grant no. TTN.4821).

The research was carried out in the group
Applied Optics, Faculty of Science & Technology
MESA$^+$ Institute for Nanotechnology
University of Twente
P.O. Box 217, 7500AE Enschede
the Netherlands.

Cover: Near-field fluorescence image of a dendritic cell
containing Cy5-labeled DC-SIGN proteins.

ISBN: 90-365-2019-3
Printed by: Febodruk BV, Enschede, the Netherlands.

SINGLE MOLECULE DETECTION ON THE CELL MEMBRANE

WITH

NEAR-FIELD SCANNING OPTICAL MICROSCOPY

PROEFSCHRIFT

ter verkrijging van
de graad van doctor aan de Universiteit Twente,
op gezag van de rector magnificus,
prof. dr. F.A. van Vught,
volgens besluit van het College voor Promoties
in het openbaar te verdedigen
op vrijdag 19 maart 2004 om 15.00 uur

door

Bärbel Irene de Bakker

geboren op 16 april 1975
te Heerlen

Dit proefschrift is goedgekeurd door:
prof. dr. N. F. van Hulst (promotor)
dr. M. F. García-Parajó (assistent promotor)

voor Edwin,
voor mijn ouders

Contents

Chapter 1

Introduction

High resolution imaging techniques have been essential for advances in cellular and molecular biology. In particular fluorescence microscopy, providing (bio)chemical contrast in living cells, and scanning probe microscopy, providing structural information at the nanometer scale, are widely used. Near-field scanning optical microscopy (NSOM) unites the best of both techniques. The high spatial resolution provided by NSOM bridges the gap between the diffraction limited resolution of far-field microscopy ($\sim 300\,\mathrm{nm}$) and the distance resolution provided by fluorescence resonance energy transfer (FRET) ($< 10\,\mathrm{nm}$). In addition, NSOM allows single molecule detection even in densely packed areas. The properties of this technique enable investigation of the spatial organization of molecules at the cell membrane, i.e. the distribution, size and contents of molecular domains, in a quantitative way. This chapter presents an overview of high resolution microscopy techniques with a main focus on fluorescence microscopy and optical single molecule detection in (cell) biology. A general description of NSOM as well as a short description of the biological system under study is given, concluding with an overview of the thesis.

1.1 Microscopy and cell biology: histories in parallel

Cells, the building blocks of living organisms were described for the first time in 1665 by Robert Hooke as small elements in a slice of cork [1]. His observation was the result of the technological development of the optical microscope, which started 60 years earlier. Due to major improvements in the art of lens making, Zacharias Janssen developed one of the first compound microscopes that could magnify up to 10 times in 1590 [2–4]. In the decades after Hooke's observation, Antoni van Leeuwenhoek made many biological discoveries, e.g. observation of bacteria, living organisms in a drop of water, sperm and blood cells [4]. In the following centuries the resolution of optical microscopes improved mainly due to technological progress in glass and lens making. However, theoretical work by Abbe (1875) and Rayleigh (1879) showed that the resolution in lens-based optical microscopy is fundamentally limited by the wavelength of the light being used, i.e. the diffraction limit. Aiming at a better resolution by decreasing wavelength, the first UV microscope was developed at Zeiss by August Köhler in 1904. Soon, the (auto)fluorescence emission of cells was visualized, the first steps of fluorescence microscopy [5].

Fluorescence microscopy has become the most common imaging technique in cell biology, due to the many advantages intrinsic to light. First, it enables the study of living specimens in their native environment in a non-invasive and non-destructive way [6]. Second, it enables (bio)chemical contrast. For example, fluorescence intensity, fluorescence lifetime and polarization provide information about the conformation and movement of fluorophores as well as about their surroundings, i.e. other molecules, viscosity, oxygen concentration or pH. Third, it is a fast technique that provides time resolution down to picoseconds allowing the monitoring of phenomena such as conformational changes, binding reactions and molecular interactions [7].

Nevertheless, the spatial resolution barrier inherent in light microscopy encouraged the development of other imaging techniques such as electron microscopy (EM) [8] in 1930, and scanning probe microscopy (SPM) in the 1980s [9]. With a sublime resolution of less than one nanometer and a magnification up to one million times EM has brought an enormous amount of knowledge about cells and intracellular structures, e.g. mitochondrion, endoplasmic reticulum and cell membrane [10]. However, EM has major drawbacks as it requires dried, dead specimens and visualizes static snapshots of the cell structure or cellular processes in arrest. Moreover, the severe sample preparation, e.g. fixation and sample slicing [10], can lead to structural artifacts [11]. Living biological specimens can be studied at high resolution ($\sim 10\,\mathrm{nm}$) with atomic force microscopy (AFM), a member of the SPM family [12, 13]. This technique, invented in 1986 [14], has revealed many unique aspects of living cells, e.g. the surface structure of living spores [15, 16] and endothelial cells [17] as well as the dynamic behavior of the cytoskeleton in living cells [18, 19] and mechanical pulsing of cardiomyocytes [20]. Because AFM imaging is based on force interactions between the probe and specimen, the number of obtainable contrast mechanisms is limited. A promising development to increase contrast is functionalization of the AFM tip with adhesive [21, 22] or fluorescent molecules [23]. In this way, AFM has been used to image various biophysical cell surface properties such as hydrophobicity [24], visco-elasticity [25, 26] and adhesion [27, 28], allowing local recognition of specific molecules.

Properties of both SPM and fluorescence microscopy are united in near-field scanning optical microscopy (NSOM or SNOM), developed in the 1980s [29]. This technique provides simultaneous structural information with nanometer optical resolution, while preserving all optical contrast possibilities. The research reported in this thesis concerns the aperture-type NSOM [30], in which a probe with a subwavelength sized aperture (typically 70 - 120 nm) is scanned in the near-field ($< 10\,\mathrm{nm}$) of the sample [31, 32]. The probe illuminates the sample with an evanescent field which is strongly localized at the vicinity of the aperture and decreases rapidly away from the probe's end face [31, 33]. Due to the exponentially decaying character of the illumination field NSOM is a surface sensitive technique, and is therefore ideal for studying the cell membrane [34–39].

In 1993, NSOM allowed for the first time detection of fluorescence from individual molecules at room temperature [40]. Since then, single molecule NSOM has provided information about the relative positions of fluorescent molecules with respect to the overall structure on various biological specimens [34, 37, 41, 42]. Optical single molecule detection has nowadays become a well established technique in both near- and far-field microscopy. However, only NSOM has the added values of a high spatial resolution below the diffraction limit and a small penetration depth of the illuminating light. In this thesis NSOM has been exploited to study fluorescently labeled proteins with a high local density on the membrane of intact cells. The small penetration depth enables detection of single molecule fluorescence on a densely packed cell. Moreover, the high spatial resolution of NSOM allows to distinguish individual entities, which would not have been resolvable by diffraction-limited techniques.

1.2 Fluorescence microscopy, biology towards the nanometer scale

Initially, in the first decades of the 20th century, UV microscopy was limited to visualization of autofluorescent components within cells, e.g. vitamins like ascorbic acid and riboflavin and organic compounds like chlorophyll [43]. The number of specimens under study increased dramatically with the invention of fluorescent labeling of tissue components and bacteria using fluorophores by Max Haitinger (1933) [44] and later by antibody staining as introduced in 1941 by Albert Coons [45]. An important and more recent development is the exploitation of natural fluorescent proteins [46], e.g. green (GFP), blue (BFP), cyan (CFP), yellow (YFP) and red (DsRed) fluorescent protein. The isolated gene for the autofluorescent protein is fused to the DNA encoding for the target protein to produce a chimeric DNA structure. As living cells can produce the chimeric target protein, this is a powerful method which allows optical investigation of expression and dynamics of proteins in living cells with minor perturbation of the biological system [46–49].

Amongst all fluorescence microscopy techniques to investigate biological specimens, epifluorescence and confocal microscopy are most common due to their ease of use. In wide-field epifluorescence microscopy (Figure 1.1 a,) the sample is illuminated over a large area, $\sim 100 \times 100\,\mu\text{m}^2$.

The spatial resolution in wide-field microscopy is given by Rayleigh's criterium:

$$d = 0.61 \cdot \frac{\lambda}{NA} \tag{1.1}$$

where d is the distance between two point sources in the object plane, λ is the wavelength of the fluorescent light and NA is the numerical aperture of the lens system. Optical slice thickness is not definable in epifluorescence microscopy as object information from the focal plane is mixed with blurred information from out-of-focus object regions.

The negative effect of out-of-focus light on the image is reduced using confocal microscopy. The principle of confocal microscopy is shown in Figure 1.1 b, where light is focused on the sample by a high NA objective, with confocal alignment of the illumination spot and point detector. The spatial resolution in confocal microscopy is higher than obtained in wide-field microscopy:

$$d = 0.44 \cdot \frac{\lambda}{NA} \tag{1.2}$$

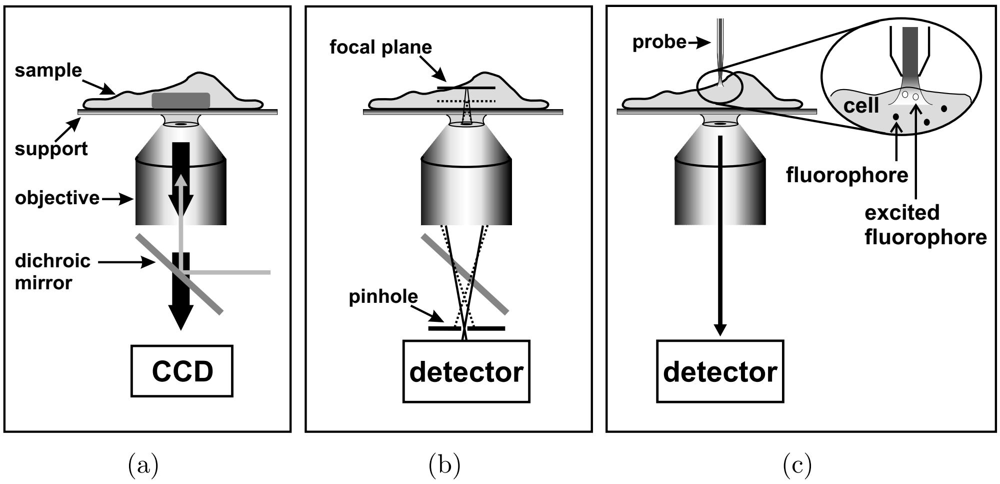

(a) (b) (c)

Figure 1.1: Schematic of different fluorescence microscopes. (a) Epifluorescence microscopy. Light from a laser or arc lamp is reflected by a dichroic mirror and focused onto the back-focal of an objective, acting as condenser. The objective collects the fluorescence, which is transmitted by the dichroic mirror, filtered and then detected by a two-dimensional array detector, e.g. CCD. (b) Confocal microscopy. Excitation light is collimated, reflected by a dichroic mirror and focused onto the sample (path not shown). Fluorescence, from the focal plane (solid line) and from out-of-focus regions (e.g. dotted line), is collected by the same objective, filtered and detected by a detector, e.g. an Avalanche Photodiode (APD) or Photomultiplier Tube (PMT). (c) Near-field scanning optical microscope. The probe illuminates the sample in the near-field, while the sample is scanned underneath the probe. Fluorescence is collected in the far-field by a high NA objective, filtered and detected on a detector, e.g. APD.

Along the optical axis the resolution criterium is given by:

$$d_z = \frac{0.88\lambda}{n - \sqrt{n^2 - NA^2}} \tag{1.3}$$

where n is the index of refraction of the medium. Because the sample is locally illuminated, an image is created by scanning the laser beam over the sample. A confocal microscope also makes use of a detection pinhole that rejects out-of-focus light and enables imaging of thin sections from thick specimens and thus 3D visualization of the interior of cells [50–53].

Recently, a number of approaches have been developed with the aim to improve the optical resolution by reducing the confocal illumination volume, such as multi-photon microscopy (MPM) [54, 55], 4Pi confocal [56] and stimulated emission depletion (STED) microscopy [57, 58]. All of them have specific advantages and disadvantages. For example, the improved axial resolution of MPM is particularly suitable for thick specimens [52, 55]. However, MPM can be harmful for living cells because the illumination intensities used are much higher than in single photon microscopy [58]. 4Pi confocal microscopy has an improved axial resolution below 100 nm, which is a significant improvement with respect to regular confocal microscopy, providing high resolution 3D images of fixed [59] and living cells [60, 61] as well as complete tissues [62, 63]. However, its versatility is limited as it is technically complicated. This is also the major drawback for STED, where the effective confocal illumination spot is decreased six-fold in axial and two-fold in lateral direction, resulting in a nearly spherical spot of 100 nm diameter [64].

A successful method to gain contrast at an even smaller (nanometer) scale than the above described far-field fluorescence techniques is Förster or fluorescence resonance energy transfer (FRET) [65, 66]. FRET is the electromagnetic dipole-dipole interaction between nearby fluorophores in which the optically excited donor transfers its energy non-radiatively to a nearby acceptor, which then fluoresces. The efficiency of the energy transfer is strongly dependent on the donor-acceptor separation ($\sim \mathrm{r}^{-6}$). This distance dependent process occurs in the range of 1 - 10 nm and can be visualized with any fluorescence microscopy method. FRET is an excellent contrast method to study biological processes in the nanometer regime and used widely in biology for measuring proximity of molecules, protein conformational changes, structural changes and binding events [67–69].

Many cellular processes occur at the scale from a few to several hundreds of nanometers [37]. Unfortunately, there is a gap in resolvable distances between FRET ($<$ 10 nm) and regular confocal microscopy ($\sim$ 300 nm). NSOM provides visibility in this otherwise "blind" region, bridging the gap with a resolution of typically 100 nm. Figure 1.1 c shows the principle of NSOM. The heart of the near-field optical microscope is the near-field probe that interacts with the sample at nanometer distance and determines contrast, resolution and sensitivity. Although there are various operation modes possible [31, 70], this thesis focuses on NSOM operation in illumination mode, where the sample is illuminated through a subwavelength aperture at the end of the probe. The most widely used probe type is the adiabatically tapered, aluminum coated optical fiber [71, 72]. The distance regulation, to keep the probe in the near-field of the sample ($\sim$ 10 nm), is provided by a feedback mechanism based on shear force between probe and sample [33, 73]. A near-field image is created by scanning the sample underneath the probe. During scanning, the feedback signal, related to the surface topography, and the optical (fluorescence) signal are recorded simultaneously. The high resolution of NSOM is specifically interesting for cell biology as is demonstrated by localization studies of different types of proteins on fixed cells at a spatial resolution of $\sim 100\,\mathrm{nm}$ [37, 39, 74–78]. In particular, the combination of FRET and NSOM is powerful to investigate close molecular proximity, e.g. resolving distances within molecular domains, in combination with a high spatial resolution, e.g. resolving domain dimensions beyond the diffraction limit [79].

1.3 Single molecule detection

While cells are building blocks of life, molecules are the building blocks of cells. Therefore, in addition to a high spatial resolution, the ideal microscopy technique for cell biology should be able to resolve individual molecules. In the last years, several techniques to identify single biomolecules have been developed, such as optical tweezers [80–82] and AFM to measure forces [83–87], optical microscopy to measure fluorescence emission [88–95] and EM and patch-clamp-like techniques to measure electronic properties [96, 97]. This thesis focuses on the optical detection of single molecules on the cell membrane.

The power of single molecule detection lies in the capability to investigate molecular properties that are normally averaged out, and therefore hidden, in bulk experiments. Single molecule studies reveal information about the interaction of the molecule with its (nano)surroundings and the local heterogeneity of the sample. In particular, molecular reactions that are usually not synchronized can be uncovered with this technique [88–90, 93, 94, 98].

The most difficult aspect of single molecule detection is to ascertain the weak single molecule signal from the surrounding background. This is particularly critical for single molecule detection on cells, where cellular autofluorescence originating from natural fluorophores [43, 93, 99] interferes strongly with the single molecule signal. In this research, proteins on human cells were examined by single molecule detection, setting specific experimental requirements. First, the specific fluorescence signal had to be distinguished from light coming from the molecule's environment, e.g. scattered light and fluorescence. This demanded the use of dyes with suitable photo-physical properties, i.e. large absorption cross section, high quantum yield and a large Stokes shift between absorption and emission spectra. As most autofluorescent compounds in mammalian cells can be excited in the near UV and blue region of the spectrum ($< 500\,\mathrm{nm}$), it is preferable for single molecule detection to use fluorescent labels that can be excited at longer wavelengths, i.e. $> 550\,\mathrm{nm}$. Second, to detect the weak signal from a single molecule, sensitive detectors such as avalanche photodiodes (APDs) and intensified CCDs are commonly used [93, 94]. Third, the molecular density should be such that only one molecule is contained within the excitation volume. Because cells are densely packed molecular systems, the illumination volume has to be minimized in order to excite one molecule at the time. An alternative, though less desirable way to achieve excitation of one molecule in the illumination spot is by labeling only a low concentration of molecules or by bleaching the majority of the high concentration fluorescent molecules, leaving a low concentration for single molecule detection.

1.3.1 Optical single molecule studies on cells

Wide-field epifluorescence microscopy is being increasingly applied for single molecule detection in living cells. The main advantage of the technique resides in the time resolution (in the order of 5 ms) which allows the monitoring of dynamic processes in real time. Therefore, epifluorescence has been used to observe protein diffusion [100] and mobility of ion channels [101] and phospholipids [102] in free-standing lipid membranes, thus avoiding background from intracellular autofluorescence. Unfortunately, epifluorescence microscopy can only be used to study biological systems where the concentration of molecules under study is sufficiently low ($< 2.7\,\mathrm{molecules}/\mu\mathrm{m}^2$). For example, a labeling ratio of $1:10^4$ labeled : unlabeled proteins was used to monitor the translational motion of proteins in the plasma membrane of a living cell, resulting in a maximum of 0.3 labeled molecules/μm^2 [103]. Trajectories of a low concentration of single proteins could be visualized inside a living cell [104, 105] as well as entry of virus particles into a cell [106]. By bleaching the sample prior to measurement, *in vivo* experiments of oligomerization and diffusion of single YFP-tagged Calcium channels on HEK293 cells could be performed [107]. Thus, although dynamic processes in living cells can be monitored, the application of epifluorescence microscopy on cells is limited and requires special treatment of the specimen to decrease the concentration of fluorescent molecules.

Due to the small illumination volume of confocal microscopy ($\sim 10^8\,\mathrm{nm}^3$) it has become an important tool in single molecule biophysics. In particular, confocal microscopy combined with single pair FRET is being widely used for *in vitro* studies of molecules under physiological conditions. [66, 98, 108–115]. Because scanning over a cell is too slow to study single molecular dynamics and diffusion [116], often the detection volume is not scanned, but kept fixed at a particular location of the sample. Diffusion, mobility, as well as association rates of intramolecular reactions of molecules can be detected in this way, as every fluorescent molecule that passes the volume emits a burst of photons during its transit [117–121].

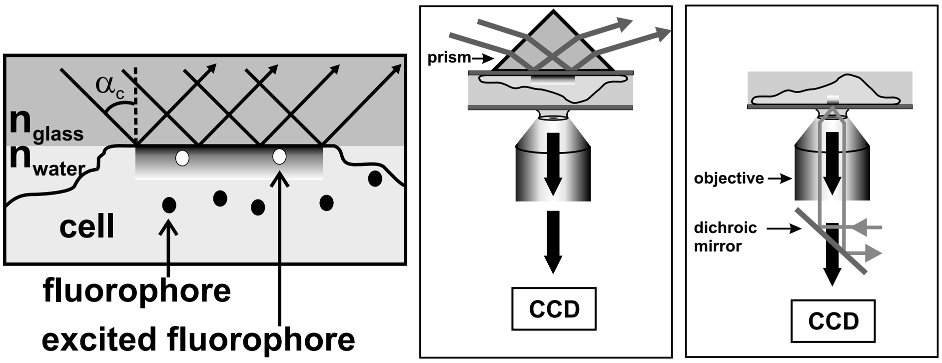

(a) (b) (c)

Figure 1.2: (a) Principle of total internal reflection microscopy (TIRFM). Light, traveling through an optical dense medium is incident at the interface between two media of different refractive indices ($n_{water} = 1.33$ and $n_{glass} = 1.52$) at an angle (α) that is larger than the critical angle of refraction (α_c). At this angle, the light is totally reflected by the interface. The evanescent field, generated at the interface, penetrates into the medium of lower refractive index and decreases exponentially with the distance from the interface. Two ways to achieve an angle larger than the critical angle are by using a prism (b) or an objective (c).

As the penetration depth of confocal microscopy is still on the order of the wavelength used, background from cellular autofluorescent components is a problem in single molecule confocal microscopy. A successful technique to reduce the intracellular background and a common method to image single molecules on living cells is total internal reflection fluorescence microscopy (TIRFM). This near-field technique employs an induced evanescent field to selectively illuminate and excite fluorophores in a sample region immediately adjacent to a glass-water interface as is shown in Figure 1.2(a).

The evanescent wave can be created either by using a prism or an objective as shown in Figure 1.2 [122–124]. In both cases the fluorescence is collected by an objective, filtered and focused onto a CCD camera. Wide-field TIRFM is less prone to the effects of cellular autofluorescence compared to wide-field epifluorescence due to the shallow (< 100 nm) penetration depth [95]. This is also the reason why the first observations of single biomolecules in aqueous solution, showing a single kinesin motor walking along a microtubule, were performed with TIRFM [125]. The technique is being used in many single molecule studies, e.g. studying fusion of vesicles in the membrane [124], diffusion of membrane bound molecules [126], dynamics of phosphorylation, protein oligomerization in the plasma membrane of living cells [91, 127–129], and 'real time' visualization of single protein dynamics on the cell membrane using organic fluorophores [130] and autofluorescent proteins [129, 131]. As TIRFM is a diffraction limited technique, low concentration samples must be used in order to distinguish single molecules. Moreover, TIRFM imaging is restricted to the interface between a high and a lower refractive index. In fact, the evanescent field is created at the side where the cell is fixed to the glass substrate, which might hinder dynamical processes and introduce artifacts in the functioning of the cell (membrane) under study. An additional disadvantage of TIRFM is the fact that the local excitation intensity per molecule may vary as the membrane/substrate contact distance can vary tens of nanometers, making it hard to perform quantitative analysis [132].

1.3.2 Near-field Scanning Optical Microscopy on cells

NSOM preserves the advantages of the near-field excitation, without having the restrictions of TIRFM. Because of the high spatial resolution and small penetration depth, the excitation volume provided by NSOM is the smallest compared to other optical techniques, e.g. $\sim 10^5\,\mathrm{nm}^3$ NSOM excitation volume versus $\sim 10^8\,\mathrm{nm}^3$ obtained with confocal microscopy. This is particularly useful in reducing intracellular autofluorescence background and in observing closely packed molecules (at best 100 molecules/μm^2). Yet, single molecule studies on complete cells using NSOM have not been reported so far, mainly due to: 1) the complexity of the technique, which requires reliable and reproducible probe fabrication and accurate control of sample-probe distance. 2) the slow frame rate, which is inherent to scanning probe techniques. 3) the fact that NSOM does not work reliably under liquid conditions. The most relevant results of NSOM studies on cells include fluorescence imaging of cytoskeletal actin on fixed mouse fibroblast cells [78], (co-)localization of host and malarial proteins on malaria-infected cells [76], imaging of membrane lipids and proteins on fibroblasts, both dried and in saline [75, 133] and visualization of lectins binding to cell surface proteins [74]. Two of the few NSOM studies under liquid conditions have been performed on antibody-labeled nuclear pore complexes visualized on an isolated nucleus membrane [134] and on fluorescently labeled human leukocyte antigens present on fibroblast cells [135].

1.4 Immunology in a nutshell

The objective of the work described in this thesis has been to exploit NSOM for the study of two different protein systems at the single molecular level on the cell membrane. The examined proteins are related to the immune system. Therefore, an introduction to the human immune response is given to familiarize the reader with applicable terminology.

The first line of defense in the human body

The human immune system is a sophisticated mechanism to protect the human body against pathogens like bacteria, viruses and fungi that can cause diseases. All humans are born with a fast first line barrier and defense mechanism that acts non-specifically against foreign, sometimes harmful, materials and micro-organisms: the innate immune system. To prevent entry of pathogens there are physical barriers like the skin, antibacterial substances in secretions like stomach acid and reflexes for mechanical removal of microbes from the body like coughing and sneezing. Micro-organisms that have overcome these barriers (Figure 1.3 a) are likely to be ingested by specialized cells called phagocytes (Figure 1.3 b), such as macrophages, neutrophils and dendritic cells (DCs). These cells recognize pathogens using cell-surface receptors and then ingest and degrade the pathogen. Fever and inflammation, i.e. accumulation of body fluids to drive immune cells to the site of infection, are other protective mechanisms of the innate immune response (Figure 1.3 c).

The adaptive immune system

DCs are particularly important immune cells since they are most efficient in activation of the adaptive immune system [136]. In contrast to the innate mechanism, adaptive immune processes are pathogen-specific and therefore efficient in pathogen elimination. A DC can bind to pathogens or their products using receptors present on the DC membrane. After binding, the DC internalizes the pathogen (phagocytosis) or the pathogenic material (pinocytosis), as shown in Figure 1.3 d. The internalized material is degraded into peptide fragments. These fragments bind to major histocompatibility complex (MHC) proteins that carry them to the cell surface (see Figure 1.3 e), the process to which the DC owes its designation of antigen presenting cell (APC).

Adaptive immune responses for elimination of intruders are carried out by B and T lymphocytes, also named B and T cells. Both B and T cells have receptors for specific antigens and exhibit unique ways of fighting pathogens. The adaptive

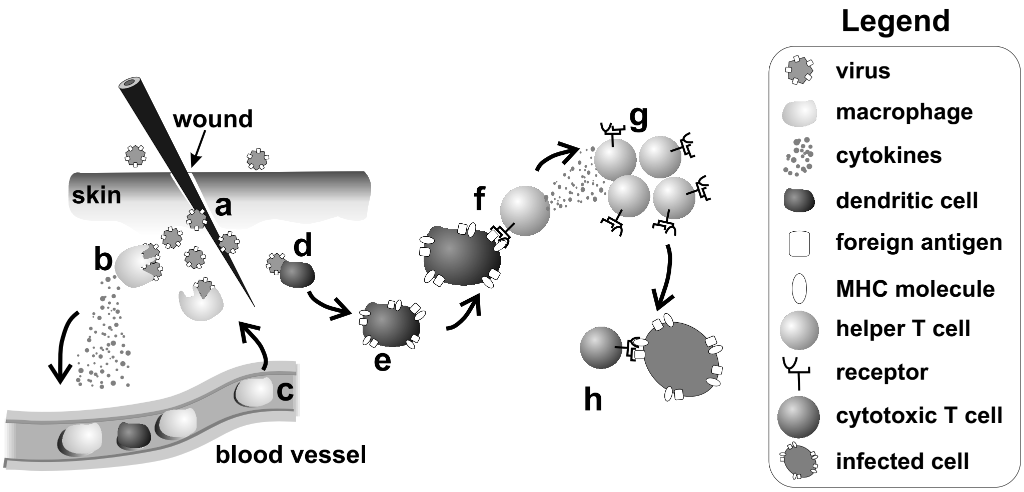

Figure 1.3: Immune response. a) Pathogens enter the body through a wound in the skin. b) Macrophages ingest and kill pathogens, and release cytokines to induce inflammation. c) Immune cells are driven to site of infection. d) Dendritic cells (DC) ingest pathogens e) and display pathogenic material together with MHC molecules on surface. f) A naïve helper T cell recognizes antigens presented by a DC and is activated to become an effector helper T cell. g) Upon activation, the helper T cell produces cytokine (IL-2) causing itself and other T cells to proliferate. h) A cytotoxic T cell, stimulated by helper T cells, travels to site of infection and targets a viral infected cell, presenting the same antigen in an MHC molecule on its surface. The infected cell is directly killed.

immune responses are initiated by activation of so called naïve B and T cells, i.e. cells that have never encountered their specific antigen. We will focus here on T cells. DCs can activate two types of naïve T cells, i.e. helper and cytotoxic T cells[1], which then become effector cells or memory cells. For example, Figure 1.3 f shows the activation of a naïve helper T cell by a DC, i.e. the T cell recognizes the pathogenic peptides presented on the DC membrane. Then the T cell stops migrating and releases cytokines that are bound by specific cytokine receptors at the T cell membrane, followed by proliferation of activated helper T cells as shown in Figure 1.3 g. These cells help cytotoxic and other cells to fight the infection, as shown in Figure 1.3 h. Upon proliferation, also memory helper T cells are formed, which can easily and quickly be triggered to become effector

---

[1] Helper T cells stimulate other cells for pathogen elimination, while cytotoxic T cells directly eliminate pathogens. Helper and cytotoxic T cells are distinguished by surface proteins CD4 and CD8, respectively. Therefore, the distinct forms of naïve, memory or effector cells are often denoted as CD4 naïve T cel, CD8 naïve T cell, etcetera.

cells in a later encounter with the same antigen. Memory cells can live for a human lifetime and give rise to either effector cells or more memory cells after activation. This ensures that when a specific infection occurs for the second time, the immune system is faster and more efficient in the elimination of the pathogen.

Cell binding plays an important role during both innate and adaptive immune processes, e.g. in the uptake of pathogens by DCs and the activation of naïve T cells by antigen presenting cells. There are many different membrane receptor molecules that mediate cell binding. Both the expression level of specific receptors at the cell membrane and their spatial organization are important parameters that determine the binding properties of a cell. The high molecular packing of the cell membrane requires a high resolution technique to visualize and investigate the nanoscale distribution of membrane molecules. In this thesis, the spatial organization of two types of immune receptors have been investigated with NSOM on intact cell membranes at the single molecular level, i.e. 1) DC-SIGN, a transmembrane protein on the membrane of immature DCs. DC-SIGN binds to surface proteins of several viruses and microbacteria, enabling pathogen uptake by DCs, as schematically shown in Figure 1.3 d. 2) Cytokine specific Interleukin receptors IL-2R and IL-15R on the membrane of activated T cells. IL-2R and IL-15R bind to Interleukins IL-2 and IL-15, respectively. Upon binding, the T cell is signaled to perform a specific cell function such as differentiation, proliferation or to induce activated cell death. Therefore, these cytokine receptors play an active role in the T cell development after activation, i.e. step *g* in Figure 1.3. More extensive introductions to DC-SIGN and Interleukin receptors IL-2R and IL-15R are given in Chapter 3 and Chapter 6, respectively.

1.5 Thesis overview

Recently, biological interest has grown as to the heterogeneity and structure of the cell membrane in relation to cell functioning [137]. The existence of functional domains is an issue under extensive discussion, partly because of contradictory observations [138] and the differences in measured domain sizes, which have been reported to vary from $< 10\,\mathrm{nm}$ to the micrometer scale [36, 139].

In this thesis, single molecule studies on the membrane of intact, dried and fixed cells are presented. The high spatial resolution of NSOM enables distinction of molecular domains as well as single molecules on the membrane. Single molecule analysis has been used to elucidate domain properties of two different protein systems. Recently, our NSOM has proven to be successful for cell imaging under liquid conditions [140], which in combination with autofluorescent proteins will enable future optical high resolution studies on living cells.

In Chapter 2, the technical details of the combined near-field/confocal scanning optical microscope, developed during the course of this work, are discussed. An overview of the microscope is given, as well as a short description of the individual components. Then, the general performance of the microscope in terms of sensitivity, spatial resolution and localization accuracy is discussed, using optical measurements on fluorescently labeled cells as examples.

Chapter 3 is dedicated to the near-field study of the spatial organization of pathogen recognition receptor DC-SIGN on the membrane of intact immature dendritic cells. Using single molecule sensitivity, the local molecular density of DC-SIGN on the cell membrane is examined in a quantitative manner.

In Chapter 4, the specific spatial DC-SIGN organization, which is discovered in Chapter 3, is brought in connection to the adhesion function of immature dendritic cells. Using Monte Carlo simulations, the influence of the spatial organization on the cell's adhesive properties is investigated.

In Chapter 5, more quantitative aspects of single molecule detection are shown. Irreversible photobleaching is exploited to accurately count the number of closely packed molecules. This method is used to determine the dye-to-antibody ratio of Cy5-labeled antibodies. In a second study, a densely packed area on a cell surface is sequentially imaged while photobleaching, which allows to pin-point the remaining fluorescent molecules within the fluorescence depleted area.

In Chapter 6, the spatial organization of a second molecular system is investigated, i.e. Interleukin receptor subunits IL-2Rα and IL-15Rα on activated T cells. Using similar methods as in Chapter 3, the local molecular density of these molecules is revealed, showing domain formation for both types of protein. Moreover, the relative organization and correlation of the two molecules is investigated using dual color excitation and detection NSOM.

Chapter 2

Instrumentation

A combined near-field and confocal scanning optical microscope has been developed for the optical investigation of biological specimens at high resolution and with single molecule sensitivity. The combination of bright wide-field, confocal (fluorescence) and near-field scanning optical microscopy permits zooming in step by step on a sample going from hundreds of micrometers to the nanometer scale. Some practical examples are discussed, giving insight into the performance of the microscope.

2.1 Confocal & near-field optical microscope

2.1.1 Microscope properties

Near-field scanning optical microscopy (NSOM) is a valuable technique for biological studies requiring high optical resolution, surface sensitivity and/or correlated topographic information at the nanometer scale [34, 35, 37, 133]. Here we focus on the development and utilization of an optical microscope for the study of biological specimens at the single molecular scale with a high spatial resolution.

Several properties have been taken into account in the design of the microscope: 1. step by step zoom in on a specific location of the sample, using bright field, confocal and NSOM imaging modes. 2. easy and reversible interchange between the various modes of operation. 3. full compatibility with other commonly used microscopy techniques in biology, e.g. fluorescence correlation spectroscopy and fluorescence resonance energy transfer. 4. possibility to integrate a liquid cell and temperature controller for investigation of the specimen under native conditions. Figure 2.1 shows an overview of the actual set-up with its most important parts highlighted.

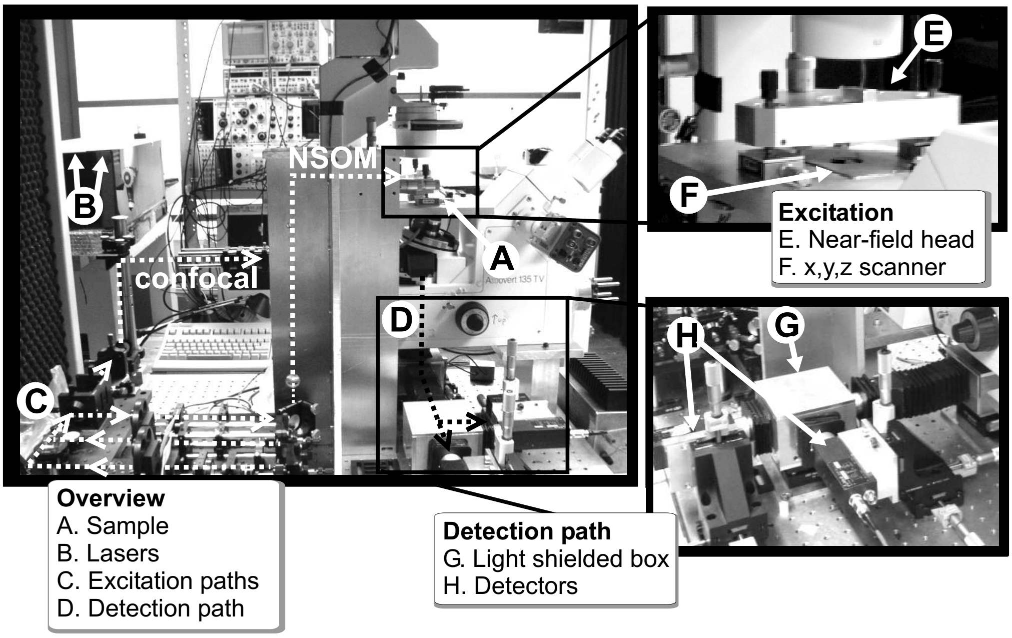

Figure 2.1: Overview of the complete near-field & confocal scanning optical microscope. The white/black dashed lines illustrate the optical excitation/detection paths.

2.1.2 Description of the microscope

The experimental set-up is integrated into an inverted optical microscope (Zeiss Axiovert 135 TV). Instead of the commercial microscope sample stage, a solid Al plate equipped with an x,y,z scan stage with a range of 40×40×26 μm

(NanoCube^{TM}, Physik Instrumente (PI), Germany) has been installed. The scanner is linearized and stabilized (drift $\sim$1 nm/min) using a lateral position feedback system. The set-up allows two modes of operation for fluorescence microscopy, i.e. far-field excitation (confocal mode) and near-field excitation, using one or two excitation wavelengths simultaneously and two detection channels.

The scheme of the microscope is shown in Figure 2.2. The microscope has access to two Ar^+/Kr^+ ion lasers, providing a wide wavelength range (457 - 647 nm). Laser light enters the set-up via two independent optical paths (a and b). Broadband polarizing components (P) in both paths allow independent control of the polarization for each beam. The beams are combined by the beam splitter. Flippable mirror M_2 allows easy and reversible switching between confocal and near-field illumination. For far-field excitation the light is guided through a short piece of single mode fiber ($\sim$5 cm) (F) that acts as a spatial filter and guarantees full overlay of two wavelengths. The fiber core ($\sim$3.4 μm) can be considered as a point source for the confocal microscope. Objective L_3 couples the light out of the fiber and expands it to a diameter of $\sim$5 mm to fill the back of the main objective (O). The near-field excitation path is discussed in more detail below.

Fluorescence is collected with a high NA objective (O), filtered from the excitation wavelength using long-pass filters (F_2 - F_4), and separated in two channels, either orthogonally polarized or spectrally separated. The detection path is shielded by flexible light-tight bellows and a light-tight box that holds filters and beam splitter components. The universal mount in the box allows easy interchange between polarization cube and dichroic mirror. Two photon-counting avalanche photodiodes (APDs) are confocally aligned with either the confocal illumination focus or the near-field probe aperture.

2.1.3 Near-field microscopy

This thesis focuses on an aperture-type near-field scanning optical microscope working in illumination mode, i.e. the near-field aperture probe acts as a subwavelength light source [31, 141]. The probes, based on single mode optical fibers (single mode at $\lambda = 633$ nm, Cunz GmbH & Co., Frankfurt, Germany), were fabricated using the "heating-and pulling" method [31, 72, 142, 143]. Tapered probes were then coated with a thin ($\sim$1 nm) chromium adhesion layer, followed by an aluminum layer ($\sim$100 nm) in order to confine the light within the probe. Fiber

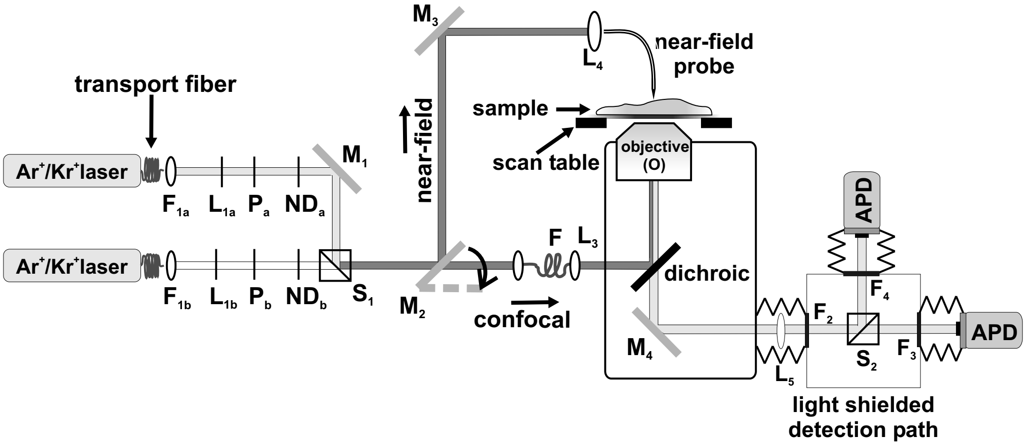

Figure 2.2: Scheme of the near-field/confocal scanning optical microscope. Single mode fibers are used to transport the light from two Ar^+/Kr^+ ion lasers (CW, Spectra-Physics) to the set-up. Objectives L_{1a}, L_{1b} (4×0.12 NA, Melles Griot (MG)) couple the light out of the transport fiber. The spectral- and intensity properties of both beams are controlled independently by laser line filters (F_{1a}, F_{1b}) and neutral density filters (ND_{1a}, ND_{1b}) in light paths a and b. P_{1a} and P_{1b} are broadband polarizing components to manipulate the polarization in both paths independently, i.e. precision linear polarizer (430 - 670 nm, Newport Corp., CA USA), $1/2\lambda$ and $1/4\lambda$ achromatic zero-order wave plates (460 - 655 nm, Newport). The two beams are overlaid by the combination of mirror M_1 and the broadband non-polarizing beam splitter cube S_1 (400 - 700 nm, Newport). Mirror M_2 is mounted on a flipper^{TM} mount (New Focus Corp., CA, USA) allowing fast and easy switching between confocal and near-field operation. In confocal mode, fiber F acts as spatial filter combining two wavelengths. Objective L_3 (4× 0.12NA) collimates the (dual colored) beam. Via a dichroic mirror and the main high NA oil immersion objective O (100× 1.3 NA, Zeiss or 64× 1.4 NA Olympus), the light is focused on the sample. The sample (cover glass ∼0.17 mm thick) is glued to a stainless steel holder, which is kept by small magnets and supported by a plate that fills most of the free volume between sample and objective. In NSOM mode, the light is directed via M_2 and M_3 and coupled with L_4 (16×0.32 NA, MG) into the near-field probe. On the detection side, filters (F_2 - F_4) are placed in a light tight box, also holding a dichroic mirror or a broadband polarization beam splitter cube (400 - 700 nm, Newport). Lens L_5 (f = 80 cm) focuses the fluorescence with a magnification of five times up to 150 μm (for 100× objective), similar to the active area of the APD detectors (SPCM-100, EG&G Electro Optics, now PerkinElmer Inc.).

probes fabricated in our lab have a throughput efficiency of 10^{-6} - 10^{-4} [72]. A typical aperture probe is shown in Figure 2.3(a). While the size of the aperture determines the optical resolution, the small aluminum grains (10 - 50 nm) protruding from the end face of the tip act as sharp little probes and provide high lateral topographical resolution. The definition of the probe end face structure, i.e. end face roughness and aperture size, can be improved by slicing the end face with focused-ion-beam (FIB) milling as shown in Figure 2.3(b) [72].

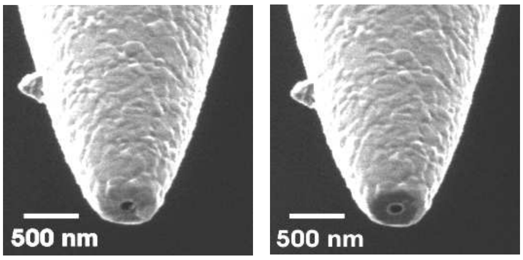

(a) (b)

Figure 2.3: The tapered aluminum-coated aperture probe in (a) is modified with side-on FIB milling, as shown in (b). The grains of the aluminum coating are clearly visible on both probes. The circular aperture in (a) has a diameter of ~ 80 nm, while the cut end face aperture in (b) has a diameter of ~ 100 nm.

Although the polarization characteristics are better defined with FIB-treated probes, in this thesis mainly regular (non-FIB treated) probes have been used in order to exploit the enhanced topographical resolution. The fabricated probes for the research presented here had end face apertures of 70 - 100 nm, throughput of $\sim 10^{-5}$ and extinction ratios in the two orthogonal polarization directions usually better than 1:15, as measured in the far-field.

To excite the sample in the near-field and obtain subdiffraction resolution, the probe-sample distance should be kept at < 10 nm. This requires a highly sensitive distance control, which in our NSOM is provided by a feedback mechanism based on shear-forces using a quartz piezo-electric tuning fork (100 kHz resonance frequency) as force sensing element [73, 144]. The scheme of shear-force distance control of the probe is depicted in Figure 2.4. The fiber is attached to one of the prongs of the tuning fork. The fiber end protrudes ~ 300 μm from the tuning fork. The resonance frequency of the tuning fork - probe system is typically 97 - 102 kHz with a quality factor of 100 - 500. The tuning fork is mechanically excited by an external dither piezo having a piezo-electric constant of 0.3 nm/V. During measurement, the dither piezo is driven at a frequency slightly below resonance with a driving amplitude in the order of 5 pm peak-to-peak, corresponding to about one nanometer lateral displacement of the tip as a result of the system resonance amplification. Upon approach of the probe to the sample surface, a phase shift of the tuning fork oscillation is observed [73]. The phase difference between the excitation signal from the function generator and the signal induced by the oscillation of the tuning fork is detected and used as a feedback signal for the tip - sample distance regulation. The bandwidth of the feedback electronics is ∼ 100 Hz. Electronic noise and mechanical vibrations of the sample limit the vertical noise in the topography images. For cell studies, the full vertical range (26 μm) of the scanner is exploited. The read-out accuracy with these settings is ∼ 6.4 nm, limited by the least-significant bit of the 12 bit digital to analog converter in the electronics. By reducing the driving voltage for the scanner the vertical noise in our set-up can become lower than 2 nm [145].

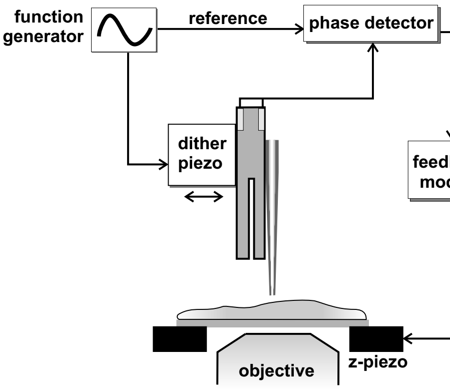

Figure 2.4: Diagram of shear-force distance control using a tuning fork. The function generator drives the dither piezo and provides the reference signal for the phase detector. A transimpedance amplifier amplifies the piezoelectric signal from the tuning fork. The feedback signal regulates the probe - sample distance via the movement of the scanner in the z-direction, generating at the same time a topographic image.

The probe and tuning fork are mounted in a tripod system that allows manual approach and x,y - alignment with respect to the objective. The total length of the fiber probe is kept short (∼ 10 cm) in order to minimize background luminescence from the fiber itself. The excitation power and polarization characteristics are measured in the far-field using an analyzer and photodiode at a separate exit port of the microscope.

Custom made electronic hardware and software control the feedback loop and raster scanning of the sample and record the photon counts of both APDs. During near-field measurements the z-piezo signal, the residual phase error on the feedback loop as well as the fluorescence signals from both APDs are recorded simultaneously.

2.2 General performance of the microscope

2.2.1 Detection efficiency

The detection efficiency of the microscope is given by the collection efficiency of the objective, transmittance of fluorescence filters and lenses, the reflectance of mirrors and the sensitivity of the APDs, as given by:

$$\eta_{det} = A \cdot \eta_{obj} \cdot \eta_{APD} \tag{2.1}$$

where A includes all filter, lens and mirror transmission and reflectance contributions, η_{obj} is the angular collection efficiency of the main objective and η_{APD} is the detection efficiency for the APDs. An important part of the losses is caused by η_{obj}, which is 0.42 for a 1.4 NA oil objective and 0.29 for a 1.3 NA oil objective, and the limited detection efficiency of the APDs, being 0.30 at $\sim$500 nm and $\sim$0.72 at $\sim$650 nm. In this thesis, mainly Alexa488 ($\lambda^{max}_{absorption} = 495$ nm, $\lambda^{max}_{emission} = 519$ nm) and Cy5 ($\lambda^{max}_{absorption} = 649$ nm, $\lambda^{max}_{emission} = 670$ nm) have been used as fluorescent labels. Emission of Alexa488 is selected using a long pass filter (ALP510, Omega Optical Inc.). An additional band pass filter (BP510-560, Omega Optical Inc.) is used in case of dual color experiments. The detection efficiency for Alexa488 is calculated to be $\sim$3% and $\sim$2% for 1.4 and 1.3 NA objectives, respectively with $A = 0.22$. Cy5 emission is selected by an ALP665 long pass filter (Omega Optical Inc.), resulting in detection efficiencies of 13% and 9% for the 1.4 NA and 1.3 NA objective, respectively with $A = 0.43$.

The expected photon flux S (photon counts/s) emitted by a single molecule is given by:

$$S = \eta_{det} \cdot \frac{\sigma \cdot \varphi}{h\nu} \cdot \eta_{abs} \cdot I_{exc} \tag{2.2}$$

where σ is the absorption cross section at the peak of the absorption spectrum of the fluorophore (cm^{-2}), φ is the fluorescence quantum yield, hν is the photon energy (J), η_{abs} is the absorption efficiency at the excitation wavelength and I$_{exc}$ is the excitation intensity (W/cm^2). For Alexa488 excited at an intensity of 1000 W/cm^2 at 488 nm, the expected fluorescence detection count rate is $\sim$5 kcnts/s (with $\eta_{det} = 0.3$, $\sigma = 3.0 \cdot 10^{-16}$ cm^{-2}, $\varphi = 0.48$, h$\nu = 4.1 \cdot 10^{-19}$ J and $\eta_{abs} = 0.75$). For Cy5 excited at an intensity of 1000 W/cm^2 at 647 nm, the expected fluorescence detection count rate is $\sim$75 kcnts/s (with $\eta_{det} = 0.3$, $\sigma = 9.6 \cdot 10^{-16}$ cm^{-2}, $\varphi = 0.27$, h$\nu = 3.1 \cdot 10^{-19}$ J and $\eta_{abs} = 1.00$).

2.2.2 Imaging with single molecule sensitivity

Figure 2.5(a) shows a confocal image of a dendritic cell (DC), containing Cy5-labeled membrane proteins. The image is built up in time by scanning the sample bottom left to top right corner, therefore containing both time and spatial information. The cell appears to be completely covered by proteins. Figure 2.5(b) shows two zoomed-in images, where the upper figure is made in NSOM mode and the lower one in confocal mode. In both images single molecule spots, exhibiting a discrete time dependent fluorescence behavior, have been identified. The confocal image is brighter in the region of the cell due to higher excitation intensity than used for NSOM as well as a larger contribution of intracellular autofluorescence.

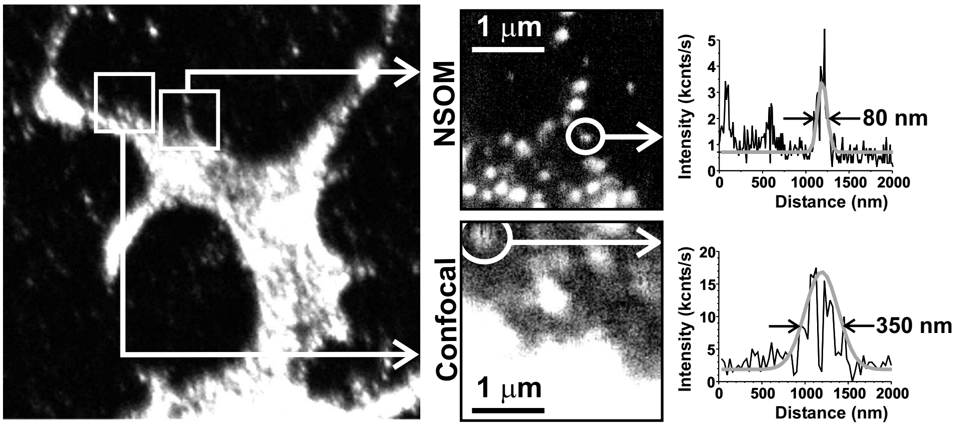

(a) (b) (c)

Figure 2.5: Confocal and near-field single molecule imaging of Cy5 labeled DC-SIGN proteins on a dendritic cell. (a) Confocal image of dendritic cell ($20 \times 20 \mu\mathrm{m}^2$ at 256×256 pixels). (b) Near-field (top) and confocal (bottom) zoom in of $3 \times 3\,\mu\mathrm{m}^2$ at 256×256 pixels and 100×100 pixels, respectively. Circularly polarized light ($\lambda = 647\,\mathrm{nm}$) has been used at $500\,\mathrm{W/cm}^2$ in confocal and $100\,\mathrm{W/cm}^2$ in near-field excitation. Fluorescence has been detected using a 1.4 NA objective. In both images a single molecule is indicated by a white circle. (c) Cross sections through the marked single molecule fluorescence spots in (b).

2.2.3 Optical resolution and localization accuracy

The intensity profile of a single molecule maps the lateral dimensions of the illumination spot. For example, Figure 2.5(c) shows two cross sections of the single molecule spots from the NSOM and confocal images in Figure 2.5(b). The intensity profile of a single molecule imaged with confocal microscopy or a single molecule with an in-plane emission dipole moment imaged with NSOM can be determined using a Gaussian response function [100, 146–153]. Although a Gaussion function is an approximation for the response of an NSOM probe, it is a practical function to use [154–156]. A one dimensional Gauss profile is given by:

$$S \exp\Big\{ -\frac{(x - x_c)^2}{2\Gamma^2} \Big\} \tag{2.3}$$

where x_c is the center coordinate of the Gaussian, S is the signal level above background and Γ is the variance of the Gaussian. The size (full width at half maximum) of the near-field intensity profile of Figure 2.5(c) as determined by a Gaussian fit is 80 ± 8 nm, resembling the probe aperture. The confocal spot size is 350 ± 15 nm, which is diffraction limited ($\sim 0.5\ \lambda$). The error in the position of the central peak is calculated by a χ^2-minimization procedure, in which the expression for χ^2 is minimum for $x = x_m$ [157]. The root squared error of the Gaussian response function is:

$$\frac{\bar{x} - \bar{x}_m}{\Gamma} = \sqrt{\frac{\Delta}{N_\Gamma S} \frac{1}{\int_{-t}^{t} u^2 \big(e^{-\frac{u^2}{2}} - \frac{B}{S}\big) du}} \tag{2.4}$$

where Δ is a constant related to the number of free fit parameters, i.e. $\Delta = 1$, 2.3 and 3.5 for 1, 2 and 3 fit parameters, respectively; N_Γ is the number of data points within Γ; $t = \frac{N}{2N_\Gamma}$ with N the total number of data points; B is the background level, which is assumed to be constant and u is the integration parameter. If the signal to background ratio is large, the first term in the integral of equation 2.4 becomes $\sqrt{2\pi}$ and the second term reduces to $\frac{2}{3}\frac{B}{S}t^3$. Equation 2.4 is then approximated by:

$$\frac{\bar{x} - \bar{x}_m}{\Gamma} \approx \sqrt{\frac{\Delta}{N_\Gamma S} \frac{1}{\sqrt{2\pi} - \frac{2}{3}\frac{B}{S}t^3}} \tag{2.5}$$

It is clear from equation 2.4 that the localization accuracy increases with the number of data points N_Γ and that the localization accuracy is depending on the shot noise $\sqrt{S}$. Using equation 2.5 the localization accuracy of the confocal spot in Figure 2.5(c) is calculated to be 27 nm, (with parameters: $\Gamma = 170$ nm, $N_\Gamma = 5$, $\Delta = 3.5$, $S = 14.1$ $B = 2.1$ and $t = 1.8$). For the near-field spot the localization accuracy is 14 nm, (with parameters: $\Gamma = 45$ nm, $N_\Gamma = 4$, $\Delta = 2.3$, $S = 3.4$, $B = 0.7$ and $t = 1.82$). Thus, even at five times lower excitation intensity used for NSOM, the localization accuracy is twice better than obtained confocally. The accuracy for NSOM can be improved if a zoom in is made, increasing N_Γ. For a larger signal to noise ratio and a larger number of data points, NSOM gives a localization accuracy < 1 nm [145].

2.2.4 Background reduction and surface specificity

As already mentioned in Chapter 1, one of the major difficulties when discriminating single molecules on the cell membrane is the large fluorescence background generated by intracellular components. This is particularly relevant for dendritic cells, investigated in this thesis, which are known for their high autofluorescence [158, 159]. The shallow penetration depth of the evanescent field emanating from the NSOM probe (< 100 nm) is an important advantage, minimizing the generation of autofluorescence from the cell. Figure 2.6 shows as example a cell imaged both in confocal (left) and NSOM (right) mode. The transmembrane protein of interest is labeled with Cy5. In the upper figures, the sample was excited at a wavelength of 647 nm, matching the peak in the Cy5 absorption spectrum. The advantage of NSOM as a high resolution imaging technique is clearly visible when comparing both images. Even more striking is the large fluorescence background suppression obtained by NSOM. In the lower figures, an excitation wavelength of 514.5 nm, outside the absorption spectrum of Cy5 has been used. While the confocal image exhibits a large background contribution from the cell, the NSOM image of the same region is virtually devoid of background, showing no contrast between glass and cell.

2.2.5 High resolution imaging

Finally, the advantage of a small excitation volume for fluorescence imaging of cells or other closely packed systems is demonstrated in Figure 2.7. This figure shows a typical experiment in which the sample is quickly examined with bright wide-field illumination using a CCD camera (a) and a confocal fluorescence scan (b), followed by a high resolution zoom in on an interesting area using NSOM (c,d). In both confocal and near-field mode the collected fluorescence was separated into two perpendicular polarization components, each with its own

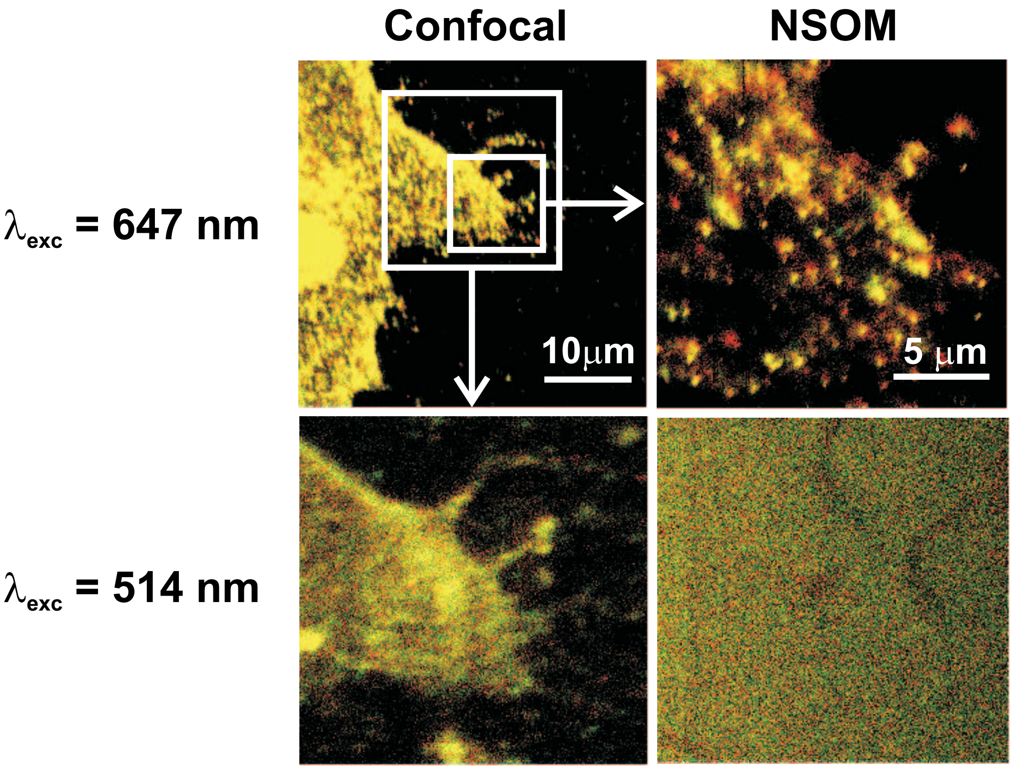

Figure 2.6: Fluorescence and autofluorescence from a Cy5-labeled cell, excited with 647 nm (upper images) and 514 nm (lower images), respectively. The confocal image (bottom left) shows a factor of ten more fluorescence on the cell (40 kcnts/s, $I_{exc} = 2.7\,\mathrm{kW/cm^2}$ at $\lambda = 514\,\mathrm{nm}$) than coming from the glass (4.5 kcnts/s). In the NSOM image (bottom right) fluorescence intensity from cell and glass are similar (3.6 kcnts/s, $I_{exc} = 2.7\,\mathrm{kW/cm^2}$).

detection channel. The pseudo-colors in the images reflect the relative contribution of each in-plane component and therefore the in-plane projection of the emission dipole moment of the excited fluorophore. The scale ranges from green (dipoles oriented along the vertical image direction) through yellow (dipoles oriented at 45^o or averaged value over a number of different dipole orientations) to red (dipoles oriented in the horizontal image direction).

The confocal image exhibits a large fluorescence intensity spread over the cell. The smallest spot size observed is diffraction limited. This, in combination with close packing of fluorescent molecules results in the large fluorescent patches shown in the confocal image. The optical near-field image in Figure 2.7(c) reveals details within the fluorescent patches and clearly distinguishes spots of different sizes. The smallest spot size is tip-convoluted, i.e. ~100 nm in diameter. The larger fluorescent spots consist of a number of closely packed dyes in a region larger than the aperture of the probe. The intensity of a spot is related to the number of dyes. Therefore, bright spots consist of closely packed dyes, indicating the existence of protein domains. A detailed description of this particular protein-cell system is given in Chapter 3. Figure 2.7(d) shows the topography image, which is simultaneously obtained with the near-field fluorescence image. The combination of topography and fluorescence intensity allows the determination of the absolute position of the fluorescence spots on the membrane. In particular, the topography image reveals that the apparent non-specific fluorescent spot in the fluorescence image (encircled) is actually localized on one of the cell dendrites. Therefore, topography is essential to find the origin of the fluorescence and can be used to check the sample for artifacts, such as non-specific binding of fluorophores and membrane folding. Fine dendrites on the topography image have a height of less than 50 nm, while the cell body has a height of 250 nm, indicating that the cell is well stretched on the substrate.

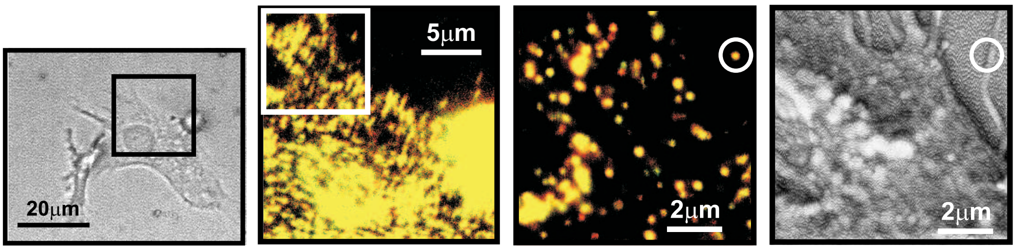

(a) Bright field (b) Confocal (c) NSOM (d) Topography

Figure 2.7: Imaging membrane proteins externally labeled with Cy5 on a dendritic cell. (a) Bright field image of a DC stretched on glass. The box shows the scan area used for confocal imaging. (b) Confocal image, showing an area of $20 \times 20 \mu m^2$, 256×256 pixels. Fluorescence was collected using a 1.4 NA objective. (c) Near-field fluorescence image of the white frame in (b), i.e. an area of $7 \times 7 \mu m^2$ (256×256 pixels) is scanned. Circularly polarized light ($\lambda = 647$ nm) has been used for both confocal and near-field excitation. (d) Shear-force topographic image, simultaneously recorded with (c).

2.3 Conclusion

A versatile fluorescence microscope combining both near-field and confocal scanning optical microscopy with single molecule sensitivity has been described in this chapter. The microscope allows fast and easy switching between near-field and confocal microscopy, with no additional adjustment on the detection side. NSOM provides topography correlated with fluorescence images. A tuning fork (resonance at 100 kHz) is used as a shear-force sensing element to regulate the probe - sample distance. The vertical resolution is limited by electronic noise and mechanical vibrations, resulting in a vertical noise of several nanometers. The detection efficiency of the microscope is mainly determined by the collection efficiency of the objective and the detection efficiency of the avalanche photodiodes and is $\sim 9\%$ for Cy5 detection ($\lambda_{detection} \sim 670\,\mathrm{nm}$) and $\sim 2\%$ for Alexa488 using a 1.3 NA objective ($\lambda_{detection} \sim 520\,\mathrm{nm}$). The microscope has single molecule sensitivity in near-field as well as confocal mode. Single molecules in fluorescence images map the lateral size of the illumination spot, which is diffraction limited in case of confocal illumination and limited by the aperture size in case of near-field microscopy. The center of a Gauss fit, applied on a confocal or near-field fluorescence spot, has a localization accuracy of 27 nm for confocal, and 14 nm for the single molecule near-field spot in Figure 2.5(c), in which the near-field excitation intensity used was five times lower than the confocal excitation. The small excitation volume provided by NSOM is essential when measuring densely packed molecules. This is illustrated in figure 2.6, where confocal excitation gives rise to more autofluorescence than near-field excitation. In addition, NSOM provides topography information, which is important when imaging cells as it provides information about the exact location of the fluorescence.

Chapter 3

Nano-scale organization of DC-SIGN on the membrane of dendritic cells

The nano-scale organization of DC-SIGN, a transmembrane protein expressed on the membrane of immature dendritic cells (imDCs) has been investigated using the confocal/near-field scanning optical microscope (NSOM) developed. Nano-scale domains, typically 185 nm in diameter, have been directly observed. A wide spread in molecular packing density, i.e. number of molecules per area, has been found, ranging from a few molecules to tens of DC-SIGN molecules per domain. These domains appear randomly distributed on the membrane. By correlating the number of DC-SIGN molecules in each domain to the size of the domain, we have calculated intra-domain distances in the order of tens of nanometers. The hierarchical organization found, in which DC-SIGN molecules are assembled in randomly spread domains, might bare direct relation to the pathogen-binding function of immature DCs.

3.1 Introduction

Fluorescence microscopy remains the preferred experimental approach for investigating the spatial organization of receptor molecules on the surface of cells [160, 161], and is enhanced by the possibility of exploiting autofluorescent proteins in (dynamic) studies on living cells. To date, standard fluorescence measurements performed on isolated cells have shown first indications for a well defined spatial organization of membrane specific receptor proteins but without any details (see for example [161, 162]). This is mainly due to the lack of single molecule detection sensitivity and poor spatial resolution, making discrimination of individual entities within densely packed complexes impossible. Our set-up however brings these capabilities. This chapter describes the first study performed with the developed near-field & confocal microscope on a biological sample of intact immature dendritic cells (imDCs). The nano-scale organization of a transmembrane adhesion protein (DC-SIGN) present on the imDC membrane has been visualized and quantified.

3.2 Dendritic cells and the role of DC-SIGN

Dendritic cells (DCs) are the sentinels of our health, playing a crucial role in both innate immunity and the initiation of adaptive immunity, as described briefly in Chapter 1. The lifetime of a DC comprises different stages, each characterized by a different cell function, as schematically shown in Figure 3.1. DC - precursors develop into immature dendritic cells (imDCs), which then patrol the body for intruders and efficiently bind to pathogens. After pathogen binding, the imDCs migrate to the draining lymph nodes. During transit, they rearrange their surface profile, i.e. type and number of surface molecules and lose their ability to take up antigens. They also increase the number of antigenic peptides and other molecules in order to bind to T cells. This process is called maturation. In the lymph nodes the fully matured DCs activate T cells to eliminate the infection [10, 136, 163–165]. A crucial aspect during the whole process is cell adhesion, necessary for the DC to migrate, capture pathogens, and to signal T cells. In this research we have focused on the molecular surface profile of imDCs which plays a key role in pathogen binding.

The recently identified surface receptor DC-SIGN (DC-Specific ICAM (inter cellular adhesion molecule) Grabbing Nonintegrin), also referred to as CD209, is exclusively expressed by DCs and takes part in several types of DC interactions [136, 166]. DC-SIGN is a type II transmembrane protein, containing a mannose-binding C-type lectin domain that forms the ligand-binding site [1]

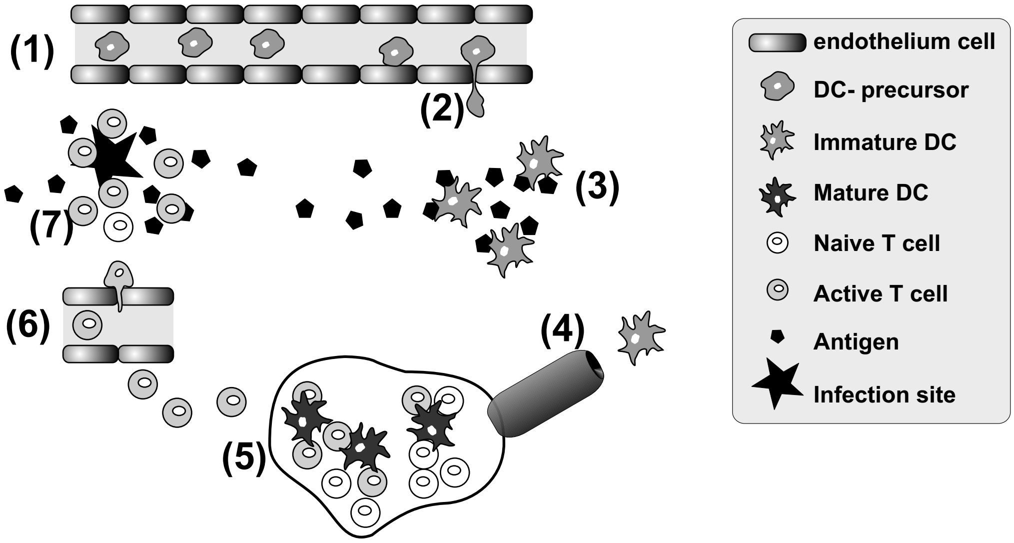

Figure 3.1: Various DC functions during the immune response. (1) DC - precurors (monocytes), present in the blood stream. (2) DC-precursors are attracted to infected tissue by inflammation, as described in section 1.4. During migration from the blood stream into peripheral tissue, the DC-precursors develop to immature DCs (imDCs). (3) ImDCs binding to antigens. (4) ImDCs transform into mature DCs during their travel to the lymph system. (5) In the lymph node, mature DCs present pathogenic material to naïve T cells and activate them. (6) Activated T cells migrate to the infection site. (7) Activated T cells eliminate the infection.

[161, 162]. DC-SIGN can bind to different ligands and performs a dual role for the DC: it can act as an adhesion receptor as well as a pathogen recognition receptor [166]. As a cell adhesion receptor, DC-SIGN mediates the interaction between DCs and endothelial cells, the building blocks of our blood vessel walls, via the ligand ICAM-2 [167]. This interaction stops the DC from free floating in the blood and allows a directed migration movement into the peripheral tissue. DC-SIGN also binds to ICAM-3, a molecule present on T cells, ensuring adhesion between mature DCs and T cells which is necessary for T cell activation [162]. In the last three years, extensive research has been performed on the pathogen recognition capabilities of DC-SIGN. DC-SIGN contains a carbohydrate recognition domain (CRD) that has a high affinity for high-mannose N-linked oligosaccharides such as those present on the envelope proteins gp120, E, E2, E and GP of the human immunodeficiency virus (HIV-1) [162], Dengue

---

[1] A ligand is any molecule that binds to a specific site on a molecule.

virus [168], cytomegalo virus (CMV) [169], Ebola virus [170] and Hepatitis C virus (HCV) [171, 172], respectively. DC-SIGN has also shown to bind micro-organisms such as Leishmania [173], Candida albicans [174], Mycobacterium [175–177] and Schistosoma [178]. It is clear that unraveling the role of DC-SIGN in the immune response is important to understand the early stage of human infections.

Although the expression level of DC-SIGN influences the functionality of the DC, it is not clear how the cell spatially arranges DC-SIGN to perform its specific function. For instance, recent investigations have shown that some pathogens, including HIV-1, exploit cholesterol rich domains to enter host cells [179]. This finding in combination with the high affinity of imDCs for the HIV-1 virus may point to a role for the spatial organization of DC-SIGN to regulate the binding capability of the imDC for pathogens. We have used NSOM to reveal the spatial organization of DC-SIGN on the membrane of imDCs.

3.3 Materials and Methods

Cell preparation and labeling

Immature DCs were cultured from healthy human blood monocytes in presence of IL-4 and GM-CSF, 500 and 800 units/ml, respectively (Schering-Plough, Brussels, Belgium). After 6 days of culture, flow cytometry analysis showed low levels of CD14 and CD83, moderate levels of CD86, and high levels of MHC class I and II, consistent with the phenotype of imDCs [162]. The DCs obtained were stretched on a fibronectin-coated glass coverslip for 1 hour at 37 °C and fixed with 1% paraformaldehyde in PBS for 20 minutes. The specimens were rinsed in two washing steps with PBS and PBA (PBS containing 0.5 % BSA and 0.01 % sodium azide), respectively. The cells were then incubated with primary monoclonal antibodies (mAb) AZN-D1 in PBA (10 μg/ml, 25 min). The AZN-D1 antibodies are home-made, as described by Geijtenbeek et al. [162]. After two washing steps with PBA, a second incubation was performed with goat anti - mouse Cy5 (Fab fragment) (Immunotech - Beckman Coulter, Marseille, France), 1 : 125 in PBA for 25 min, allowing fluorescent detection of the anti-DC-SIGN antibody. The labeling efficiency as given by the manufacturer was 2 - 4 Cy5 molecules per antibody. Samples were subsequently post-fixed in 2% paraformaldehyde, dehydrated by subsequent incubations in 30%, 50%, 70% and 100% pure ethanol and finally critical-point dried.

Single molecule measurements on DCs

Cy5-labeled DC-SIGN molecules were excited at a wavelength of 647 nm either confocally or in near-field mode. In confocal mode, incoming circularly polarized light was reflected by a dichroic mirror (650 DRLP, Omega Optical Inc., Brattleboro, VT, USA) and focused onto the sample with a 1.4 NA objective. In NSOM mode, the Al-coated near-field probe was kept at ~ 10 nm distance from the cell surface by a feedback mechanism using tuning fork shear-force sensing, as described in Chapter 2. On the detection side, the emitted fluorescence ($\lambda > 665$ nm) was selected using a long-pass filter (665 AELP), separated into two orthogonal polarization components using a polarizing beam splitter, and then detected by two avalanche photodiodes (APDs).

Cells were selected using wide bright-field illumination and then imaged in confocal mode (typical scan size $\sim 30 \times 30\,\mu\text{m}^2$, 256×256 pixels). A region containing cell dendrites and showing fluorescence contrast was then selected for further near-field investigation. The size of a near-field scan area was typically $7 \times 7\,\mu\text{m}^2$ (256×256 pixels). The scanning speed used was 3 - 6 μm/s, depending on the surface roughness. The cell height in the dendrite region varied from tens of nanometers to a few micrometers. All data shown in this chapter have been acquired using the same near-field probe. Images were obtained at a typical excitation intensity of 150 W/cm^2. The topographic images, simultaneously obtained with the fluorescence data, were used to determine the exact position of each fluorescent spot on the cell membrane and to exclude artifacts due to the structure of the membrane, such as steep cell edges and membrane folding or ruffling.

Image analysis

A total of 1251 fluorescent spots in 20 images from 7 different cells were characterized in terms of their size, intensity, position on the cell membrane and relative position with respect to each other. The size of every individual spot was determined by fitting the measured intensity profile with a 2D Gaussian profile. The spot size was defined as the full-width at half-maximum (FWHM) of the fit. The intensity of each spot was determined by adding all photon counts within a contour of $\sim 15\,\%$ of the peak intensity level and subtracting the cell background in the immediate vicinity of the spot. The spot intensities were related to the intensities detected from single Cy5 molecules. The positions of all spots on the cell membrane were determined by combining the near-field optical and topography images. Mutual spot distances were examined by means of nearest neighbor distance analysis [180]. For this purpose the position of each spot was determined from the peak position of a Gauss fit to the intensity profile.

3.4 Results

3.4.1 High resolution imaging of DC-SIGN

Typical fluorescence measurements of an imDC expressing DC-SIGN at the cell surface are shown in Figure 3.2. The typical structure of an imDC with fine dendrites is clearly observed in the confocal image of Figure 3.2(a). The high fluorescence intensity is caused by the high expression level of DC-SIGN on the membrane. The smallest visible features have a diffraction-limited size of $\sim 350\,$nm. From the image, it is hard to distinguish isolated entities on the cell surface. In contrast, the high resolution near-field image in Figure 3.2(b) of the selected area in Figure 3.2(a) shows the distribution of DC-SIGN in more detail. Figure 3.2(b) is composed of three independent near-field measurements in which the fluorescence spots overlay the topography. The smallest measured size of the near-field fluorescent spots is $\sim 100\,$nm, comparable to the probe aperture size. Areas of closely packed molecules are resolved spatially with a localization accuracy better than 10 nm.

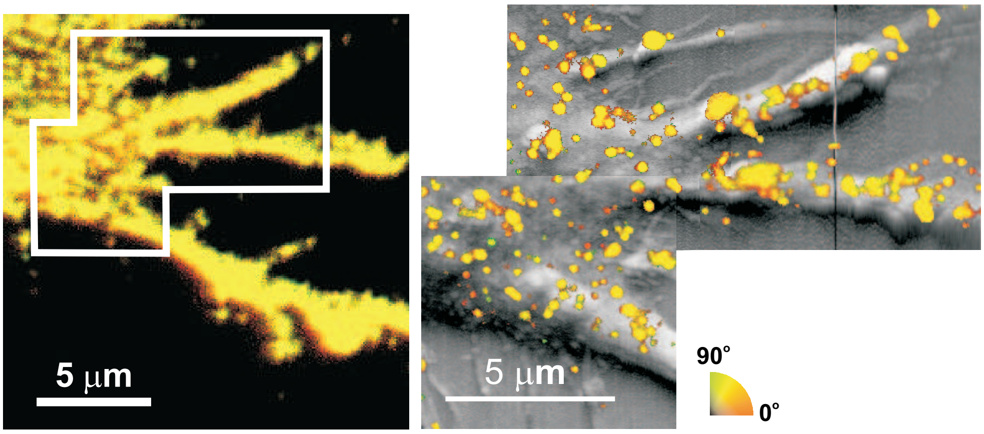

(a) (b)

Figure 3.2: Imaging Cy5 labeled DC-SIGN molecules on the membrane of an imDC. (a) Confocal image ($20 \times 20\,\mu m^2$, $50\mu m/s$) of an imDC stretched on glass. Large and intense fluorescent patches cover the entire cell surface. (b) Combined topography and near-field fluorescence image of the area in the white frame in (a), composed of three partially overlapping near-field images (area: $7 \times 7\,\mu m^2$, scan speed: $3\mu m/s$). In both (a) and (b) the fluorescence signal is color-coded according to the detected polarization, red$=0\,°$, green$\,=90°$. The height of the dendritic regions varies from 10 nm to $3\,\mu m$.

In addition, the shallow penetration depth of the evanescent field guarantees exclusive excitation of the cell surface, thereby suppressing the autofluorescence of the cell as discussed in Chapter 2. The fluorescent spots in the near-field images differ in brightness, size and emission polarization, already suggesting that DC-SIGN is not randomly distributed as individual molecules but rather clustered in domains, assuming a uniform labeling of all DC-SIGN on the cell membrane.

3.4.2 DC-SIGN clusters in domains

Intensity analysis

Figure 3.3 shows a typical near-field fluorescence image in 3D, indicating the most important characteristics of the fluorescent spots, i.e., intensity, size and relative position with respect to each other. The total number of detected photon counts from a spot is related to the number of Cy5 dyes and thus to the number of DC-SIGN molecules.

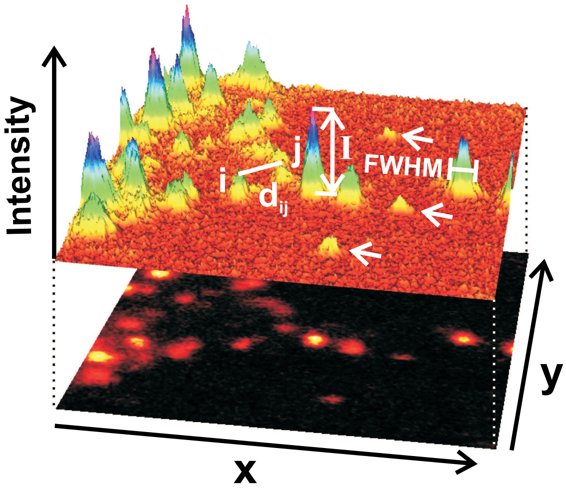

Figure 3.3: Information extracted from a typical near-field fluorescence image ($3 \times 3\,\mu\text{m}^2$, 256×256 pixels). The fluorescence in the upper image is plotted in three dimensions with x and y as spatial axes and a vertical intensity axis. The fluorescent spots differ in intensity (I) and size (FWHM). The arrows point to single molecule spots. The spatial position of the spot is given by the center coordinates of the intensity profile after fitting with a Gaussian function. The total number of detected photon counts of each spot, is related to the number of Cy5 dyes present. The nearest neighbor distance between two spots i and j is indicated by d_{ij}.

All spot intensities were collected in a histogram as shown in Figure 3.4(a). The spot intensities range from 1 kcnts/s to more than 1 Mcnts/s, with an average value of 200 kcnts/s, which is a range of about three orders of magnitude. The inset of Figure 3.4(a) shows a zoom in on the low intensity part of the total histogram. The distribution peaks at ∼ 25 kcnts/s. In order to relate these intensity values to the number of Cy5 molecules, the intensity histogram has been normalized to the typical intensity obtained from an individual Cy5 molecule. From each measurement, spots exhibiting single molecule signatures such as bleaching, blinking and a unique emission dipole were selected. In Figure 3.4(b) four single molecule spots are marked. The distribution of single molecule intensities is superimposed on the histogram in the inset of Figure 3.4(a).

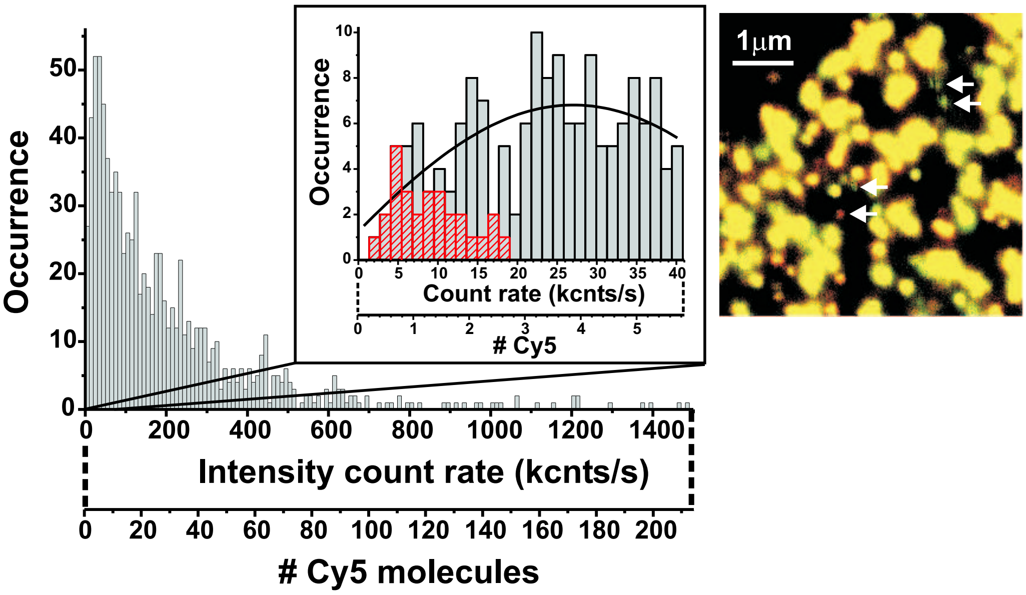

(a) (b)

Figure 3.4: (a) Intensity distribution of all measured spots at an excitation intensity of ∼ 150 W/cm^2. The inset shows a zoom in on the lowest intensity values (< 40 kcnt/s), including the intensity of single molecule spots which are contained in the red shaded histogram. The peak of the single molecule histogram is used to convert the intensity count rate to the number of Cy5 molecules, as shown in the lower axes of (a). (b) Near-field image of imDC membrane, measured with polarization contrast. The arrows point to fluorescence spots on the cell membrane, exhibiting single molecular fluorescence behavior.

The average count rate of the single molecule distribution is ~ 7 kcnts/s. This value is used to assign the number of Cy5 molecules to the intensity of a spot. The overall intensity distribution peaks at ~ 3.5 Cy5 molecules with an average value corresponding to ~ 30 Cy5 molecules. The range of spot intensities exceeds a value of 200 Cy5 molecules in one single spot. Considering that the antibody labeling efficiency is 2 - 4 Cy5 molecules per secondary antibody, our results indicate that the peak of the intensity distribution corresponds to approximately one DC-SIGN protein. However, the majority of DC-SIGN molecules ($\sim 80\%$) are clustered on the membrane, with each cluster hosting from a few to tens of DC-SIGN molecules.

Domain size analysis

Further evidence for DC-SIGN clustering was obtained from the sizes of the fluorescent spots. A histogram of all spot sizes, i.e. FWHM values, is shown in Figure 3.5(a). The spot sizes vary from 70 nm to 650 nm with a peak at 200 nm and a mean value of 210 nm, respectively. The inset of Figure 3.5(a) shows a distribution which contains the sizes of single molecule spots. All measurements have been performed using the same probe. At the start of the measurement series, the single molecule response of the probe was ~ 70 nm in size. During 20 near-field scans on 8 different cells, the single molecule response gradually increased to ~ 120 nm, which is probably due to probe wear and opening up of the probe aperture.

The peak of the single molecule size distribution is ~ 100 nm and is clearly separated from the peak of the main size distribution. The measured sizes of the fluorescent spots result from a convolution between the probe aperture and the sample, as described in Chapter 2. The real size of a domain can be deduced by correcting the measured spot profile for the size of the probe aperture. Figure 3.5(b) shows the measured size of an object as a function of its real size, where for simplicity a Gaussian probe response centered at 100 nm has been considered. Correction of the measured sizes, using the relation in Figure 3.5(b), results in spot sizes up to 500 nm with a mean value of ~ 185 nm. The size correction pulls the small measured object sizes (< 200 nm) to lower values, while large sizes remain approximately the same. The deviation in estimated size, i.e. the difference between the solid and dashed line in Figure 3.5(b), decreases with increasing feature size. Both intensity and size analysis indicate that Cy5 molecules, and thus DC-SIGN, are confined into small domains. To our knowledge, this is the first time that such small domain sizes have been directly observed by optical means.

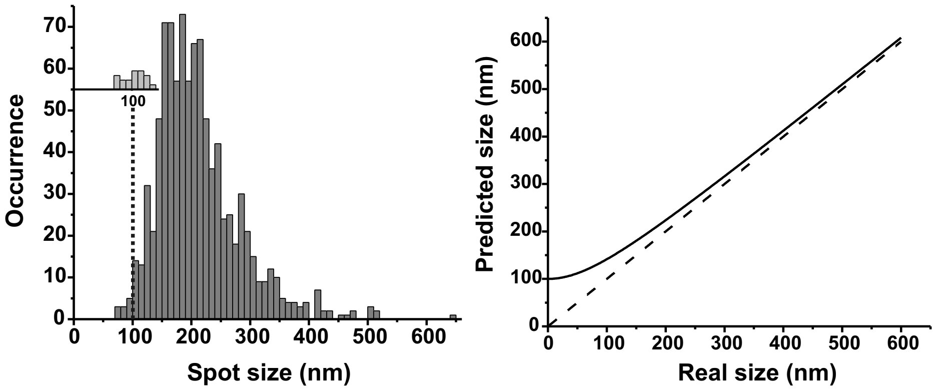

(a) (b)

Figure 3.5: (a) Size distribution of all measured spots. The inset shows sizes of 19 single molecules. (b) Predicted size as a function of the real size of a feature. Because the near-field fluorescence spots result from a convolution of the size of the probe aperture (diameter of 100 nm) and the sample, the smallest fluorescence features appear in an image as 100 nm spots (solid line). The dashed line indicates the case of the ideal resolution, in which the measured and real size are identical.

Molecular density in DC-SIGN domains

Information about the molecular density within a domain is obtained by correlating the intensity and size of each fluorescent spot. Such a correlation plot is shown in Figure 3.6. The plot demonstrates a large variety in packing density of the observed domains. The average intensity of ~ 200 kcnt/s (≈ 30 Cy5 molecules) together with the average corrected spot size of ~ 185 nm correspond to a Cy5 density of $\rho \sim 1000$ Cy5 molecules/μm^2, which is indicated by the gray line in Figure 3.6.

We make an estimation of the number of DC-SIGN molecules per spot, by taking into account the Cy5 labeling efficiency of ~ 3.5. Assuming 100% protein-antibody labeling efficiency and a random ordering of DC-SIGN molecules within a domain, the average nearest neighbor distance (*nnd*) between DC-SIGN molecules is related to the molecular density by $nnd = \frac{1}{2 \cdot \sqrt{\rho}}$, where ρ is the molecular density [180]. With this relation, the average *nnd* in each domain is calculated and plotted in a *nnd* histogram, as shown in Figure 3.7. The *nnd* distribution peaks at ~ 21 nm and has a mean value of ~ 39 nm.

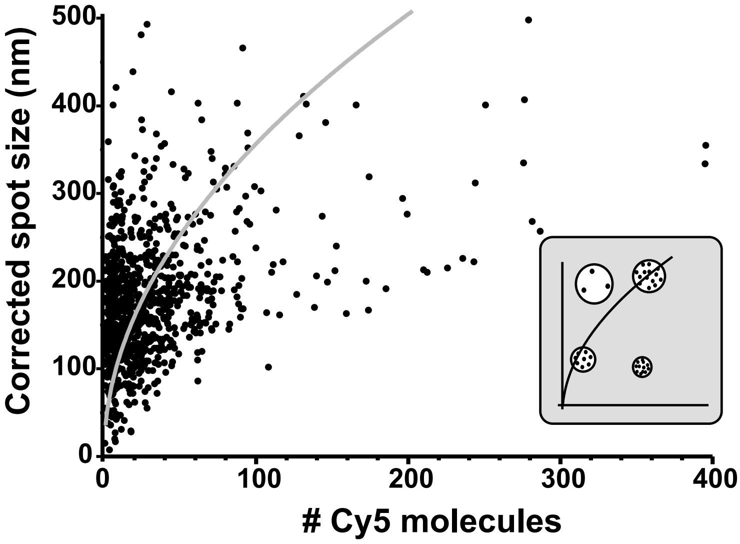

Figure 3.6: Correlation between the corrected size of a spot and its Cy5 content. Every point in the graph corresponds to one measured spot. The gray line shows the average occurring molecular packing density, i.e. $\rho = 1000\,\mathrm{Cy5}/\mu\mathrm{m}^2$ as calculated by $S(\rho) = \sqrt{4N_{Cy5}/(\pi\rho)}$, where $S(\rho)$ is the spot size and N_{Cy5} the number of Cy5 molecules. The cartoon in the inset illustrates four types of domain packing: top left is a large domain containing only few Cy5 molecules, i.e., low molecular density; bottom right is a small domain containing a large number of Cy5 molecules, i.e., high molecular density. The remaining two domains have similar packing density but are different in size.

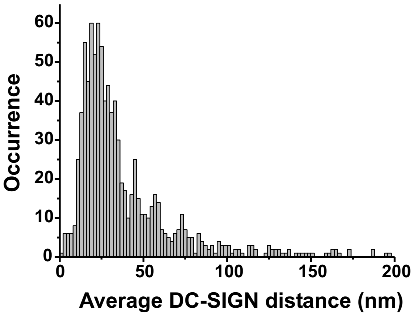

Figure 3.7: Distribution of DC-SIGN nearest neighbor distances within each domain, assuming a random DC-SIGN packing.

3.4.3 Spatial distribution of DC-SIGN domains.

We have also used *nnd* analysis to investigate the distribution pattern of the domains on the membrane. The area covered by domains represents 8% of the total cell area, with an average density of 2.53 domains/μm^2. The mutual distances between all detected spots are included in a distance distribution shown in Figure 3.8(a). This figure provides information both on inter-domain distances as well as the type of domain distribution. The mean value of the distribution is $\sim$450 nm. The measurements were compared to a calculated *nnd* distribution of randomly distributed spots (Poisson distribution), using the measured average domain density of 2.53 domains/μm^2. The Poisson distribution has a mean value of 344 nm. The overall shapes of both measured and calculated distributions resemble each other, especially on the right side of both plots. The difference in shape for small *nnd* values is caused by the finite size of the domains. Because the majority of the domains have a size of $\sim$200 nm (see Figure 3.5), the majority of the *nnd* values will be larger than this value. From the shape similarity between both distributions it appears that the domains are randomly distributed on the membrane.

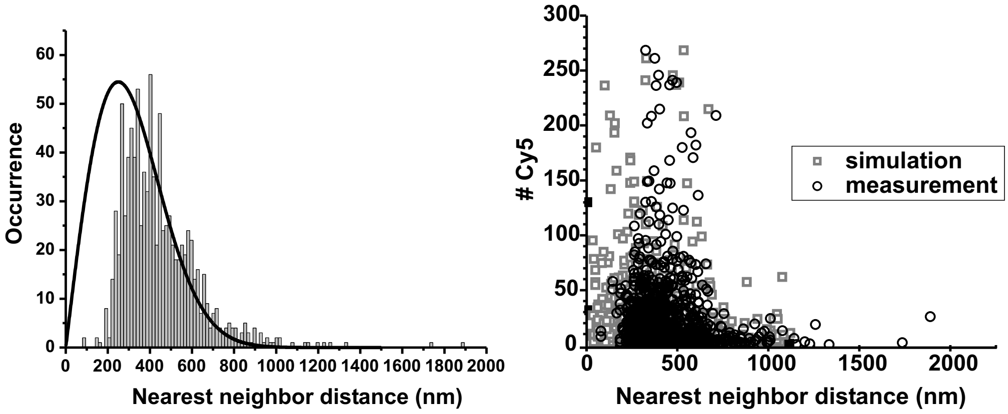

(a) (b)

Figure 3.8: (a) Inter-domain distance histogram obtained by *nnd* analysis of all measured fluorescence spots. A Poisson (random) distribution for the domain density of 2.53 domains/μm^2 is indicated by the black solid line in (a). (b) Correlation between domain intensity and inter-domain separation of both measured- and simulated data. In the simulation, the intensities of all domains are distributed randomly on the surface. Because only intensity and not the size of the domains is included in the simulation, the simulated inter-domain distances can take much lower values than experimentally observed (left side of the plot).

Although this first analysis indicates that the domains are organized on the membrane in a random fashion, we investigated the possibility of a non-random spatial distribution of the domains by correlating the number of Cy5 molecules within a domain with the mutual domain separation, shown in Figure 3.8(b). An apparent correlation emerges from the shape of the correlation plot, i.e., large intensity values correlate with shorter inter-domain distances, and vice versa. However, the large wings both in intensity and inter-domain distance are the result of the large number of occurrences at a distance of ~ 350 nm and an intensity of 3.5 Cy5 molecules, respectively. This was confirmed by the outcome of simulations in which each NSOM measurement was mimicked in terms of cell contours, total number of present domains and domain intensities. In each simulation, random (x,y) coordinates have been assigned to the domains within the defined cell contour. The distances between the randomly positioned domains have been analyzed and calculated in a similar fashion as described for the measurements. The correlation plot of domain intensity versus the inter-domain distances from the simulations is included in Figure 3.8(b). The overall shape of the correlation is similar for both measurement and simulation, confirming that DC-SIGN domains are randomly distributed on the membrane.

3.5 Discussion

In this chapter we have focussed on the nano-scale organization of DC-SIGN on the membrane of immature DCs. Recent *in vitro* studies have suggested that oligomerization of DC-SIGN enhances its ability to bind to multivalent ligands, such as those present on the viral envelope of HIV-1 and HCV, while performing its pathogen-recognition role [171, 181]. It has also been shown that pathogens and toxins make use of cholesterol rich domains as cell entry and exit sites [36, 137, 179, 182, 183]. Moreover, some first biochemical experiments indicated a moderate association of DC-SIGN with lipid raft components [1] [184] . The accurate localization and detailed structural and spatial organization of DC-SIGN appear therefore essential to elucidate the structure-function relationship between DC-SIGN and imDC.

The measurements and analysis presented, show the advantage of NSOM as a high resolution optical technique relative to confocal microscopy when applied to densely packed systems. The small illumination spot of NSOM allowed discrimination of isolated fluorescent spots of Cy5-labeled DC-SIGN on the surface of an imDC. Analysis of the fluorescence intensity of each spot (Figure 3.4(a))

---

[1] Lipid rafts are specialized membrane domains composed mainly of cholesterol and sphingolipids.

confirmed clustering of DC-SIGN. These observations are fully consistent with the findings of Cambi et al. [184], in which DC-SIGN was labeled with gold beads and imaged using transmission electron microscopy. In general, clustering of proteins can have different functions for the cell such as local enhancement of molecular binding properties or signaling ability [185, 186] and/or increase of local concentration of proteins to localize a specific protein function. A similar type of organization is found in epithelial cells exhibiting an asymmetrical (polarized) functionality due to formation of molecular domains [36, 137] or the immunological synapse, where molecular complexes facilitate binding and signaling between T cells and antigen presenting cells [160, 187–190]. Since it has been shown that DC-SIGN on imDCs binds with high affinity to a wide range of pathogens ([184] and references therein) and pathogens use lipid rafts as entry and exit portals for host cells [179, 191, 192], it seems reasonable to associate the existence of DC-SIGN clustering with the presence of lipid rafts. On-going experiments, e.g. NSOM under liquid conditions, should shed light on the validity of this hypothesis.

As already mentioned, *in vitro* biochemical studies have shown that DC-SIGN forms multimers, e.g. dimers and tetramers [171, 181]. These oligomers contain fewer molecules than the average number of DC-SIGN molecules per spot we have observed, i.e. ~ 10 molecules. Although oligomerization of DC-SIGN might occur, it seems improbable that the clusters we have observed are exclusively due to oligomerization. In fact, the physical size of the clusters of about 185 nm as shown in Figure 3.5(a) together with the wide spread of intensity in Figure 3.4(a) are more consistent with a recruitment of proteins to increase the local concentration of DC-SIGN. Of course, subsequent oligomerization as a result of the increase in the local concentration of DC-SIGN bring about that clusters cannot be excluded at this stage.

An increase in the local concentration of DC-SIGN might facilitate cell-pathogen binding. In fact, experiments by Cambi et al. have shown that imDCs are able to bind virus-like particles of 40 nm in diameter, while intermediate DCs with a random distribution of DC-SIGN on their surface do not bind these particles [184]. It is probable that the cell combines the enhanced adhesion ability of DC-SIGN domains with the pathogen's preference for cholesterol rich regions. In order to understand the possible reasons for DC-SIGN clustering we have modeled and simulated the capacity of targets of different sizes to establish interactions with either individual or clustered DC-SIGN molecules. Our simulations address the following questions: Is there a difference in binding capacity upon clustering as compared to individuals?; Is there an effect of the target size?; and, provided that clustering is beneficial, what are the optimum clustering conditions, i.e. molecular density and size; and how does it depend on the target size?

Details of this simulation model are described in Chapter 4.

Correlating the intensity and the size of each detected fluorescent spot, enabled determination of the molecular packing density of the domains. We have observed a large variation in the molecular packing density of each domain (see Figure 3.6). While the size distribution of the domains was centered around 185 nm with a width of 50 nm, the number of molecules within each domain varied significantly from cluster to cluster. It is remarkable that the DC-SIGN domains found in our experiments have a size similar to most viruses (30 - 500 nm diameter). This correspondence is consistent with the hypothesis that the imDC arranges DC-SIGN molecules in a way that optimizes virus-cell binding. Using a similar line of reasoning, one could argue that the large spread in molecular density, primarily due to the number of molecules involved in each cluster, might serve to maximize the chances of the imDC to bind a large variety of viruses, having similar physical sizes but different binding affinities. Of course our experiments are static, while it is reasonable to think that the formation and the existence of clusters is a rather dynamic process, i.e., clusters might change size and density. Nevertheless our images are snapshots that map at a given moment the entire process of formation, existence and degradation of domains, rendering information on all possible situations.

In addition to the molecular density in each cluster, we have estimated the distance between DC-SIGN molecules in each cluster, typically 21 nm. The distance distribution in Figure 3.7 is based on three main assumptions. First, for simplicity it is assumed that DC-SIGN is randomly distributed within a domain. Second, the antibody to Cy5 ratio is 1 : 3.5. This labeling efficiency has a small effect on the estimated distances, as labeling ratios of 1 : 2 and 1 : 4 shift the peak of the histogram from 17 nm to 23 nm respectively. Third, the Cy5*antibody to DC-SIGN ratio is one-to-one. In reality the antibodies will spatially hinder each other if the proteins are too densely packed, causing the antibody to protein ratio to be less than one and resulting in a underestimation of the number of proteins in this study. Recent NSOM experiments on the same cell system have shown that the fluorescence emission of Cy5 labeled imDCs is more intense when the cells reside in liquid compared to measurements under dried conditions. This indicates that the cell drying procedure quenches or damages the Cy5 fluorophores. Of course it is preferable to fuse DC-SIGN with an autofluorescent protein to visualize DC-SIGN in the natural environment, ideally within the living cell. This has several advantages: a one-to-one fluorophore to protein ratio and a less severe treatment of the cells as no drying procedure is required. However, attempts to let DCs express autofluorescent DC-SIGN proteins have not been successful so far.

Finally, we have observed a random distribution of the protein domains with a mean inter-domain distance of $\sim 450\,\mathrm{nm}$, as shown in Figure 3.8(a). The reason for a random domain distribution is probably to maximize the chances that a pathogen will meet a domain in a random encounter with the cell. Furthermore, we investigated the possibility of a dynamic domain organization by means of a correlation plot showing the domain intensity as function of the nearest (domain) neighbor distance Figure 3.8(b). If the formation of domains is a diffusion assisted process, similar to what is observed in thin film nucleation, we should have observed in our static images some evidence for DC-SIGN nucleation and coalescence, i.e., presence of 'small', low intensity domains being closer to 'large', high intensity domains. We were however not able to find a clear correlation between inter-domain distance and intensity. As the ordering of DC-SIGN domains seems random, with no clear evidence for DC-SIGN diffusion, our data suggest that the domains emerge to the cell membrane in a rather pre-assembled way. Dynamic experiments should reveal whether pre-assembly or diffusion of DC-SIGN takes place on imDCs.

3.6 Conclusions

Near-field illumination has proven to be valuable for discriminating individual entities in densely packed systems, in particular single molecule detection on the cell membrane. We have observed a two-layer hierarchical organization of DC-SIGN. In the first layer, DC-SIGN resides on the membrane of an imDC in domains with a typical size of 185 nm and a wide spread of molecular content. In the second layer, the domains are spread in a random fashion at a typical density of $2.53\,\mathrm{domains}/\mu\mathrm{m}^2$, thereby covering about 8 % of the total membrane area. The domain properties, i.e. size and content, seem to facilitate virus binding, whereas the random domain distribution is likely to maximize chances of a domain - pathogen encounter. Questions remain as to how DC-SIGN gathers into these regions and how the cell regulates the organization of DC-SIGN. Near-field scanning optical microscopy in combination with autofluorescent protein labeling of DC-SIGN allowing dynamic studies on living cells might provide the answers.

Chapter 4

Modeling the functional cell surface profile

Interactions between a cell and its surroundings are mediated by membrane proteins. Both expression level and spatial organization of these receptor proteins are important for their specific type of interaction. In this chapter, a model is presented that describes the probability of a cell to have a certain number of receptors joining the contact site in the initial encounter with an external object, e.g. another cell, virus or bacterium. The model considers the molecular density of the receptors on the cell and their spatial organization, i.e. clustered in domains or randomly spread as individuals. Monte Carlo simulations, based on the model, have been performed to investigate which parameters are determinant in the object-cell encounter. In addition to fixed simulation parameters, simulations were performed using distributions of domain size and content as measured for DC-SIGN. The simulations show that receptor clustering in domains is favorable to enhance the number of receptors hit by the object if the domain size becomes comparable to the size of the object. Moreover, an optimum exists for a specific object size and receptor density within the domains. In addition, the simulations indicate that the specific spatial organization of DC-SIGN on the membrane of imDCs optimizes the binding properties of imDCs.

4.1 Introduction

The plasma membrane forms the physical boundary between the cytosol of the cell and the extracellular environment. Membrane proteins mediate interactions between the cell and its surroundings, i.e. other cells or the extracellular matrix (ECM) [10]. The specific nature of the interaction is determined by the type, expression level and spatial distribution of proteins. In particular, the formation of molecular domains on the cell surface plays an important role in the functioning of the cell [193]. The concentration of specific molecules on the cell membrane can have direct consequences for cell function: 1) enhance or amplify molecular interactive properties; 2) induce conformational, and thus, functional changes; 3) include/exclude molecules from a specific region in order to enhance/prevent their cooperativity. In the last ten years extensive work has been devoted to the understanding of functional lipid microdomains or lipid rafts, defined by detergent solubility and sensitivity to cholesterol deprivation, which have been suggested to play a role in many cell functions [36, 185, 193–195].

The importance of membrane heterogeneity for proper cell functioning is observed in (directed) migration of cells, where cell adhesion receptors mediate binding to the molecules of the ECM or to counter-receptors on other cells [196]. For example, migrating leukocytes exhibit a polarized surface distribution while moving under the influence of a chemoattractant gradient. In this situation, the chemoattractant receptors and other receptor molecules accumulate at the leading edge of the cell, acting as the sensing side of the cell that guides the migration. At the trailing edge of the cell, adhesion molecules are concentrated in focal adhesions to bind other cells, e.g. endothelial cells [182, 197, 198]. This functional asymmetry of the cell membrane in combination with the dynamic actin network enables the cell to move forward.

Molecular domains have also been shown to facilitate entry of some pathogens, including viruses, parasites, bacteria and toxins into host cells [179, 191, 192]. In fact, Cambi et al. [184] have shown a direct correlation between the clustering distribution of the pathogen-recognition receptor DC-SIGN on the cell membrane and its capacity to bind and internalize virus-sized ligand-coated particles. Immature dendritic cells, exhibiting domains of DC-SIGN, were able to bind virus-like particles of 40 nm in diameter, while intermediate dendritic cells, having a random distribution of DC-SIGN on their surface, did not bind these particles.

Damjanovich and coworkers (see also Chapter 6) have observed nano-scale domains of signaling receptors (IL-2R and IL-15R) on the membrane of activated T lymphoma cells [199, 200]. Receptor clustering appeared to be associated with lipid rafts, suggesting that rafts might facilitate the formation of efficient signaling platforms on the cell membrane [193, 201].

These examples illustrate the wide variety of processes in which protein domains play a key role. Moreover, as each type of domain has its own specific properties and distribution on the membrane, as demonstrated in Chapters 3 and 6, it seems that Nature has optimized these parameters. We have developed a simple and general model that explains in physical terms the advantages of clustering and is able to relate domain size and molecular packing to its possible biophysical role. Specifically, the model describes the binding probability for a random encounter of a cell and an external object (another cell or a pathogen). By means of Monte Carlo simulations, we have addressed the following questions: 1) what is the most beneficial spatial organization for binding a particular object, randomly spread individual receptor molecules or clustered receptor domains?
2) does this organization depend on the size of the object? 3) what is the optimum molecular density and size of the domains? The results of the simulation are compared to the experimentally found DC-SIGN receptor organization on dendritic cells, as described in Chapter 3. In particular, we investigated realistic situations including distributions of domain sizes and the number of receptors within a domain.

4.2 Monte Carlo simulation of object - cell encounter

4.2.1 Model description

The model describes the encounter of an object and a cell surface in terms of the object size and the receptor distribution on the surface. Based on the model we describe the probability that an object interacts with a certain number of receptor molecules on a cell surface in case of a random object - cell encounter, as depicted in Figure 4.1. Although the membrane is a dynamic surface, we consider cells with a random, static distribution of either receptor domains or individual receptors covering the whole cell surface. This is valid as the model is focused on the initial moment of a object - cell encounter, not including any signaling or redistribution events of the cell membrane components that may occur directly after the engagement. In the model, the spatial distribution of the receptors on the object is considered fully covered and, an engagement of the object with a receptor on the cell surface always leads to a positive interaction, i.e. object - cell bond.

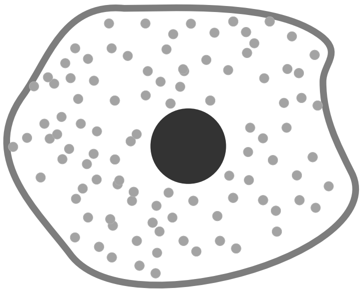

Figure 4.1: Top view of a random object - cell encounter. The cell surface is covered by individual, randomly distributed membrane receptor molecules (light gray dots). The finite sized circular object (dark gray) hits a number of receptors at the cell surface. For simplicity, the encounter is considered in two dimensions.

4.2.2 Analytical description

We first describe the model for a surface containing receptor domains, using an analytical expression. Consider a cell surface of area A_{total} covered with U randomly distributed receptor domains. The domain and the object have radius r_{dom} and r_{obj}, respectively. The probability that the object hits the domain is:
$P = (U\pi(r_{dom} + r_{obj})^2)/A_{total}$
Figure 4.2 depicts the situation in which the object partly overlaps the domain. The center to center distance between object and domain is d_N, with
$r_{dom} - r_{obj} \leq d_N \leq r_{obj} + r_{dom}$ for $\mathrm{r}_{obj} < \mathrm{r}_{dom}$.
The probability that the center of the object falls within distance d_N from the center of the domain is:

$$P = (U\pi \cdot d_N^2)/A_{total} \tag{4.1}$$

More specifically, we are interested in the probability for an object to hit a certain minimum number of receptors within the domain. For any situation in which the object hits a domain with a certain overlap, the probability is given by equation 4.1. The domain contains a number of N_{total} evenly distributed receptors. Thus, the number of molecules within the overlap area is: $N = A_{overlap}(d_N) \cdot \rho$, where ρ is the molecular density of each domain and $A_{overlap}(d_N)$ is given by equation 4.2, based on geometric calculations.

$$A_{overlap}(d_N) = r_{dom}^2 \arccos \frac{(d_N^2 - r_{obj}^2 + r_{dom}^2)}{2r_{dom}d_N} + r_{obj}^2 \arccos \frac{(d_N^2 + r_{obj}^2 - r_{dom}^2)}{2r_{obj}d_N} - \\ 0.5\sqrt{(-d_N + r_{dom} + r_{obj})(d_N + r_{dom} - r_{obj})(d_N - r_{dom} + r_{obj})(d_N + r_{dom} + r_{obj})} \tag{4.2}$$

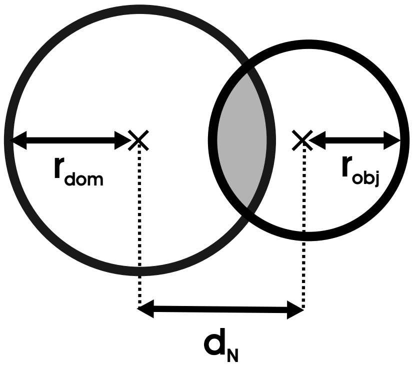

Figure 4.2: Domain with radius r_{dom} is hit by an object of radius r_{obj}, with $r_{obj} < r_{dom}$. The object starts overlapping the domain if $d_N = r_{dom} + r_{obj}$. The object partly overlaps the domain if: $r_{dom} - r_{obj} < d_N < r_{dom} + r_{obj}$. The object starts fully overlapping domain if: $d_N = r_{dom} - r_{obj}$

The probability to find N or more receptors in the overlap area is therefore the same as the probability to find the minimum overlap area ($A_{overlap}(d_N)$), being: $P = (U\pi(d_N)^2)/A_{total}$. This analytical model describes the hit probability for fixed domain sizes and content. To take into account a realistic situation with distributions of domain sizes and the number of receptors within a domain, we extended the analytical calculation with a Monte Carlo simulation.

4.2.3 Simulation

We have implemented the model in a Monte Carlo simulation. In each simulation step, a circular object encounters the cell surface at a random position. The surface contains randomly positioned receptors or receptor domains. If a receptor molecule is located within the area occupied by the object, we count one 'positive binding event', or one 'positive hit'. The number of positive hits *(N)* in each simulation step is then counted and added to build up an occurrence histogram as the simulation proceeds. This distribution shows occurrences up to $N = N_{max}$ binding events. The distribution is then successively integrated from a lower integration boundary N_{min} to infinity. The outcome for each value of N_{min} from zero to N_{max} yields a new distribution, containing the number of positive binding events that occur above a minimum (N_{min}). This type of distribution is also denoted 'cumulative relative frequency distribution' and shows the probability of a certain minimum number of positive hits to occur.

Figure 4.3 shows the geometric parameters of the simulation. The calculation area is surrounded by a buffer area, ensuring that all receptors or receptor domains fall randomly within the total area A_{total}, while avoiding edge effects in the calculation. Per calculation, the size of a receptor together with the surface fraction covered by receptors defines the total number of N_{max} receptors on the surface. These values are kept constant throughout all simulations, while N_{total}, r_{obj} and r_{dom} are variables. A simulation step starts with randomly positioning of N_{max} individual or clustered receptors in area A_{total}. Then, the overlap areas between domains and the object are calculated. Multiplication of each overlap area and the molecular density of a domain gives the number of receptor molecules involved in each overlap, i.e. the number of positive hits or binding events. In case a receptor molecule is positioned exactly at the edge of the object, the overlap is set at 50% (occurrence of 0.5). Finally all positive hits are summed.

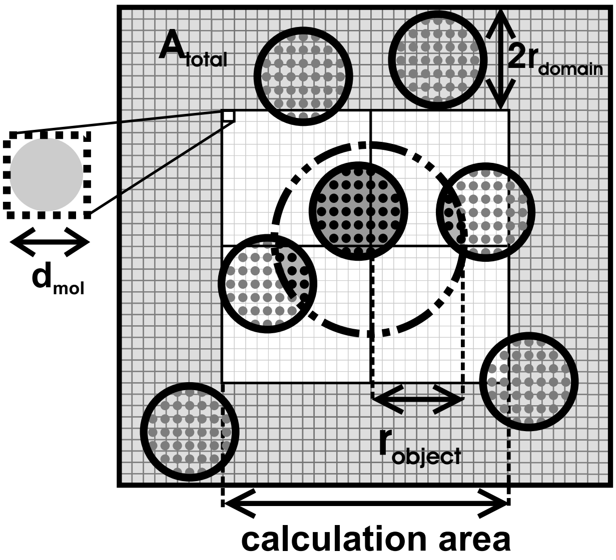

Figure 4.3: Two dimensional top view of an encounter between an object (circle with dash-dotted outline of radius r_{obj}) and a cell surface, containing a number of domains (solid outlines with radius r_{dom}). The square simulation surface has an area of A_{total}. The surface consists of a lattice with a unit cell of size d_{mol}. The overlap area between object and domain after the encounter is filled as dark gray. Each domain contains a number of N_{total} receptors (gray and black dots). Receptors located within an overlap area are 'positive binding events' or 'positive hits', indicated as black dots. To simulate a situation in which the cell surface consists of randomly spread individual molecules, N_{total} is set to one and $2r_{domain} = d_{mol}$.

Therefore, one simulation step consists of filling the area with receptors and calculating the number of positive binding events. During a simulation, individual simulation steps are repeated, building up an occurrence histogram and a cumulative relative frequency plot.

The added strength of Monte Carlo simulations is the possibility to randomly choose simulation parameters from a predefined data set, containing distributions of, for instance, domain sizes and/or content. In this case, for each simulation step the area is filled with randomly selected domains of certain size and density from the data set obtained in Chapter 3, until the maximum number of receptor molecules N_{max} is reached or exceeded.

4.3 Results

4.3.1 Individual receptors versus receptor domains

The simplest and most efficient way for a cell to distribute adhesion or other interactive receptor proteins on the cell membrane is likely to be a random distribution of individual molecules. Clearly, a random spread of molecules maximizes the chance for a receptor to participate in an accidental object - cell encounter. We have first performed a series of simulations to verify the effects of random and non-random spread of receptor molecules. Accidental encounters of an object and a cell were simulated, in which objects of different sizes encountered a surface containing either randomly distributed receptor molecules or molecules clustered in domains.

The first simulation encompassed an encounter of an object with $r_{obj} = 50\,\mathrm{nm}$ and a surface containing randomly distributed receptor molecules. A receptor density of 30 molecules/μm^2 was chosen, resembling the density experimentally found for the pathogen recognition receptor DC-SIGN, expressed on immature dendritic cells (imDCs) as discussed in Chapter 3. The object size is similar to the typical size of a virus, e.g. the human immunodeficiency virus (HIV) has a diameter of 80 - 110 nm [202]. The probability to have a minimum number of positive binding events in this object - cell encounter is shown by the dark gray solid line in Figure 4.4. The probability for the object to hit at least zero receptors is one and drops quickly to a low probability ($1{\cdot}10^{-3}$) for hitting two or more receptors. The number of positive binding events can become smaller than one in the simulation if the object hits the molecule only partially, explaining the non-integer values of the minimum number of positive binding events. The discrete character of the simulation results in a stepwise behavior of the probability, e.g. the probability changes dramatically going from a situation of an object hitting

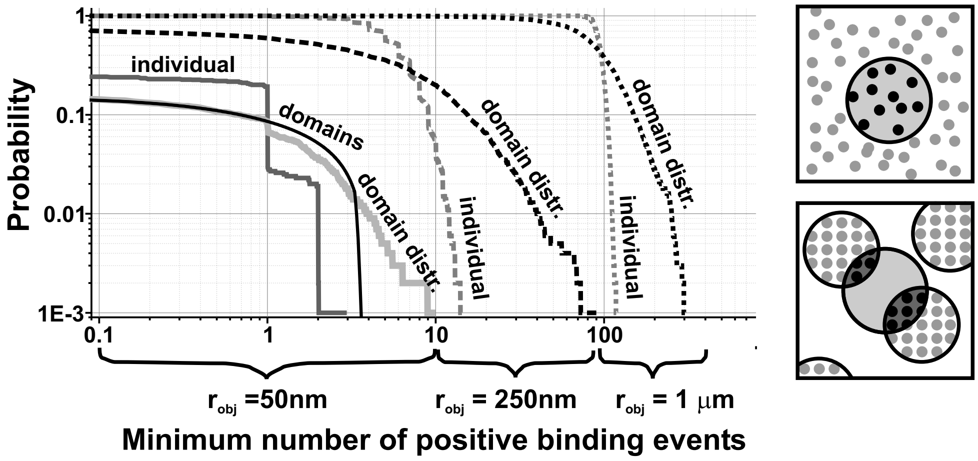

Figure 4.4: Cumulative relative frequency distribution of the hit probability as function of the type of receptor distribution (individual or domains) for three different object sizes: radii of 50 nm (solid lines), 250 nm (dashed lines) and 1 μm (dotted lines). The dark gray lines, denoted as 'individual' show the results for randomly distributed individual receptors. The black solid line, marked as 'domains', shows the the calculated probability for a fixed domain size and density. The lines denoted with 'domain distr.' correspond to Monte Carlo simulations using distributed domain parameters, i.e. size and content. The upper cartoon on the right schematically shows an object (gray circle) hitting a membrane, which contains randomly positioned molecules (gray dots). Molecules that are hit by the object are colored black. The lower cartoon shows the same object hitting a membrane with clustered molecules, where the overlap area is colored dark gray.

at least 1 receptor to a situation in which the object hits at least 1.1 receptors as in the latter case the object hits in fact two receptors simultaneously.

To compare the simulation of a random distribution of individual molecules with a domain type of distribution, we first have used the analytical description of the probability. The probability for an object of $r_{obj} = 50\,\text{nm}$ to hit more than a particular number of receptors on the cell membrane is calculated using equation 4.1. In the calculation we assume domains of $r_{dom} = 90\,\text{nm}$ in size, containing $N_{total} = 12$ molecules per domain and a domain density of $U = 2.53\,\text{domains}/\mu\text{m}^2$. The resulting probability curve is shown in Figure 4.4. Comparison of the simulation with randomly spread receptors and the calculation for a domain type of distribution shows that a membrane with randomly spread individual molecules has the highest hit probability. This is consistent with our general hypothesis, i.e., a random distribution maximizes the chance for the object to hit anything. Interestingly, the two curves cross each other. This crossing point indicates a binding threshold, i.e. if the binding strength required to sustain a stable object - cell bond is larger than the threshold, then clustering results in a higher hit probability and will be beneficial with respect to randomly distributed individual molecules.

We then performed Monte Carlo simulations for the same object radius and surface receptor density ($30\,\mathrm{molecules}/\mu\mathrm{m}^2$), using distributed domain parameters, i.e. distributions of domain size and molecular density within a domain, from the experimental data set as obtained from NSOM experiments of DC-SIGN on the imDC membrane (Chapter 3). The average values for the distribution parameters were $r_{dom} = 90\,\mathrm{nm}$, $N_{total} = 12$ molecules per domain and $U = 2.53\,\mathrm{domains}/\mu\mathrm{m}^2$. The probability plots for three different object sizes are shown in Figure 4.4. The result for $r_{obj} = 50\,\mathrm{nm}$ is similar to the calculated probability up to a minimum number of three positive binding events. Above this value, the simulation crosses the calculated line and shows a higher probability, reaching even more (up to ten) binding events per encounter. This is explained by the fact that the calculation was done for fixed domain characteristics, whereas in reality the cell has a whole distribution of domain sizes and content including larger an denser packed domains, which enables more hits.

The results for object sizes of $r_{obj} = 250\,\mathrm{nm}$ and $r_{obj} = 1000\,\mathrm{nm}$ show that the hit probability increases and shifts to higher values with increasing object sizes. In addition, the relative difference between random and clustered organization becomes less pronounced with increasing object size. Thus, clustering seems to be of particular importance for binding objects of sizes comparable to the domain size.

4.3.2 Domain size and packing density

Having established the advantage of domains over randomly distributed individual receptors for comparable object and domain sizes, we next studied the effect of domain properties, such as size and molecular packing density, on the hit probability for an object size of $r_{obj} = 50\,\mathrm{nm}$. In the first set of simulations, the domain size was kept constant ($r_{dom} = 90\,\mathrm{nm}$) while the number of receptor molecules per domain (N_{total}) was varied by about two orders of magnitude, i.e. from 3 to 100 receptors. Accordingly, the mutual distances between receptors changed from $r_{intra} = 48\,\mathrm{nm}$ to $r_{intra} = 8\,\mathrm{nm}$. As the total number of receptors available was kept constant, the number of domains on the surface decreased with increasing molecular density. The results of the four simulations are shown in Figure 4.5(a) and indicate that for low receptor densities the hit probability is high and decays fast, whereas high densities have a lower probability to hit something but ensure larger and higher hit ranges.

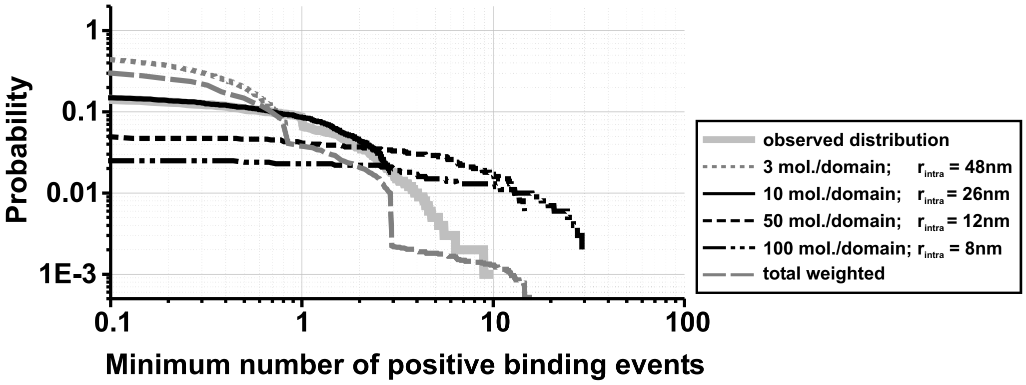

(a)

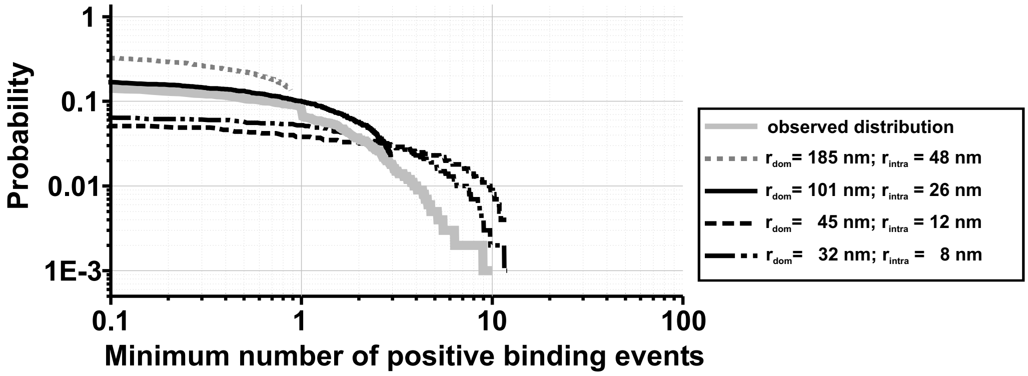

(b)

Figure 4.5: The influence of the domain properties on the hit probability. Cumulative relative frequency distributions with a fixed object size of $r_{obj} = 50\,\text{nm}$. (a) Hit probability for simulations with a fixed domain size ($r_{dom} = 90\,\text{nm}$) and varying number of receptors per domain (3 to 100 receptors/domain). The dashed gray line, denoted as 'total weighted', shows the plot of four simulations which are weighted according to the density occurrences measured for the DC-SIGN domain distribution (shown in Chapter 3). (b) Hit probability for simulations with varying domain sizes and a fixed number of receptors per domain ($N_{total} = 12$). In (a) and (b) the gray solid lines ('observed distribution') show the probability distribution for distributions of domains size and packing density.

In fact, Figure 4.5(a) illustrates the transition from an individual type of distribution, resembled by 3 receptors/domain, to a domain type of distribution.

In the second set of simulations, the receptor density was changed by changing the domain size. The object size was fixed at $r_{obj} = 50\,\text{nm}$. To fix the number of domains per area, the number of receptors per domain was kept constant at 12 receptors and the total receptor coverage at 0.048 %. The domain radius was varied from $r_{dom} = 185\,\text{nm}$ to $r_{dom} = 32\,\text{nm}$, which corresponds to similar intermolecular distances (r_{intra}) as in the previous simulations. For $r_{obj} < r_{dom}$, i.e. $r_{dom} = 185$ and 101 nm, the trends are similar as observed in Figure 4.5(a). Thus, domains with low receptor densities achieve a high hit probability but reach only a low number of hits, whereas high receptor densities ensure a larger and higher hit range at lower probability values. In case $r_{obj} > r_{dom}$, i.e. $r_{dom} = 45$ and 32 nm, the minimum number of hits that can be reached is limited. This can be seen for instance by comparing the graphs of $r_{intra} = 8\,\text{nm}$ in Figure 4.5(a) and Figure 4.5(b): the number of positive binding events in (a) can become thirty, while in (b) the number of positive binding events is limited to about ten. Thus, if the object is larger than the domains, the only way for the cell to achieve a larger number of positive binding events would be by packing the receptors more densely. Naturally, there is a physical limit for the packing of the receptors, ultimately given by the size of the receptors. Therefore, if the domain becomes slightly smaller than the object, the domain properties restrict the number of possible binding events. If the domain becomes slightly larger than the object, the domain packing capacity as well as the object size restrict the number of possible binding events. To maximize its binding capacity it is more favorable for the cell to keep the domain size larger than the smallest object size it needs to bind. In this case, it makes no difference in probability how a certain domain density is obtained, either by changing domain size or by content.

For comparison, the probability distribution for an accidental encounter of a cell surface containing domains with distributed size and packing density as measured for DC-SIGN and an object (r_{obj} =50 nm) is shown in Figure 4.5(a). It is notable that this graph equals to a certain extent the results of the simulation in which an object encounters a surface containing domains with a fixed molecular density of 10 receptors per domain also shown Figure 4.5(a). This is due to the fact that the fixed molecular density used is similar to the mean value of the measured distribution. Like the calculated graph in Figure 4.4, higher hit values are lacking in case of fixed domain properties. The distribution of DC-SIGN domains contained a high percentage (48% and 42%) of low density domains (3 and 10 receptors per domain respectively) and a low percentage (5%) of higher densities (50 and 100 receptors per domain). By applying the corresponding weight factor to the probability plots of fixed domain properties (3, 10, 50 and 100 receptors per domain) and adding all plots, a total weighted graph was created in Figure 4.5(a). As expected, the weighted graph resembles the probability curve with the measured DC-SIGN domain distributions, demonstrating that the cell makes use of a variety of molecular densities to achieve a high hit probability as well as a large range in the number of positive hits.

4.3.3 Optimization of the domain distribution

So far, it has been shown that the cell can optimize its domain properties for an object - cell encounter with a small object to assure a certain minimum number of positive hits, i.e. possible binding sites. Next, we searched for the optimum domain density and spatial domain distribution to bind a small object with $r_{obj} = 50\,\mathrm{nm}$ at a given receptor density on the surface (30 receptors/μm^2). By varying the domain content by two orders of magnitude, i.e. from 3 to 270 receptors/domain, the domain density on the surface changed from ~ 10 domains/μm^2 to ~ 0.11 domains/ μm^2. The inter-domain distances (r_{inter}), measured from center to center, are obviously dependent on the domain density, thus the mean inter-domain distances varied from $r_{inter} \sim 150$ to 1500 nm, by varying the domain content. We performed binding simulations for 19 different receptor densities within the specified range of inter-domain distances and a constant domain size of $r_{dom} = 90\,\mathrm{nm}$. Making use of the fact that the hit probability is a function of the minimum number of binding events and the domain properties, we plotted the probability as a function of the domain density for different values of the minimum number of binding events (N_{min}) as shown in Figure 4.6(a). To hit at least 10 receptors, a molecular density of ~ 90 receptors/domain is needed. Therefore, the graph of $N_{min} = 10$ hits starts at $r_{inter} \sim 850\,\mathrm{nm}$. In all four graphs, the hit probability decreases for increasing inter-domain distances, i.e. increasing molecular packing density. This is true for all N_{min} values because the high packing density of the domains leaves behind large uncovered areas, reducing the hit probability. In case less than four positive hits are necessary for stable object - cell binding, the hit probability exhibits a peak, indicating that the specific combination of inter-domain distribution and molecular content is optimal to bind an object of 50 nm with at least $2, 3$ or 4 hits. At smaller inter-domain distances, the molecular density per domain is too low to establish enough positive hits and thus achieve a sufficient binding strength (larger than $N_{min} = 2$).

We performed a second set of similar simulations in which the object size was increased to $r_{obj} = 250\,\mathrm{nm}$, shown in Figure 4.6(b). An optimum is observed for $N_{min} = 10$ hits, corresponding to an inter-domain distance of $\sim 425\,\mathrm{nm}$ and 20 receptors/domain. The graph with threshold $N_{min} = 3$ hits, shows that if only

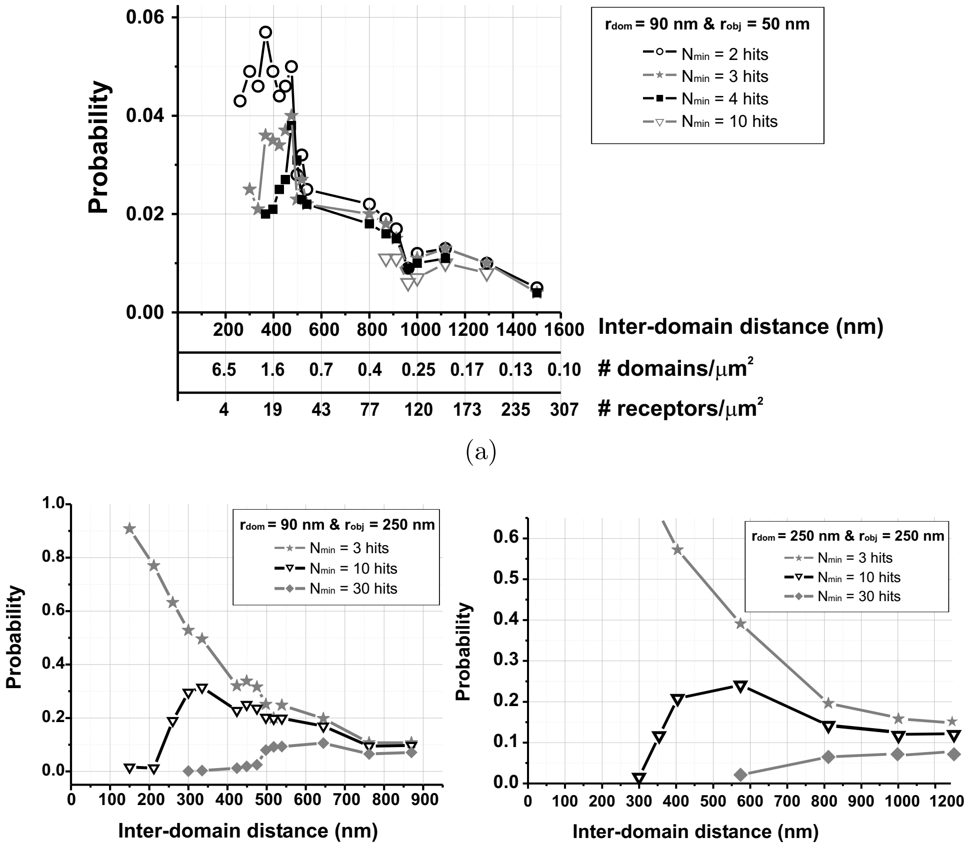

(a)

(b)

(c)

Figure 4.6: Optimum domain distribution for object - cell binding. Probability to hit more than $N_{min} = 2, 3, 4, 10$ and 30 receptors as a function of the inter-domain distance. The plots are derived from encounter simulations of domains with fixed object and domain sizes with varying domain densities. (a) Probability plot with $r_{dom} = 90$ nm and $r_{obj} = 50$ nm. For convenience, the equivalent values for the domain density and the number of receptors per domain are given in the lower axes. (b) Probability plot with $r_{dom} = 90$ nm and $r_{obj} = 250$ nm. (c) Probability plot with $r_{dom} = r_{obj} = 250$ nm.

few molecules are sufficient to establish a successful object - cell bond, many domains with a low receptor density at small inter-domain distances are preferential. As an extreme case, randomly distributed molecules are preferential in case of a small N_{min} (about one). Figure 4.6(c) shows the probability as function of the inter-domain distance in case both the object and domain are large, i.e. $r_{obj} = r_{dom} = 250$ nm. The trends are similar to Figure 4.6(b), although the optimum for $N_{min} = 10$ hits is shifted to $r_{inter} \approx 600$ nm, i.e. higher receptor density.

4.4 Discussion

The simulations of a random object - cell encounter with different types of molecular surface distributions indicate that the basic binding properties of a cell are dependent on the combination of the object size and the spatial organization of receptor molecules on the cell membrane. More specifically, molecular receptor domains are beneficial in order to increase the number of possible bonds if their size becomes comparable to the size of the object, as demonstrated in Figure 4.4. In all simulations, receptors or receptor domains were considered randomly distributed on the cell surface. The same figure showed that for large object sizes, the spatial distribution of receptors on the cells becomes less critical, due to a larger contact area between object and cell which ensures good overlap with a large number of receptor molecules. The cartoon in Figure 4.7 illustrates the effects of a random and a clustered type of organization of receptor molecules on the cells capability to bind small and large objects.

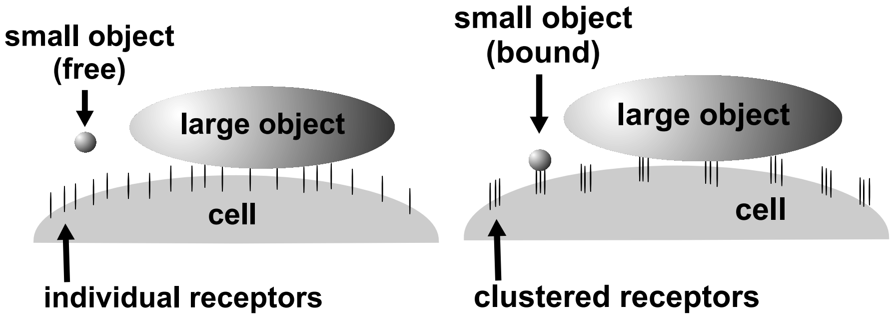

(a) (b)

Figure 4.7: (a) A large contact area ensures multiple interactions with randomly spread individual receptor molecules. As a small object can not bind many receptors simultaneously, it is not capable to obtain stable object-cell binding. (b) A clustered type of receptor distribution ensures multiple bonds for both large and small objects, enabling binding of both types of objects.

Recently, the relation between the spatial distribution of surface receptors and the binding capacity of cells was experimentally demonstrated for dendritic cells [184]. In the experiment, 40 nm polystyrene beads, mimicking the size of a virus, were coated with the human immunodeficiency virus (HIV) envelope protein gp120. Whereas imDCs, having the pathogen recognition receptor DC-SIGN organized in a clustered way (see also Chapter 3) were able to bind the beads, intermediate developed DCs, having randomly distributed individual DC-SIGN on their surface, did not bind the beads. Interestingly, both cell types did bind gp120 - coated particles of 1 μm in diameter as a result of the large contact area of the 1 μm particle which always accounts for multiple DC-SIGN - gp120 interaction sites, regardless of the spatial organization.

From both our simulations and the binding experiments it follows that domains appear necessary to bind small objects, suggesting that imDCs solve the problem of the small contact area of most viruses by locally increasing the DC-SIGN density. Our simulations show that the combination of a large range in packing density plus a specific domain size, as seen for DC-SIGN, is ideal to optimize the pathogen binding capability of imDCs. First, the cell exploits the large range in receptor densities to profit both the high hit probability and a large hit range. Second, the observed DC-SIGN domain size ($r_{domain} \sim 90$ nm) is slightly larger than the smallest virus particles ($r_{object} \sim 20$ nm) that bind to DC. This is favorable for the number of positive hits in an encounter as this number is limited by the virus size. Because the domain sizes influence the binding probability for small objects, we hypothesize that the domain size is specific for these small objects.

Using Figure 4.5 it was shown that for $r_{obj} < r_{dom}$, the origin of packing density, i.e. a change of the number of receptors or the domain size, did not significantly influence the hit probability. However, if $r_{obj} > r_{dom}$, the domain packing density and the domain size restrict the maximum number of hits. Interestingly, DC-SIGN domains on imDCs showed a large spread in molecular packing density, mainly caused by a high variety in number of DC-SIGN receptors. Apparently, it is favorable for the cell to vary the domain contents rather than the size. This hints to an external mechanism driving domain formation instead of the molecules themselves. Since the simulations show that there is no apparent difference in how to change density (for $r_{obj} > r_{dom}$), it appears that the domain formation is related to the size of the object.

Figure 4.6 shows an interesting aspect on the threshold values. To achieve at least $2, 3$ or 4 simultaneous hits, there is an optimum for an inter-domain distance of $r_{inter} \sim 425$ nm. This value corresponds to a molecular density of ~ 20 receptors per domain with $r_{intra} \sim 18$ nm. These numbers are in very good agreement with measurement data of DC-SIGN domains from chapter 3, i.e. $r_{inter} \sim 450$ nm and a mean value of ~ 10 molecules per domain. Apparently the imDC has also optimized the spatial distribution of DC-SIGN to obtain the highest probability of binding. Because the optimum vanishes for higher threshold values, we propose that there is a preferred threshold value for the number of possible binding events. This value is larger than one because the cell forms domains, and smaller than four, according to Figure 4.6.

Our results explain some aspects of the good binding capability of immature dendritic cells (imDCs) to various types of objects using DC-SIGN. This molecule contains a carbohydrate recognition domain (CRD) [166] that has a high affinity for various envelope proteins of pathogens, e.g. gp120, E2, E and GP proteins on the human immunodeficiency virus (HIV-1) [162], Dengue virus [168], Cytomegalo virus (CMV) [169], Ebola virus [170] and Hepatitis C virus [171, 172], respectively. In addition, imDCs are also able to bind microbacteria, such as Leishmania [173], Candida Albicans [174] and mycobacterium [175–177]. As the simulations showed a dependence between the size of the object and the cells binding capability, an overview of sizes and morphology of pathogens that can bind to imDCs is given in Table 4.1. Note that the average diameter of a DC-SIGN domain is ~ 185 nm, similar to the typical size of a virus.

pathogen	**diameter**	**shape**
HIV-1	70 - 110 nm	icosahedral
Dengue	40 - 60 nm	spherical
Cytomegalovirus	130 - 200 nm	icosahedral
Ebola	0.7 - 1.4 μm × 10 nm	rod
Hepatitis C	40 - 50 nm	spherical
leishmania	2.5 - 5 μm	spherical
candida	2 - 7 × 3 - 8 μm	oval
mycobacterium TBC	$\sim 0.3 \times 3\mu$m	rod

Table 4.1: Sizes and shapes of viruses [203] and bacteria [204, 205] that can bind to imDCs.

Although the affinities of DC-SIGN to a glycoprotein as gp120 and E2 are high, i.e. 1.3 nM [206] and 3 nM [171] respectively, on-off rates of individual bonds may require more than one binding event to maintain a stable virus-cell bond. From Figure 4.4 a threshold value was found for the minimum number of positive events, which indicated that if more positive binding events are needed for a stable cell-object bond, the receptors have to be clustered in domains. Thus indirectly, the threshold value provides information about the object to be bound in terms of size and affinity. The threshold values that we have estimated in our simulations may deviate from the real number of possible binding events that are needed for successful binding for several reasons. First, in the simulations the envelope of the pathogen, i.e. the object, is considered fully covered with envelope proteins. Regarding the pathogen sizes in table 4.1, the protein coverage of the pathogen's envelope is likely to be more critical for viruses than for bacteria.

Therefore, we will focuss on the viruses in table 4.1, which have a well defined structure, containing evenly dispersed surface projections of envelope proteins. For example, the HIV-1 envelope contains 72 glycoprotein trimers (with gp120) on its surface and the Dengue surface contains 90 glycoprotein dimers [207]. DC-SIGN binds to both type of protein 'spikes'. Considering the size of these virions, the protein spikes are distributed at a mutual distance of typically 5 - 10 nm. Also the morphology of Ebola is known to contain glycoprotein spikes at a typical distance of 10 nm [203]. In contrast, the average nearest neighbor distance of individual DC-SIGN receptors is about 40 nm, as estimated in Chapter 3, Figure 3.7. Therefore, in this case, the DC-SIGN density seems to form the bottleneck rather than the density of the envelope proteins. Second, on-off rates of individual protein bonds are not considered. On-off rates are particularly important for binding small objects, because their small contact area can lead to only a few bonds. This may cause an overestimation of the number of bonds. Third, cooperative effects, such as multiple binding sites, oligomerization or steric hindrance effects are not considered in this simple model. It is known that cooperativity plays a role in the functioning of DC-SIGN, as recent in vitro studies have shown that the extracellular domain of DC-SIGN enables the formation of tetramers, enhancing the affinity to certain viruses [171, 181]. In addition, steric hindrance effects occurring after tetramer formation, ensure selectivity [171, 208] and may lead to a deviation of the found threshold values.

4.5 Conclusion

We have developed a simple model that describes the probability of a cell to have a certain number of molecules joining the contact site in the initial encounter with an external object. Simulations of our model have shown that receptor clustering is particularly favorable to enhance the hit probability in a random object - cell encounter if the domain size becomes comparable to the size of the object. To bind objects with a large contact area, the precise receptor distribution on the cell surface has only minor influence. The simulations have shown that there is an optimum receptor distribution for the very first stage of cell - pathogen binding, considering the number of domains, the number receptors per domain and the minimum number of required receptors. The simulations support the hypothesis that the specific spatial organization of DC-SIGN on the membrane of imDCs, as measured in Chapter 3, is optimized for the pathogen - binding properties of imDCs. In particular, as a single receptor can not establish a stable binding due to the on-off rate of the bond, the cell can ensure stable binding by domains. Therefore, Nature seems to optimize the spatial organization of receptors on the membrane, while minimizing their production. After the first contact, many other processes may take over to enhance, stabilize, or utilize the binding, like cooperativity [209] and protein recruitment [187]. Nevertheless, success of the initial binding is highly dependent on the geometric organization of the receptors on the cell membrane.

Chapter 5

Counting and localizing single molecules by photobleaching

Discrete photobleaching, leading to the sudden termination of fluorescence is recognized as one of the clear signatures of an individual fluorescent molecule. This chapter demonstrates how photobleaching can be used to determine the molecular stoichiometry of densely packed areas, i.e. counting the number of single molecules. Furthermore, successive bleaching of a sequence of NSOM images has been used to resolve densely packed areas, allowing localization and reconstruction of the position of individual molecules on the membrane of dendritic cells with nanometer accuracy.

5.1 Introduction

The spatial resolution of any optical microscopy method sets an upper limit to the molecular density that allows identification of single molecules. To enable single molecule detection with NSOM, for instance, the molecular density should be typically less than about $100\,\text{molecules}/\mu\text{m}^2$. In Chapter 3, the spatial organization of receptor domains on the membrane of immature dendritic cells (imDCs) was investigated using NSOM. Because of the high packing density, no individual molecules could be resolved within the domains. As a consequence, the fluorophore density of each domain was estimated using both the integrated intensity of the domain and the typical single molecule intensity as determined from a single molecule intensity distribution. Furthermore, assuming that the labeled proteins were randomly distributed within the domain, the average intra-domain distance was estimated. Obviously, a more direct method to gain insight into the real spatial construction of these domains is desirable. Identification of individual fluorescent molecules within densely packed areas is only possible if the molecules under study exhibit unique optical characteristics, such as distinct spectral properties or different fluorescent lifetimes, which can be used for imaging [148, 150, 210, 211]. Here we demonstrate how photobleaching, as a unique time dependent single molecule property, can be used to resolve molecules, allowing direct measurement of the molecular stoichiometry of a packed system. Thus, without assumptions or intensity averaging, molecules are isolated and counted within densely packed regions. Moreover, in this chapter we will make use of successive photobleaching to accurately determine the position of molecules in densely packed areas, using the fact that the molecules also exhibit a unique spatial position.

Photobleaching is the irreversible change in molecular structure due to a photochemical reaction, causing the molecule to stop emitting and/or absorbing photons [89, 98]. In practice, for molecules in aqueous solution at room temperature photobleaching occurs after emission of roughly 10^6 photons, limiting the observation time to a few seconds [94]. Figure 5.1 shows a typical time trajectory of the fluorescence emitted by a single molecule, exhibiting one irreversible photobleaching step at time $t = 17\,\text{s}$, after emission of $\sim 1.5{\cdot}10^6$ photons. Despite its obvious disadvantage, one can exploit photobleaching to count the number of fluorophores within the illumination spot, e.g. to determine the number of individual chromophores in multichromophoric systems [212–214] or to determine the number of closely packed autofluorescent molecules in a living cell [107].

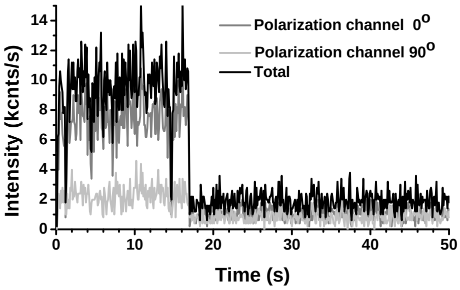

Figure 5.1: Fluorescence time trajectory of a single molecule (Cy5) measured on two perpendicular polarization channels at an excitation intensity of 600 W/cm^2. The total emitted fluorescence count rate (black line) is obtained by adding the signals of the two channels.

5.2 Stoichiometry: counting single molecules

A typical system where one gets confronted with closely packed fluorophores is a fluorescently labeled antibody, which usually contains 1 - 5 fluorophores. Obviously, both the average labeling efficiency, i.e. fluorophore to antibody ratio, and its distribution are important to quantify the number of antibodies and thus the number of proteins in a fluorescence image. To address this issue we have estimated the labeling efficiency by imaging isolated Cy5-labeled antibodies and recording their fluorescence emission in time.

Figure 5.2(a) shows a near-field image of Cy5-labeled antibodies (goat anti - mouse, (Immunotech - Beckman Coulter, Marseille, France) on a glass substrate at a concentration of ~ 4 antibodies/μm^2. The antibodies were attached to the glass substrate using Poly-L-Lysine and then critical point dried, following a similar sample preparation as described in Chapter 3. The image in Figure 5.2(a) exhibits single molecule fluorescence spots, as evidenced by discrete photobleaching and fluorescence blinking. The average count rate detected from a single Cy5 molecule was 8 kcnts/s at 600 W/cm^2 excitation intensity.

Figure 5.2(b) shows the time dependent fluorescence signal of the spot encircled in Figure 5.2(a). The two successive photobleaching steps, with a step size of 8 kcnts/s, indicate the presence of two Cy5 molecules within the illumination spot.

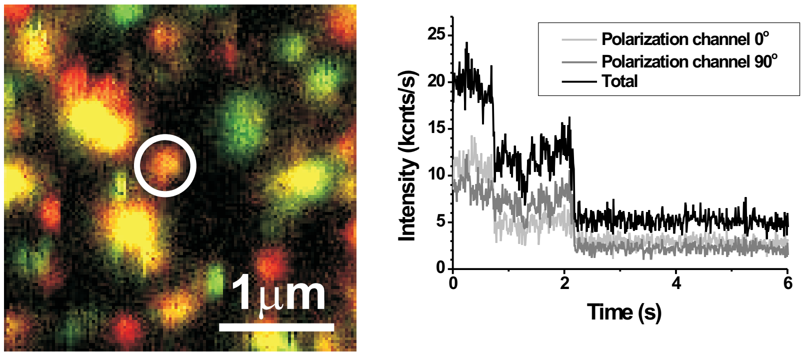

(a) (b)

Figure 5.2: (a) Near-field image of Cy5-labeled antibodies with a scan size of $3 \times 3\,\mu\text{m}^2$ (256×256 pixels) and excitation intensity of $\sim 600\,\text{W/cm}^2$. (b) Time trajectory of the bright encircled fluorescent spot in (a) at 2 ms acquisition time (binning 100 ms) with polarization contrast.

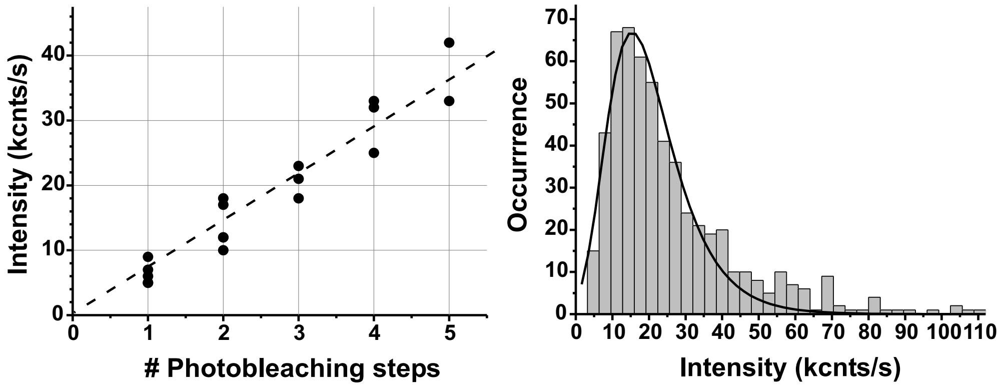

(a) (b)

Figure 5.3: (a) Average intensity of fluorescent spots (individual antibodies on glass) as function of the number of photobleaching steps, i.e. the number of Cy5 molecules. Every black dot corresponds to a fluorescent spot. (b) Intensity distribution of 552 fluorescent spots from seven different confocal images.

Similar samples containing Cy5-labeled antibodies on a glass substrate at a concentration of $\sim 2\,\text{antibodies}/\mu\text{m}^2$ were also imaged with confocal microscopy. Fluorescence time trajectories of about 20 spots were recorded with 0.5 ms acquisition time. For each time trajectory, the number of photobleaching steps was counted and related to the integrated intensity of the spot after background subtraction. The correlation between spot intensity and number of photobleaching steps is shown in Figure 5.3(a). The slope of the linear fit in Figure 5.3(a) indicates an average single molecule count rate of 7.5 kcnts/s at $600\,\text{W/cm}^2$ excitation intensity.

The average intensity of 552 diffraction limited fluorescent spots was measured and included in the intensity distribution of Figure 5.3(b). As the number of fluorophores per area in the images matches the concentration of the antibody solution, each fluorescent spot is attributed to one antibody. Therefore, the intensity distribution gives insight into the labeling efficiency of the antibodies. Using the average single molecule intensity, the intensity count rates in Figure 5.3(b) are converted to the number of Cy5 molecules. The distribution has a width of 18.4 kcnts/s and a mean value of 25.6 kcnts/s, corresponding to a width of 2.3 Cy5 molecules and an average of 3.2 Cy5 molecules per antibody.

Quantitative analysis by photobleaching on cells

In contrast to the relatively low number of fluorophores attached to an antibody as discussed in the previous section, Figure 5.4(a) shows the fluorescence image of a T cell, containing domains of densely packed labeled membrane proteins. Figure 5.4(b) shows a time trajectory of one of these domains.

During the first 20 seconds, the high fluorescence intensity decays exponentially, similar to the photobleaching of a bulk sample. With the decrease in intensity, the photon shot noise also decreases as it is proportional to the square root of the number of photons counted. After 21 seconds, the shot noise has become low enough to distinguish discrete steps in the time trace. Each step, with a mean step size of ~ 2 kcnts/s is caused by photobleaching of one Cy5 molecule, at $200\,\text{W/cm}^2$ excitation intensity. Note that the excitation intensity used is lower than in the previous experiments (see Figure 5.1- 5.3), causing a lower single molecule count rate. Eight single molecule steps are distinguished.

A similar stoichiometry analysis was performed on time trajectories of fluorescent spots imaged on dendritic cells. In each time trace the number of discrete steps was counted. Obviously, in case of high intensity spots, the number of steps could only be counted below a certain intensity, which in most cases corresponded to seven or eight remaining fluorescent molecules. Then, the intensity difference between the top level of the first step and the background signal was plotted

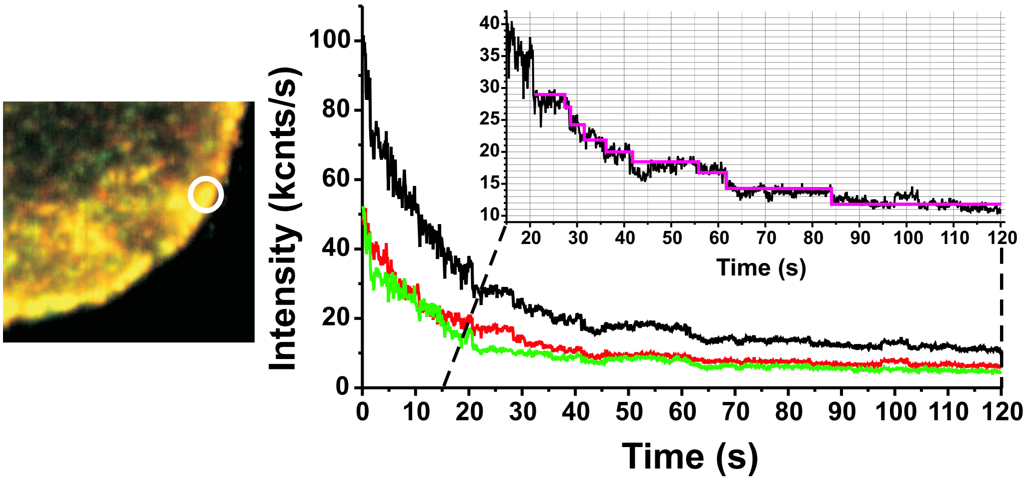

(a)

(b)

Figure 5.4: (a) Near-field image of a T cell containing Cy5-labeled IL15Rα membrane proteins (see also Chapter 6). The image was acquired at an excitation intensity of $\sim 200\,\mathrm{W/cm^2}$ with a scan size of $5 \times 5\,\mu\mathrm{m}^2$ (256×256 pixels). (b) Fluorescence time trajectory of the spot marked with the white circle in (a). The black graph shows the total signal of the two orthogonal polarization channels (red and green graphs). Discrete photobleaching steps are indicated by the red line in the zoom in of the time trace between $t = 20$ and $120\,\mathrm{s}$.

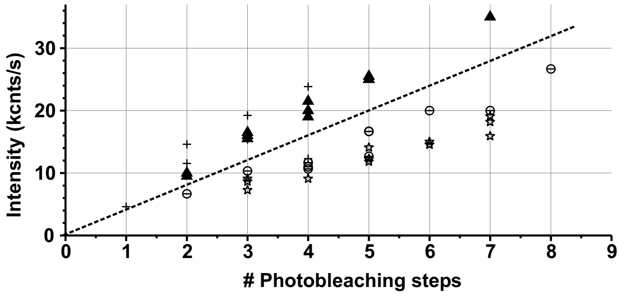

Figure 5.5: Intensity difference between the first step in the time trace of a fluorescent spot and the background signal as a function of the number of discrete steps. The spots were measured with NSOM on the cell membrane of four different dendritic cells containing Cy5-labeled DC-SIGN. Each cell is coded by a different symbol in the graph. The dashed line indicates the average linear fit of all four measurements, with a slope of $4.0 \pm 1.6\,\mathrm{kcnts/s}$ at an excitation intensity of $500\,\mathrm{W/cm^2}$.

as a function of the total number of counted photobleaching steps, as shown in Figure 5.5. From Figure 5.5 it follows that the average intensity of a single Cy5 molecule, labeled to DC-SIGN via antbodies, is ∼4 kcnts/s at an excitation intensity of 500 W/cm^2.

Reconstruction of molecular domains

We have extended the stoichiometry analysis to densely packed areas, larger than the illumination spot. Figure 5.6 shows one confocal and two near-field zoomed in images of Cy5-labeled DC-SIGN proteins, clustered in domains on the membrane of a dendritic cell. Although NSOM reveals more details than confocal microscopy, still the fluorophores within the domains are too densely packed to be distinguished individually. Therefore, we have successively imaged the area shown in Figure 5.6(c) in order to resolve the individual fluorophores within the crowded areas A and B after successive photobleaching. The sequence of NSOM images is shown in Figure 5.7.

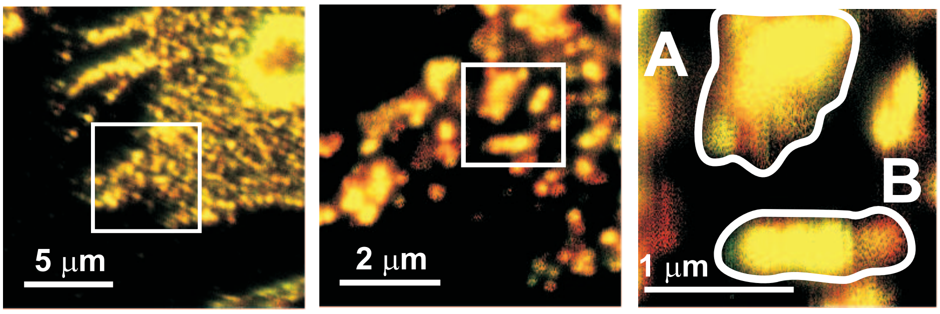

(a) (b) (c)

Figure 5.6: (a) Confocal image of Cy5-labeled DC-SIGN on the membrane of a dendritic cell. Scan size is 17× 17 μm^2 (256 × 256 pixels). The fluorescence signal is color-coded according to the detected polarization, red= 0 °, green = 90°. (b) Near-field zoom in of the white boxed area in (a) of 6× 6 μm^2 (256 × 256 pixels). (c) Near-field zoom in of the white boxed area in (b) of 2× 2 μm^2 (256 × 256 pixels).

As the intensity decreases, individual fluorescent entities become visible (e.g. see frame 16 of Figure 5.7, domain A) and finally discrete photobleaching of individual molecules is observed. Thus, the fact that the molecules bleach at different locations and different moments in time enables unraveling of the molecular content of the domain. For each frame, the integrated intensities of domains A and B are plotted in Figure 5.8 as black symbols. The resulting graphs resemble regular time trajectories, though measured over a large area with a long integration

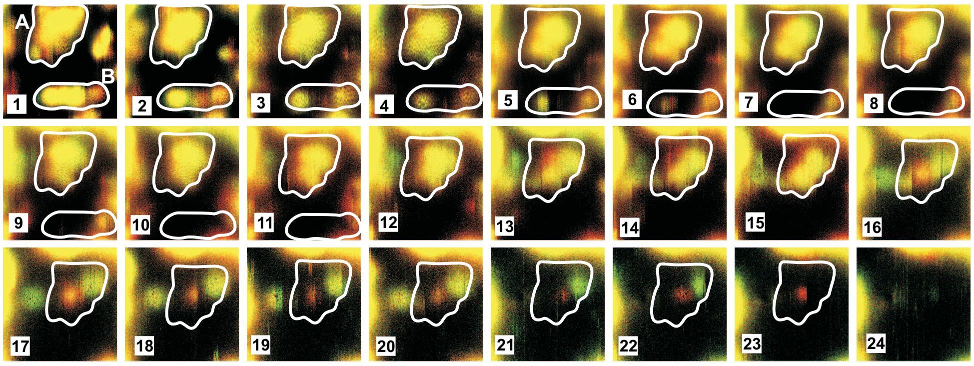

Figure 5.7: Sequential imaging (24 frames in total) of the same area of $2 \times 2\,\mu\mathrm{m}^2$ (256×256 pixels) on a dendritic cell, containing DC-SIGN proteins attached to Cy5-labeled antibodies. The integration time per pixel was 5 ms. Excitation intensity was $500\,\mathrm{W/cm}^2$. To guide the eye, the contours of two molecular domains (A and B) are drawn. For optimal visualization, the intensity is scaled per image, enabling to discriminate single molecules in the final images.

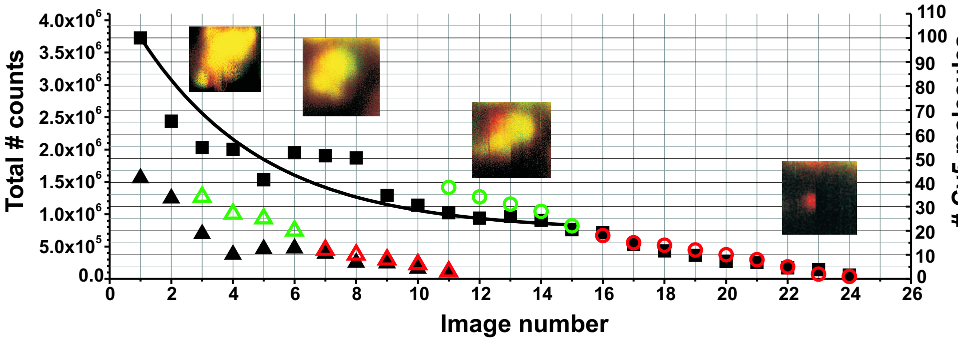

Figure 5.8: Domains A and B described in terms of intensity (left vertical axis) and number of Cy5 molecules (right vertical axis) as function of the frame number. The black data points (see left y-axis) are measured by integrating the intensity of the domain in each image (domain A:circles; B:triangles). The black line shows a mono-exponentially decaying fit for the intensity decrease in the first 15 frames. The red and green data points show the number of Cy5 molecules (see right vertical axis). The red data points are measured by counting the number of bleached molecules from the intensity images. The green data points are measured by counting the number of bleached molecules from the difference between successive images. Using the total integrated intensity of a single molecule of ~35000, the left and right axis show the same intensity range. Frames 1, 7, 13 and 23 of domain A are shown in the insets.

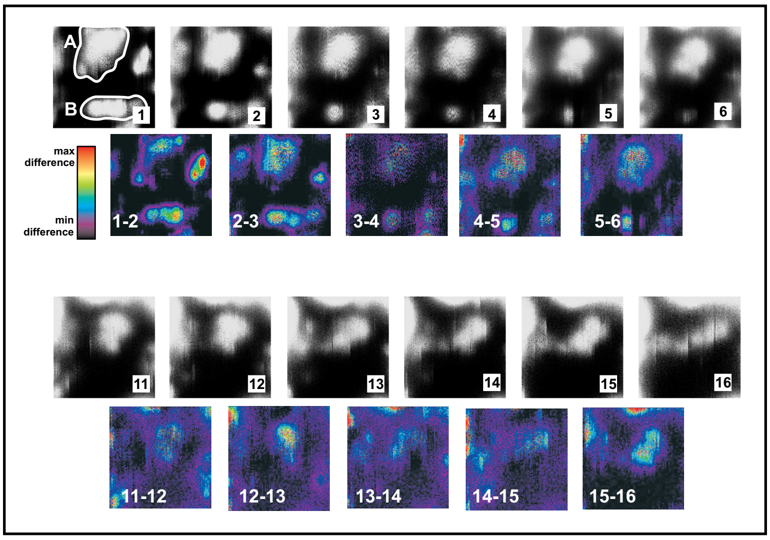

Figure 5.9: Image subtraction method. The total signal of the first and last six images of the sequence are shown in gray. The difference between two successive images are shown as the rainbow colored images (red is a large difference in signal and black is a small difference).

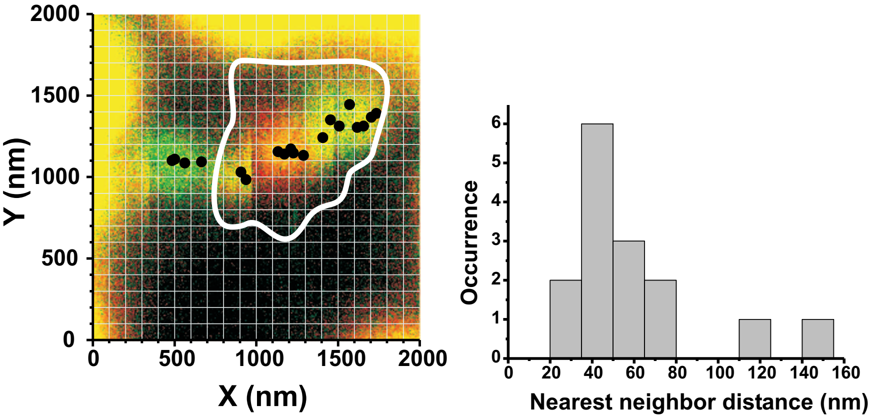

(a) (b)

Figure 5.10: (a) Spatial reconstruction of domain A, taking into account images 16 to 24. The black dots, indicating the position of individual molecules, are super-imposed on image image 15. (b) Nearest neighbor distance distribution of the Cy5 molecules in domain A (a).

time. Going backwards in time from frame 24 towards frame 1, we can localize and count the number of individual fluorophores in each frame, making use of typical single molecule signatures. The number of fluorophores obtained in this way is plotted as function of the frame number in Figure 5.8 as red symbols. Unfortunately, this method is not applicable if the intensity becomes too high and molecules are too closely packed. Therefore, the domains can only partially be reconstructed within a limited number of frames, i.e. from frame 24 up to to frame 16 for domain A and from frame 11 to frame 7 for domain B. To overcome this limitation, the total intensities of successive images are subtracted. The resulting difference images clearly exhibit bleached molecules, located at different positions, as shown in Figure 5.9. Using the difference images, single molecules could be identified in domain A from frame 16 down to 11 and in domain B from frame 6 to 3 (green symbols in figure 5.8). However, this method also can not be extended to frame 1, because if the shot noise in an area becomes larger than the single molecule intensity, difference images of that area can not reveal a single bleached molecule. This is apparent from the first five difference images in Figure 5.9, where the shot noise in domain A results in a homogeneous intensity difference.

Simultaneously with the identification of a single molecule, its position can be determined by fitting the intensity profile to a 2D Gaussian. In this way, the stoichiometry as well as the spatial organization of a molecular domain can be determined. The signal to background ratio of a single Cy5 molecule is only 2.4 in these images. Therefore, the localization accuracy of single molecules in Figure 5.7 is $\sim 6\,\mathrm{nm}$, using a similar procedure as in Chapter 2. The positions of molecules, identified from frame 24 down to frame 16 are plotted on top of image 15 in Figure 5.10(a). Having pinpointed the positions of the Cy5 molecules within a domain, we are now able to reconstruct a nearest neighbor distance (*nnd*) distribution of fluorophores based on real positions. The *nnd* distribution of all molecules within domain A in frame 16 is shown in Figure 5.10(b), showing a typical *nnd* of 45 nm.

5.3 Discussion

In this chapter, photobleaching has been used to unravel molecular systems of different densities. Cy5-labeled antibodies can be regarded as low density systems. The labeling efficiency of individual antibodies has been directly determined by counting the number of discrete photobleaching steps from a fluorescence time trajectory, as shown in Figure 5.2(b). Relating the number of bleaching steps to the intensity count rate of a fluorescent spot, the average single molecule intensity has been determined, as shown in Figure 5.3(a). Using the average single molecule intensity, the intensity count rate from isolated antibodies was converted to the number of attached Cy5-molecules, being 3.2 Cy5 molecules per antibody. The measured labeling efficiency corresponds well to the specifications provided by the manufacturer, i.e. 2 - 4 Cy5 dyes per antibody. In Chapter 3, the same type of antibodies have been used to fluorescently label DC-SIGN proteins. The intensity distribution of all fluorescence spots, as shown in Figure 3.4(a), has a peak value of 3.5 Cy5 molecules, which corresponds to the labeling efficiency of the antibodies as measured here. Therefore, the main peak in the intensity distribution of Figure 3.4(a) can be attributed to the labeling efficiency and thus to individual DC-SIGN proteins, assuming one labeled antibody per protein.

In contrast to the labeled antibodies, fluorescence time traces of densely packed systems, such as the molecular domains shown in Figure 5.4(a), merely resemble the bleaching curves of a bulk sample. This is evident from the time trace in Figure 5.4(b), where in the first 20 seconds the intensity decays exponentially without showing discrete steps, due to a large contribution of shot noise. The characteristic bleach time of the time trace is 16.5 s, as determined by fitting the time trace to an exponential decaying function. After $t = 21$ s the shot noise has become low enough to distinguish discrete steps in the time trace. Schmidt et al. defined this limit for counting the number of colocalized fluorescent molecules as 'stoichiometric resolution' [100, 215]. Each step in Figure 5.4(b) bridges an intensity difference of ~ 2 kcnts/s. After background subtraction, the last remaining fluorescent molecule has an intensity of $i_1 = 2.1$ kcnts/s with a standard deviation $\sigma_1 = 0.7$ kcnts/s. For n fluorescent molecules in close proximity, the measured intensity becomes $n \cdot i_1 \pm \sqrt{n} \cdot \sigma_1$. Obviously, the bleaching step of a single molecule can be counted as long as the error is smaller than the single molecule signal. Therefore, the maximum number of molecules that can be counted (n_{max}), i.e. stoichiometric resolution, is given by $\sqrt{n_{max}} \cdot \sigma_1 < i_1$, i.e. $n_{max} < 9$ in Figure 5.4(b). Indeed, eight discrete photobleaching steps are clearly observed from $t = 21$ s to $t = 120$ s, bridging a total difference signal of $i_n = 16.7$ kcnts/s. The large step of ~ 5 kcnts/s at $t = 19$ s is likely to be due to simultaneous bleaching of 2 or 3 fluorophores. Taking into account the single molecule count rate of

2.1 kcnts/s, the intensity at $t = 0\,\mathrm{s}$ corresponds to ~ 40 Cy5 molecules.

Both the stoichiometry and the spatial organization within densely packed molecular domains have been measured by sequential imaging of the same area, as shown in Figure 5.7. Starting with the final image in the sequence, working backwards in time towards the first image, individual molecules could be counted as well as localized in the intensity images. This method is much more accurate in order to determine the stoichiometry of a sample than using intensity integration, because all fluorescent molecules are individually counted, without using average intensity values. However, this type of analysis can be performed as long as the single molecule character dominates over the bulk behavior, i.e., when the number of molecules present in the illumination spot is such that their unique properties such as orientation, discrete emission and spatial distribution can be distinguished individually. Therefore, the stoichiometry could not be determined in the first few frames of Figure 5.7. To extend the analysis to a larger number of frames, difference images of successive frames have been used. The applicability of the difference images for stoichiometry is limited by shot noise within the illumination spot, i.e. the stoichiometric resolution. In total, about 35 molecules could be counted individually within both domain A and B, i.e. the total number of non-bleached molecules in frame 11 and frame 3, respectively. As domain A has an area of $0.67\,\mu\mathrm{m}^2$ and domain B an area of $0.46\,\mu\mathrm{m}^2$, the molecular densities of the domains in frame 11 and frame 3 are 52 and 76 molecules/$\mu\mathrm{m}^2$, respectively. By taking advantage of the integrated intensity analysis shown in Figure 5.8, one can derive an intensity ratio between frame 1 and frame 11 of 3.6 for domain A. Assuming that the spatial organization of frame 11 is similar to the organization in frame 1, the number of fluorophores in frame one is about $3.6 \times 16 = 112$ molecules. Accordingly, the intensity ratio between frame 1 and frame 3 for domain B is 2.2, giving the number of fluorophores in frame one to be $2.2 \times 34 = 75$ molecules. Because of blinking and bleaching of molecules, the intensity integration of domain A and B, as depicted in Figure 5.8 by black symbols, results generally in lower molecular densities than in case molecules are counted one by one. Figure 5.8 shows the validity of the intensity integration method (black symbols) in comparison to the sequential imaging method (red and green symbols). For these samples, i.e. labeled DC-SIGN on imDCs, the deviation of the intensity integration method and pure stoichiometry can become more than 20% for domains containing more than 40 fluorescent molecules as is the case for about 20% of all investigated fluorescent spots in Chapter 3, see Figure 3.4(a).

A unique advantage of sequential imaging is the possibility to directly measure the positions of individual fluorophores while counting them. In this way, direct information on the intra-domain positions of fluorophores is obtained, allowing spatial reconstruction of a densely packed domain. Figure 5.10 shows the positions of 15 fluorophores within domain A for frame 16, with a localization accuracy of 6 nm. We can now directly measure the nearest neighbor distances (*nnd*) between fluorophores and build up a *nnd* distribution without making any assumptions on the distribution pattern. The *nnd* distribution of the molecules in domain A of Figure 5.10 is shown in Figure 5.10(b). The distribution peaks at $nnd \approx 45$ nm, which is less than expected for a random distribution at this fluorophore density, i.e. ~ 105 nm. Thus, the distribution pattern of the fluorophores is not random, which is probably related to the fact that the fluorophores are attached to antibodies and therefore distributed as small bunches. Still, the real positions of the proteins are unknown, i.e. their distribution might be random. Therefore, full exploitation of this method can only be achieved using autofluorescent proteins.

5.4 Conclusions

Photobleaching is a useful phenomenon to be exploited for stoichiometric analysis of fluorescence images. By counting the number of photobleaching steps in a fluorescence time trajectory the number of fluorophores within the illumination spot can be determined. In this work, fluorescence time trajectories of individual Cy5-labeled antibodies have been used to determine the labeling efficiency distribution with on average 3.2 Cy5 per antibody. The emitted count rate of a single fluorophore can also be measured on fluorescence time trajectories of densely packed areas. Quantification of the single molecule intensity allows normalization of the overall image intensity and estimate the number of fluorophores per area. If the fluorophores are used as protein labels, the image intensity in combination with the labeling efficiency allows to estimate the number of proteins. A particularly useful way to reveal the spatial organization of fluorophores using photobleaching is by sequential imaging of the same sample area. By subtracting successive images, the number and location of bleached molecules can be measured. In this way, the high localization accuracy (~ 6 nm in Figure 5.7) obtained by NSOM can reveal the spatial organization of the fluorophores within a domain and allow molecular reconstruction of domains. Although this method provides more knowledge on the accurate positions of closely packed molecules, it is still limited by shot noise and therefore it can not be extended to highly packed systems.

Chapter 6

Organization of Interleukin receptors on T cells

This chapter focuses on the nano-scale organization of two types of Interleukin receptor proteins (IL-2Rα and IL-15Rα) expressed on the membrane of T cells. These proteins are essential for cell signaling, playing both similar and contrasting roles in cell functioning. Combined confocal/NSOM imaging on T cells has shown the existence of nano-domains of IL-2Rα and IL-15Rα $\sim$400 nm in size. The single molecule sensitivity of our microscope allows quantitative investigation of the molecular packing density of the domains, giving direct insight into inter-molecular distances in the nanometer range. The relative spatial distribution of the two different domains has been investigated by dual color near-field excitation and detection experiments, revealing co-localization of both IL-2Rα and IL-15Rα domains. Furthermore, our experiments provide direct information about the fractions of both IL-2Rα and IL-15Rα residing outside the domain regions.

6.1 Introduction

This chapter takes us to a later stage in the immune response, i.e. the initiation of the adaptive immune system in which T cells are activated by antigen presenting cells, as briefly described in Chapter 1. The growth, differentiation and proliferation of activated T cells is regulated by cytokines. These small proteins bind with high affinity to certain cell surface receptors. Upon binding, cytokines induce a series of intracellular signals that lead to specific cell responses, e.g. proliferation [10, 216]. Amongst the various cytokine receptors in our body, receptors IL-2R and IL-15R are closely related in structure and function and found on activated T cells [216–218]. Remarkably, cytokine binding to these receptors sometimes induces opposite cell behavior, an issue that is not well understood at present [216–219]. The reasons for this dissimilar behavior might be related to the expression [218] and/or expression pattern of these molecules on the membrane. Therefore, in this research we have studied the absolute and relative spatial organization of IL-2R and IL-15R, using near-field optical microscopy with single molecule sensitivity.

6.2 Interleukin receptors IL-2R and IL-15R

6.2.1 T cell activation

As explained in Chapter 1, after the DC has taken up antigens at the site of infection, the cell develops into a mature DC. The matured DC expresses the ingested foreign protein fragments or antigens at its surface by a protein complex structure, i.e. the major histocompatibility complex (MHC). When the DC encounters a naïve cytotoxic or helper T cell that recognizes the foreign protein fragments, it can activate the T cell to differentiate and proliferate into effector cells. These effector cells are capable of fighting the infection either by killing infected cells (cytotoxic T cell) or stimulating other immune cells (helper T cell). Activation is achieved if a mature DC delivers two independent signals to the naïve T cell, as shown in Figure 6.1 [10].

6.2.2 The role of IL-2R after the activation of T cells

After activation, the T cell starts to produce and secrete a cytokine, interleukin 2 (IL-2), also referred to in the literature as CD25 or Tac [10]. In the early stage of activation, IL-2 controls the multiplication of the T cells by stimulating cell growth [220]. This ensures continuation of the immune response. The receptor for

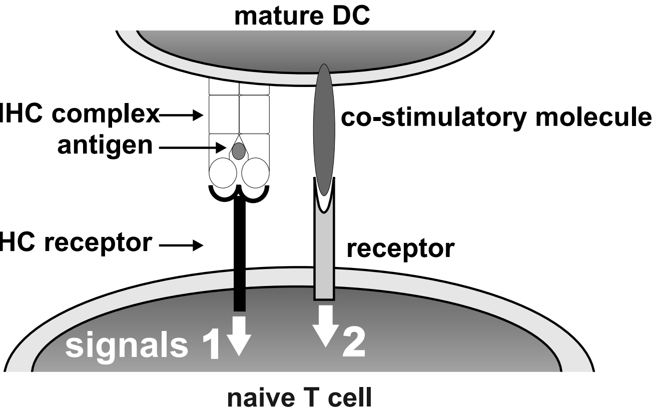

Figure 6.1: Dendritic cell activates T cell. The activation requires two independent signals delivered from one mature DC. These signals are generated upon binding. Signal 1 is delivered when the MHC-complex, that carries the antigens, binds to the MHC-counter receptor. Signal 2 is a co-stimulatory signal, provided by specific co-stimulatory proteins, that is only effective if it is delivered by the same cell [10].

IL-2 (IL-2R) exists in three forms that differ in binding affinity to IL-2 [216, 218, 219]. The low affinity form ($K_d = 10^{-8}$M) is a monomer of the α subunit IL-2Rα not involved in signal transduction. The intermediate affinity ($K_d = 10^{-9}$M) form consists of a β - γ_c subunit heterodimer, while the high affinity ($K_d = 10^{-11}$M) form is a heterotrimer, consisting of all three α, β and γ subunits. While IL-2Rβ and IL-2Rγ_c are produced by both resting and activated T cells, only activated T cells synthesize a large amount of IL-2Rα [136].

Both the intermediate and high affinity forms of the receptor are involved in cell signaling, as depicted in Figure 6.2. When IL-2 binds to its receptor, a whole cascade of secondary binding and signaling events is induced, leading to an up and down regulation of genes which are related to T cell proliferation and survival [219]. Because of the autocrine nature of this mechanism, a T cell can continue to proliferate after it has detached from the antigen presenting cell and also stimulate other nearby activated T cells.

FRET measurements on the different subunits of the IL-2R trimer have been performed on T cells, revealing that the three subunits are in close proximity [199]. Pre-assembly of α, β and γ_c in clusters has been observed even in absence of IL-2. However, the presence of IL-2 modulates the relative distances between the subunits, resulting in a compact form of the high affinity form of IL-2R. Oligomerization of the β and γ_c subunits increases cell signaling ability and was

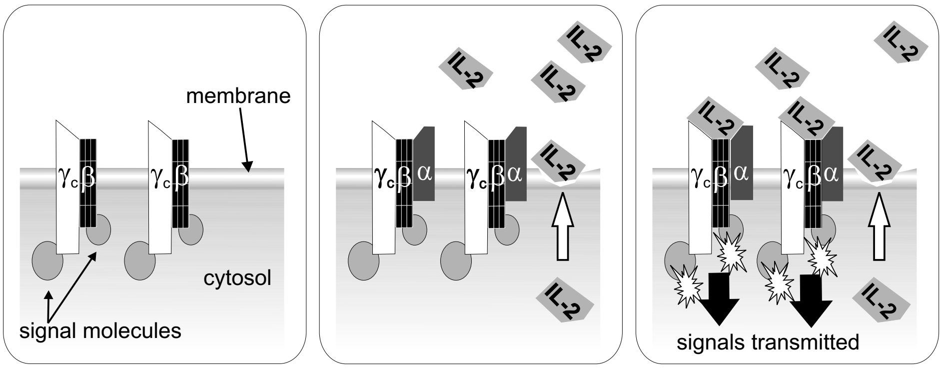

(a) (b) (c)

Figure 6.2: From naïve to activated T cell. (a) The naïve T cell expresses an intermediate affinity form receptor for IL-2, a heterodimer consisting mainly of IL-2Rβ and IL-2Rγ_c. The intracellular part of these molecules are linked to signaling molecules within the cell. (b) The activated T cell expresses the high affinity receptor for IL-2, consisting of IL-2Rα, β and γ_c. Simultaneously, the cell produces and secretes cytokine IL-2. (c) The secreted IL-2 molecules bind to the high affinity IL-2R complex. Upon binding a signaling cascade is triggered, which results in the differentiation and proliferation of T cells.

only observed in presence of IL-2Rα [221]. Therefore, it has been hypothesized that IL-2Rα is not only critical for the formation of a high affinity receptor, but also for the signaling ability of the whole receptor complex [221].

6.2.3 IL-2R and IL-15R: two competing receptors

Receptor structure and function

The IL-2Rα subunit is unique to the high affinity receptor IL-2R, whereas the other two subunits, β and γ_c are shared with another cytokine receptor, IL-15R [216, 218, 219]. Similar to the receptor for IL-2, there are three forms of the IL-15 receptor; a low affinity form ($K_d = 10^{-9}$M) consisting of the same β and γ_c heterodimer as for IL-2 and a high affinity form ($K_d = 10^{-11}$M) consisting of all three subunits IL-15Rα, β and γ_c, denoted as IL-15R [216]. Interestingly the IL-15Rα monomer has also a high affinity for IL-15 ($K_d = 10^{-11}$M) [216]. Although the α subunits are essential for proper signaling capabilities of the IL-2R and IL-15R receptors [218, 219, 221], it is not known yet what their specific roles are. While it is improbable that IL-2R independently generates signals due to its short cytoplasmic tail [219, 221], it is unclear whether IL-15Rα is capable of signaling.

Because IL-2Rα and IL-15Rα are structurally related [222], it is not surprising that binding of IL-2 to IL-2R and IL-15 to IL-15R leads to similar biological activities. Both cytokines stimulate T cell proliferation and induction of specific effector cells. However, IL-2 and IL-15 also facilitate cellular processes that work exactly opposed to each other [217]. For example, IL-2 plays a key role in activated-induced cell death of T cells, while IL-15 inhibits this process to extend the survival of T cells. In addition, IL-15 stimulates the division and survival of CD8 - expressing memory T cells while IL-2 inhibits their proliferation [216, 223]. It remains to be answered which mechanism accounts for the (dis)similarities of the signals. Due to their signaling capabilities, both IL-2R and IL-15R have been recognized as attractive candidates for immunotherapy. For example, humanized antibodies directed against the IL-2Rα subunit cause T cell inactivation to prevent acute rejection of transplanted kidneys [224]. In conclusion, there is an important relation between both structure and function of IL-2R and IL-15R, in which the respective α subunits seem to have a key function to distinguish the cellular responses upon Il-2 and IL-15 binding.

Spatial organization of IL-2Rα and IL-15Rα

In recent experiments by Vereb et al., aimed at elucidating the functional properties of IL-2Rα, immunogold labeling and electron microscopy showed that IL-2Rα clusters on the membrane of human leukemia T cells. Confocal microscopy studies confirmed the existence of these domains, having a diameter of ~ 500 - 800 nm [200]. Moreover, the domains showed co-localization with fluorescently labeled lipid raft markers. Damjanovich and coworkers suggested that the concentration of α subunits within the vicinity of many β and γ_c molecules in rafts creates platforms with high affinity to IL-2 and strong signaling capability [201]. Interestingly, in the same study FRET experiments on cell-to-cell basis using flow cytometry, showed a modest co-localization of IL-2Rα with the Transferrin receptor (TrfR), which is known to be excluded from glycosphingolipid-enriched membrane domains [201]. Using endocytosis, this receptor delivers TrfR - bound iron to the intracellular endosomal compartment. When the iron cargo is released, the receptor-TrfR complex is brought back to the membrane where the TrfR molecule is released. In this way both molecule and receptor are recycled [10]. Matko et al. suggested that the association of IL-2Rα with these TrfR domains may provide an efficient endocytosis-recycling pathway for the excess of α subunits not involved in signal transduction of these cells [201]. However, clear proof for the existence of an excess of α-subunits is still lacking.

In contrast to IL-2Rα, much less is known about the spatial organization of IL-15Rα and its possible relation to IL-2Rα. As both IL-2Rα and IL-15Rα

play a key role in the signaling function of cells, their expression pattern on the membrane might be related to their specific role in signaling. Therefore, we have studied the spatial organization of both Il-2Rα and IL-15Rα on the membrane of activated T cells.

6.3 Materials and methods

Cell culture and preparation

The experiments have been performed on Kit225 FT7.10, a human cell line of T leukemia/lymphoma origin that constitutively expresses all subunits of the IL-2R and IL-15R complexes [225]. The cell line was cultured in RPMI-1640 medium (5 % CO_2) supplemented with 10 % fetal calf serum and 20 units/ml of the antibiotics penicillin and streptomycin. To maintain cell growth and division, 20 units/ml human recombinant IL-2 were added every 48 hours. Therefore, the T cells are considered activated. The culture medium also contained 800 μg/ml G418 (Genectin) to suppress the growth of non-transfected wild type cells.

Freshly harvested cells were washed twice in ice-cold PBS (pH 7.4). The cell pellet was suspended in 50 μl PBS (0.5 - 1 $\times 10^7$ cells/ml) and labeled by incubation with 5 - 10 μg of fluorescently conjugated monoclonal antibodies (mAbs), for 45 minutes on ice. The dye to protein ratio was determined with a spectrophotometer. The ratios were $\sim$3.9 for Cy5-7A4-24, $\sim$2.8 for Cy5-7G7, $\sim$2.9 for Alexa488-7A4-24 and $\sim$1.0 for Alexa488-7G7. The IL-2Rα subunit was targeted with 7G7/B6 mAbs. IL-15Rα was defined with 7A4-24 mAbs. The fluorescently conjugated mAbs were added as a combination of either Cy5-7G7 and Alexa 488-7A4-24 or Cy5-7A4-24 and Alexa488-7G7. The excess of mAbs over the available binding sites was at least 30-fold during the incubation. To avoid possible aggregation of the antibodies, they were air-fuged at 9×10^4 rpm, for 30 min before labeling. The labeled cells were washed with excess cold PBS, then put onto a glass coverslip and fixed with 4% paraformaldehyde for 60 min on ice, and dehydrated in an ethanol series.

Single and dual color near-field fluorescence microscopy

Single color fluorescence experiments of Cy5-labeled proteins on T cells were performed in near-field mode using 647 nm wavelength excitation (Kr^+ line and 647 FS02-25 excitation filter, Åndover Corp.), at an excitation intensity of 200 W/cm^2. Fluorescence emission of Cy5 was collected by a 1.3 NA objective, discriminated from the excitation wavelength using a long pass filter (AELP665), separated in two orthogonal polarization channels and detected with two avalanche photodiodes.

For dual color experiments two types of samples were used; one type with IL-2Rα-Cy5 and IL-15Rα-Alexa 488 as protein-dye couples and a second type with the labeling vice versa, i.e. IL-2Rα-Alexa488 and IL-15Rα-Cy5. The 488 nm and 647 nm excitation wavelengths were filtered using 488 FS02-25 and 647 FS02-25 excitation filters, respectively (Åndover Corp.). For simultaneous excitation at 488 nm and 647 nm in confocal mode, a dual band dichroic mirror (XF2041, Omega Optical Inc.) was placed in the excitation path. Polarization and excitation intensity were adjusted independently before overlapping the two beams to yield circularly polarized light and an excitation intensity of 200 W/cm^2. For dual wavelength near-field excitation, both wavelengths were coupled simultaneously in the Al-coated fiber probe. Again, polarization and excitation intensity were adjusted independently to yield circularly polarized light and an excitation intensity of 200 W/cm^2, as measured in the far-field. Fluorescence emission was collected with the 1.3 NA objective and then spectrally separated using a 565DRLP dichroic mirror (XF2081 Omega Optical Inc.). The dichroic mirror was placed in the light tight box (see Chapter 2), which also contained additional fluorescence filters, i.e. a long pass (510LP, Omega Optical) and a band pass filter (D530-45, Chroma) in the Alexa488 channel and a long pass filter (665AELP, Omega Optical) in the Cy5 channel.

Cells were first screened for their overall structure and height, using the bright field mode of the microscope. An area of typically $20 \times 20\,\mu m^2$ (256×256 pixels) from the selected cell was imaged in confocal mode, at a scan speed of typically $5\,\mu$m/s, with either single or dual wavelength excitation. In total, 7 cells from each of the two different sample sets have been investigated by performing 30 near-field measurements with dual wavelength excitation. Near-field images of typically $5 \times 5\,\mu m^2$ (256×256 pixels) at a scan speed of $2\,\mu$m/s were obtained. The same NSOM probe, with an aperture diameter of ~ 90 nm was used in all experiments.

6.4 Results

6.4.1 High resolution imaging of IL-2Rα and IL-15Rα

In the first set of experiments, the nano-scale organization of IL-2Rα and IL-15Rα was investigated independently, i.e., in different cells, using Cy5 as the main label. Cy5 was chosen because of its red shifted emission and good photophysical properties, reducing the contribution of cell autofluorescence, and therefore facilitating quantitative analysis of the data. Figure 6.3 shows a complete measurement sequence starting with a bright-field image of two fixed T cells and finishing with a high resolution NSOM image of Cy5-labeled IL-15Rα proteins on the cell membrane. From the confocal image in Figure 6.3(b) it is apparent that Il-15Rα is spread over the whole cell.

Figure 6.3(c) and 6.3(d) show the near-field fluorescence and topography images respectively of the white boxed area in the confocal image. The high spatial resolution of NSOM reveals more fluorescence contrast than confocal microscopy, e.g. single molecule fluorescence spots are visible on the cell surface (indicated in Figure 6.3(c)). Still, large fluorescent patches are visible, a first indication for the assembly of IL-15Rα molecules in clusters. Similar IL-15Rα patches were observed for all cells investigated. A unique advantage of NSOM is the correlated topography which allows the identification of regions on the membrane containing proteins. For instance, the left side of Figure 6.3(d) shows the presence of the cell although hardly any fluorescence is detected in this region (Figure 6.3(c)). This observation also confirms that fluctuations in the optical signal are independent of the shear force signal. Therefore, the fluorescence patches are purely due to the local presence of an abundant number of dyes and thus IL-15Rα proteins.

Figure 6.4 is a combined image of four near-field measurements, showing Cy5 labeled IL-2Rα proteins on a T cell. Interestingly, the cell exhibits two types of protein coverage, i.e., clustered regions of IL-2Rα shown as bright fluorescent patches as well as low-coverage areas containing single molecule fluorescent spots with a size determined by the near-field aperture, indicating the presence of only a few proteins. The recorded topography images of the same area show that the middle of the cell reaches a height of 1.2 μm (data not shown). Whereas the low intensity spots are circular, the high intensity patches for both IL-15Rα and IL-2Rα have irregular forms. Most near-field images show a preferential presence of IL-2Rα and IL-15Rα domains at the cell edges towards the glass substrate. Confocal sectioning images of the cells showed a similar trend.

To obtain in-depth information about the (dis-)similarities of IL-15Rα and IL-2Rα domains, we performed a detailed quantitative analysis of the domain properties for both types of proteins.

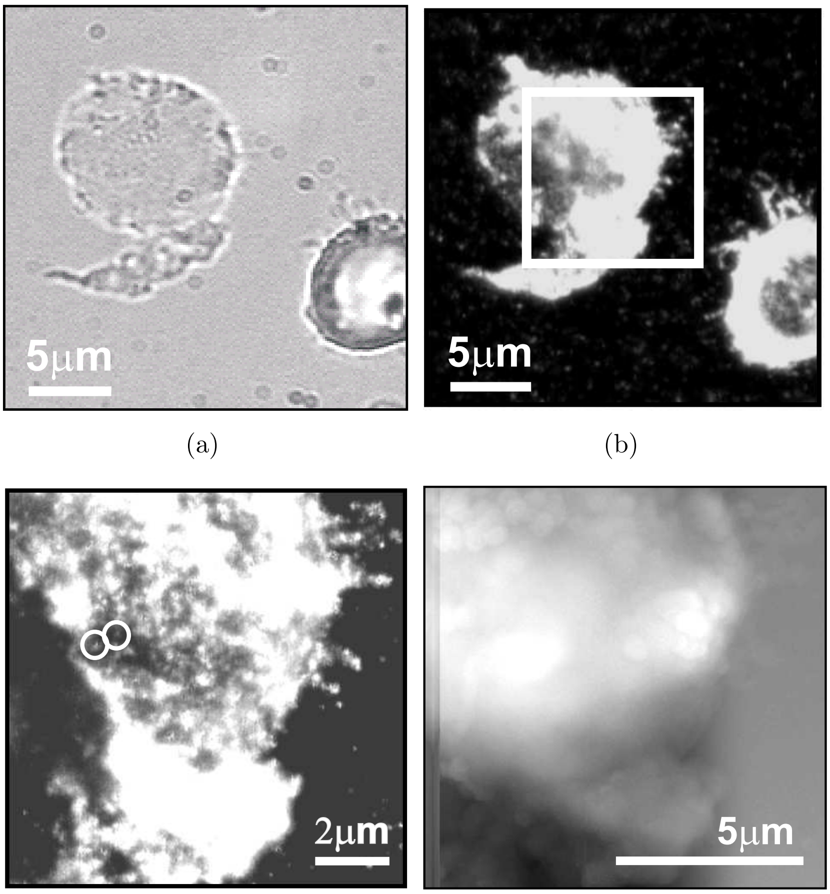

(a)

(b)

(c)

(d)

Figure 6.3: (a) Bright-field image of fixed T cells, immuno-labeled with Cy5-conjugated antibodies against IL-15Rα. (b) Confocal fluorescence image of the same sample area as in (a). The focal plane was positioned at the glass surface. (c) NSOM image of the boxed area in (b), showing single molecules surrounded by white circles. (d) Simultaneously obtained shear force image clearly shows the cell membrane structure, reaching a maximum height of $\sim 1\,\mu$m.

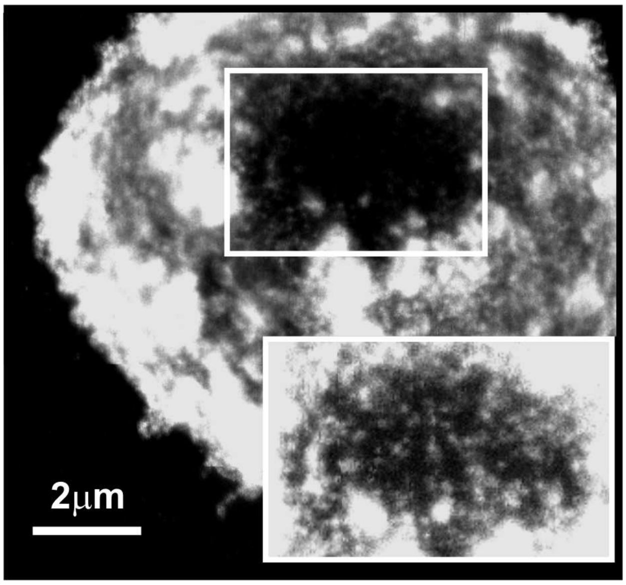

Figure 6.4: Four near-field fluorescence measurements of Cy5-IL-2Rα on an activated T cell. A compromise in image contrast accounts for the effect that the low intensity spots in the middle of the cell are not clearly visible. The inset shows the white boxed area with different image contrast, revealing the presence of single molecules.

6.4.2 IL-15Rα and IL-2Rα domain properties

IL-15Rα and IL-2Rα domain content

All fluorescent spots in the near-field images of IL-15Rα and IL-2Rα were analyzed in terms of intensity, size, position on the membrane and relative position with respect to neighboring spots, following a procedure similar to that in Chapter 3. Some fluorescent spots were attributed to single molecules as they showed the characteristics of single molecule emission, i.e. discrete time dependent emission, photobleaching and a unique emission dipole moment. The distribution in Figure 6.5 contains the intensity of single molecule fluorescence spots as extracted from the images. The typical Cy5 count rate was ~ 4 kcnts/s at an excitation intensity of $200\,\mathrm{W/cm^2}$. This number was used to relate the fluorescence intensity of a spot to the number of Cy5 molecules within the area occupied by the spot. For each spot, the total number of emitted counts was background subtracted and normalized with respect to an excitation intensity of $200\,\mathrm{W/cm^2}$. The intensity distributions for IL-2Rα and IL-15Rα are shown in Figure 6.6(a) and 6.6(b).

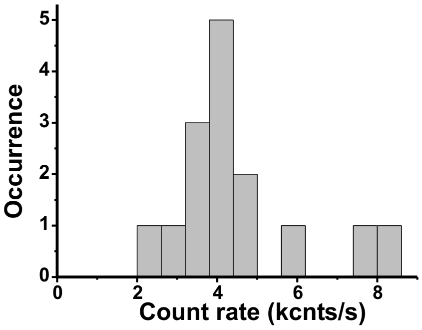

Figure 6.5: Intensity distribution containing fluorescent spots that exhibited single molecular fluorescence behavior such as blinking and bleaching. The distribution peaks at a count rate of ~ 4 kcnts/s at an excitation intensity of 200 W/cm^2.

Interestingly, the intensity distribution of Cy5-labeled IL-2Rα shows two contributions: an abundant low intensity part of the distribution peaking at ~ 1.5 Cy5 molecules, and a second high intensity distribution peaking at ~ 130 Cy5 molecules per spot. These distinct distributions were already apparent from Figure 6.4, showing patches of high intensity as well as low intensity spots. The peak value of ~ 1.5 Cy5 is lower than the antibody labeling efficiency of ~ 3 Cy5 / IL-2Rα estimated spectrophotometrically, which might be due to the sample preparation. Under the reasonable assumption that no unspecific Cy5 molecules are present on the cell surface and a one to one antibody to protein ratio, we attribute the peak of the lower intensity distribution to individual IL-2Rα proteins with a typical labeling efficiency of ~ 1.5 Cy5 / IL-2Rα protein. From an analysis of seven different near-field images, we found that about $1.4 \pm 1.1\%$ for IL-2Rα subunits are distributed spatially as individual entities.

Figure 6.6(b) shows the intensity distribution of Cy5-labeled Il-15Rα proteins. Two closely spaced populations are observed. The peak values of the two subdistributions are: ~ 3 and ~ 15 Cy5 molecules. Using the same assumptions as for IL-2Rα, we attributed the peak value of the lower intensity sub-distribution to the labeling efficiency. For the IL-15Rα subunit $29 \pm 14\%$ appear to be distributed as singles on the surface of the T cell. In absolute numbers there are ~ 15 IL-2Rα/μm^2 and ~ 5 IL-15Rα/μm^2. Furthermore, the peak values of the two high intensity distributions indicate that IL-2Rα and IL-15Rα domains consist of typically ~ 90 proteins and ~ 5 proteins, respectively.

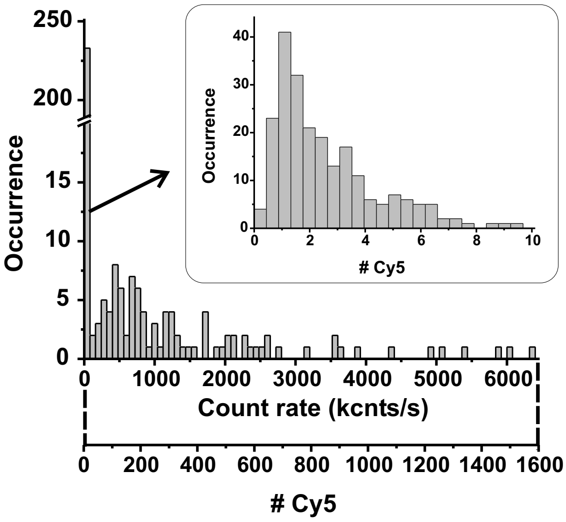

(a)

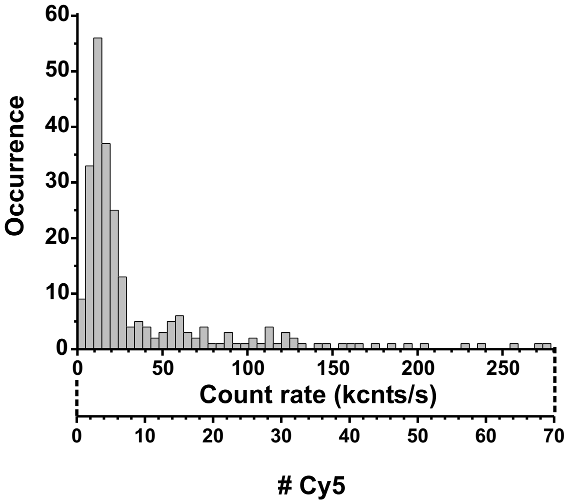

(b)

Figure 6.6: Intensity distribution in terms of fluorescence count rate at an excitation power of 200 W/cm^2 and number of Cy5 molecules of (a) Cy5-IL-2Rα and (b) Cy5-IL-15Rα. In (a) the low intensity part of the distribution is more accurately shown in the inset in terms of number of Cy5 molecules.

IL-2Rα and IL-15Rα domain sizes

To find out whether IL-2Rα and IL-15Rα domains differ in size, we next focused on all spots with intensities higher than twice the peak value of the lower sub-distributions, i.e. $\sim$3 Cy5 molecules for IL-2Rα and $\sim$6 Cy5 molecules for IL-15Rα. The domain size was defined as the area within an intensity contour at twice the background intensity. Figure 6.7 shows the distribution of the occupied areas and sizes of IL-2Rα and IL-15Rα domains. The typical area of the IL-2Rα domains is $0.15\,\mu m^2$, corresponding to a diameter of $\sim$450 nm. IL-15Rα domain areas are typically $0.10\,\mu m^2$,i.e. $\sim$360 nm in diameter. Taking into account the probe aperture response, $\sim$90 nm, the typically observed domain sizes in Figure 6.7 deviate only about 2 - 3% from the real domain size (see section 3.4.2). This deviation is negligible and therefore the domain sizes presented in Figure 6.7 were not corrected with the probe response. It is interesting to note that the domain sizes of IL-2Rα and IL-15Rα are rather similar, while the intensity analysis showed that the number of molecules of both types of domains differ by more than one order of magnitude.

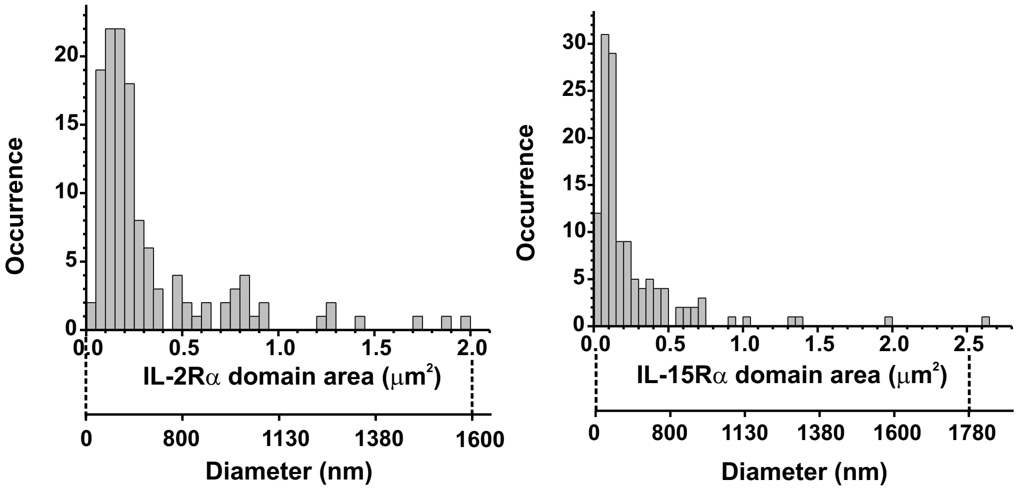

(a) (b)

Figure 6.7: Domain area/size distributions for domains of IL-2Rα (a) and IL-15Rα (b). For convenience both the occupied domain area (μm^2) and the corresponding domain diameter are indicated.

Molecular density of IL-2Rα and Il-15Rα domains

In Figure 6.8(a) the correlation graphs of domain content and area are plotted for both IL-2Rα and IL-15Rα domains. Both types of domains show a linear relation, implying that the domains have a constant molecular packing density, regardless of the specific domain size. The molecular density in IL-2Rα domains is 1350 IL-2Rα/μm^2, i.e. on average one IL-2Rα molecule is present in an area of $27 \times 27\,\mathrm{nm}^2$. In contrast, IL-15R$\alpha$ domains have a molecular density of 120 IL-15Rα/μm^2, i.e. one IL-15Rα per area of $92 \times 92\,\mathrm{nm}^2$. Thus, IL-2R$\alpha$ domains are approximately ten times denser than IL-15Rα domains.

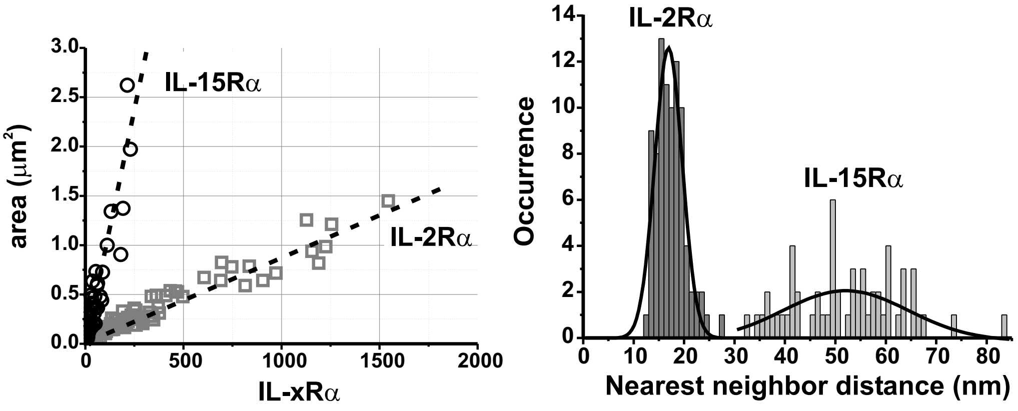

(a) (b)

Figure 6.8: (a) Correlation between domain area and number of receptors for IL-2Rα (squares) and IL-15Rα domains (dots). (b) Distribution of the calculated nearest neighbor distances within IL-2Rα and IL-15Rα domains.

The intermolecular separation was calculated for each domain. Assuming a random distribution of α-subunits in each domain, the distances are collected in the distribution of Figure 6.8(b). Clearly two distinct distributions for molecular distances within IL-2Rα and IL-15Rα domains are obtained. The peaks of the distributions correspond roughly to the $0.5/\sqrt{a}$ where a is the slope derived from Figure 6.8(a). Therefore, it follows that molecules are $\sim 14\,\mathrm{nm}$ separated within the IL-2Rα domains and $\sim 50\,\mathrm{nm}$ within the IL-15Rα domains.

6.4.3 Co-localization of IL-2Rα and IL-15Rα domains

The previous findings, in particular the similarity in domain size and the constant packing density of both types of domains, strongly suggest that IL-2Rα and IL-15Rα are related in terms of their organization on the membrane. We have investigated the relative location of IL-2Rα and IL-15Rα domains on the T cell membrane, using dual color excitation and detection, where IL-2Rα and IL-15Rα were labeled with different fluorophores. Figure 6.9 shows as example the result of such a measurement, in which IL-15Rα was labeled with Cy5 and IL-2Rα with Alexa488. A first inspection of the dual color images already shows that the IL-2Rα and IL-15Rα domains do co-localize.

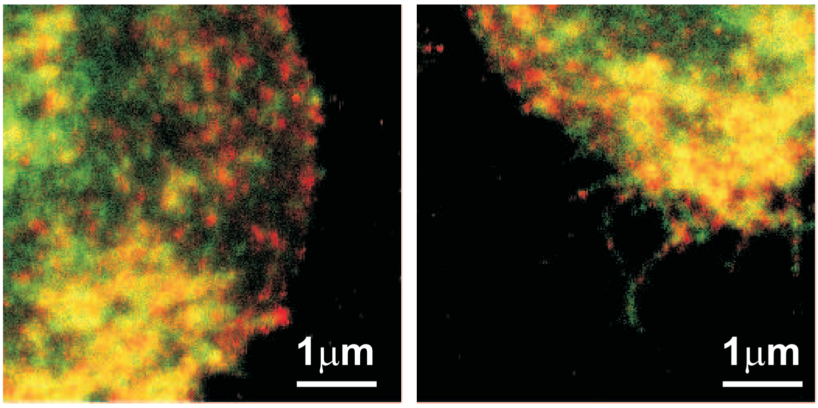

Figure 6.9: Co-localization of Alexa488 - IL-2Rα and Cy5 - IL-15Rα. Note that here the pseudo-color scale refers to spectral contrast, i.e. Alexa488 fluorescence is shown in green and Cy5 in red. The yellow color indicates co-localization of Alexa488 and Cy5 signal. Images are $5 \times 5\,\mu\text{m}^2$ (256×256 pixels), scanned at $2\,\mu$m/s. The cell heights vary from tens of nanometers in the dendrite regions to $1.5\,\mu$m towards the center of cell body.

To describe the extent of spatial overlap of IL-2Rα and IL-15Rα domains, we performed cross-correlation analysis on simultaneously obtained Cy5 and Alexa488 images. The degree of correlation between two images a and b can be calculated pixel by pixel using the cross-correlation coefficient C or Pearson's Correlation, defined as:

$$C = \frac{\sum_i \sum_j (a_{i,j} - < a >)(b_{i,j} - < b >)}{\sqrt{\sum_i \sum_j (a_{i,j} - < a >)^2 \sum_i \sum_j (b_{i,j} - < b >)^2}} \tag{6.1}$$

where $a_{i,j}$ and $b_{i,j}$ are the fluorescence intensities at pixel coordinates (i,j) for the two images a and b. Parameters $< a >$ and $< b >$ are the the average intensity values for the total images a and b, respectively. The equation is sensitive for shape similarities between the images, while the intensities are averaged out. C can vary from -1 (anti-correlated) to 0 (uncorrelated) and 1 (fully correlated). The cross-correlation analysis was exclusively executed on the cell area. Two cell areas were considered, areas containing domains and the remaining areas. For ten different cells the cross correlation coefficient in domain rich regions was 0.40 ± 0.17, while the cross correlation coefficient in the remaining non-domain regions was calculated to be 0.17 ± 0.09. Similar cross-correlation values were obtained by performing the analysis on measurements of cells with Cy5 - IL-2Rα, Alexa488 - IL-15Rα and Alexa488 - IL-2Rα, Cy5 - IL-15Rα, i.e. 0.48 ± 0.15 for domain rich regions and 0.23 ± 0.14, excluding in this way any artifacts due to cell autofluorescence and differences in labeling efficiency.

6.5 Discussion

In this work we have investigated the nano-scale organization of two cytokine receptor subunits IL-2Rα and IL-15Rα, on the membrane of human T lymphoma cells. Both receptors IL-2R and IL15R are capable of initiating a signaling cascade when binding to their own cytokine, IL-2 and IL-15, respectively. Both cytokine/receptor systems play a key role in cell survival as well as in the control of activation-induced cell death, performing both similar and opposite functions. IL-2R and IL-15R share two signaling receptor subunits, i.e. β and γ_c, and have their own private α - subunit. We have focused on these two α subunits, IL-2Rα and IL-15Rα, as they seem to be the key to the difference in signals given to the cell. The use of NSOM combined with single molecule detection sensitivity has provided new insights into the organization of these receptors.

High resolution imaging of IL-2Rα confirms the existence of domains of typically 450 nm diameter, in good agreement with earlier reported electron microscopy studies [200]. Although clustering of IL-2Rα has also been inferred by confocal microscopy [200], direct analysis of cluster size and density has been lacking so far. Here we have directly observed IL-2Rα - domains by fluorescent means. It has been reported that the clustering of IL-2Rα is associated with the presence of lipid rafts [201]. In fact, several experiments have shown that clustering of IL-2Rα depends on the integrity of cholesterol-rich lipid rafts. Although the physiological significance of this type of lateral organization is not fully clear yet, experimental evidence suggests that rafts assist Il-2Rα recruitment to the vicinity of the signaling subunits β and γ_c. This process of aggregation then facilitates the formation of the high affinity receptor IL-2R, creating a focusing platform that regulates binding and signaling of IL-2 [201].

In similar high resolution experiments we also observed clustering of the IL-15Rα receptor on the membrane of human T lymphoma cells. Surprisingly, the IL-15Rα domain sizes were similar to those of IL-2Rα domains, as shown in the size distribution of Figure 6.7(b). Furthermore, co-localization experiments using dual labeling of both α subunits showed a significant degree of co-localization between both IL-2Rα and IL-15Rα clusters. Based on these observations, our data proves that IL-2Rα and IL-15Rα co-exist in the same domains, strongly suggesting that IL-15Rα is also associated with lipid rafts. These results indicate that both IL-2 and IL-15 require the lipid raft platforms in order to optimize their signaling capabilities, providing the so-called 'focusing effect' [201]. As already postulated by experts in the field of functional domains [36, 184, 193, 226], the experiments presented here significantly support the view that nanometer-sized domains could be common among various receptor types. In fact, the possible association of the pathogen recognition receptor DC-SIGN with lipid rafts was also discussed in Chapter 3.

In addition to clustering, we also observed a minor fraction of IL-2Rα ($\sim 1\%$) to be located at the cell membrane as small aggregates consisting of only a few proteins or even as single entities. Previous FRET experiments already hinted at the existence of a minor fraction of IL-2Rα subunits associated with TrfR, which is known to be excluded from lipid rafts [201]. Using confocal microscopy it was shown that TrfR forms domains with sizes between 200 - 300 nm, which is very close to the diffraction limit of the excitation light used for imaging ($\lambda_{excitation} = 534\,\mathrm{nm}$) [200]. The sizes of the individual entities observed in our experiments are aperture-sized, i.e. ~ 90 nm. Moreover, intensity analysis showed that these entities are most probably individual IL-2Rα molecules. These findings strongly indicate that we are directly observing the fraction of IL-2Rα proteins that are associated with TrfR. Damjanovich and coworkers suggested that the association of IL-2Rα with the TrfR domains provides an efficient endocytosis pathway for the excess of IL-2Rα subunits not involved in signal transduction [201]. Since IL-2 mediated signal transduction exclusively occurs in the presence of the β and γ_c subunits, the fraction of the α chains localized outside the large clusters should lack the corresponding β and γ_c subunits. High-resolution near-field co-localization experiments with all three labeled IL-2R subunits should provide further information on this hypothesis.

In contrast to IL-2Rα, a considerable fraction ($\sim 30\%$) of IL-15Rα subunits was found to reside outside the domains and appeared distributed in smaller clusters or even as single entities. Furthermore, a low cross-correlation coefficient was found between IL-2Rα and IL-15Rα in the non-clustered regions. It is known that individual IL-15Rα subunits have a high binding affinity to IL-15 and is thought that the IL-15Rα - IL-15 complex is capable of signaling without the presence of β and γ_c subunits [218]. Therefore, the relatively large fraction of IL-15Rα not associated with the domains is probably functional and not involved in any endocytosis pathway.

The intensity distributions shown in Figure 6.6 indicate that the molecular density of IL-2Rα domains is ten times higher than in IL-15Rα domains. In earlier flow-cytometry studies it was shown that activated T cells express 10 to 20 times more IL-2Rα subunits than β or γ_c subunits [201, 221]. Combining our results with these observations, we conclude that the expression level of IL-15Rα within domains is comparable to the expression level of β and γ_c subunits on the membrane. There are several possibilities regarding the (pre-)assembly of both complete receptor constructs (α, β and γ_c). 1) Both receptors are pre-assembled separately from each other in *IL-2Rα,β,γ_c* and *IL-15Rα,β,γ_c* constructs 2) The receptors share both α subunits in a IL-15Rα-β-γ_c-IL-2Rα tetramer construct. 3) All receptor subunits are produced separately, implying that IL-2Rα and IL-15Rα subunits have to compete to form a high affinity receptor. As there are ten times more IL-2Rα than IL-15Rα, β and γ_c proteins in the domains, there will be only few complete IL-15R assemblies. In this situation it seems reasonable to assume that the signaling capability is predominantly performed by the IL-2 - IL2R complex. It is probable that the cell orchestrates the signaling contribution from both cytokine receptors by regulating of the expression of the α subunits. To verify this hypothesis, the expression levels and the fractions of α molecules in and outside domains should be examined at various moments after T cell activation. As already mentioned, we found more than a tenfold expression of IL-2Rα with respect to IL-15Rα in the domain regions. The reasons for the abundance of IL-2Rα with respect to the IL-15Rα and the common β and γ_c subunits is not yet understood. Although highly speculative at the moment, one could argue that the IL-2Rα subunits form oligomers that would join the β - γ_c to form a larger complex than the regular IL-2R trimer. Intriguingly, despite the abundance of IL-2Rα and the apparent redundance with respect to the number of available β and γ_c subunits, a low percentage of IL-2Rα subunits resides outside the domains. As this fraction is likely to be endocytosed due to its proximity to TrfR [201], it might well be that the excess of IL-2Rα subunits inside the domains is inaccessible for endocytosis because of their involvement in rafts. However, as rafts are known to be dynamic structures [36, 193], dynamic measurements of IL-xRα domains should shed light on this speculation.

From Figure 6.8 it follows that the molecular density of both IL-2Rα and IL-15Rα domains are constant, irrespectively of the domain size. Apparently, there are various distinct ways for the cell to organize its surface proteins. As shown in Chapter 3, the pathogen recognition receptor, DC-SIGN also clusters in domains but with a completely different molecular packing density for each domain. It is probable that the constant molecular densities of IL-2Rα and IL-15Rα are optimized for the signaling function of the domains. It seems reasonable that all signaling domains on the cell surface would respond with the same signaling strength, explaining the comparable receptor density for all domains. Finally, the similarity of both types of domains in size and density hints to a general mechanism of domain formation.

6.6 Conclusions

IL-15R and IL-2R, chemically similar molecular complexes, perform both similar and opposing signaling functions after T cell activation. The reason for this behavior is up to now unknown. We hypothesized that the spatial organization of both receptors on the cell membrane might play a key role in their respective functions. Since the α subunits of IL-2Rα and IL-15Rα are unique for both receptors we investigated their spatial organization and expression level. We discovered that IL-2Rα and IL-15Rα exist both as individual entities as well as domains on the cell surface. Only a minor fraction of IL-2Rα reside outside the domains while as many as $\sim 30\%$ of IL-15Rα subunits are spread as individuals or small clusters, excluded from the main domain regions. IL-2Rα and IL-15Rα domains have a diameter of ~ 450 and 360 nm respectively and exhibit a constant packing density of $\sim 1350\,\text{IL-2R}\alpha/\mu\text{m}^2$ and $\sim 120\,\text{IL-15R}\alpha/\mu\text{m}^2$. A constant intermolecular separation for mutual IL-2Rα and IL-15Rα subunits might be efficient for IL-2Rα and IL-15Rα to perform their signaling function and hints for a common way of organization. Indeed, dual color experiments showed co-localization of IL-2Rα and IL-15Rα domains, indicating that the domains gather IL-2R and IL-15R to facilitate and optimize cell signaling.

References

[1] R. Hooke, *Micrographia, or some physiological descriptions of minute bodies made by magnifying glasses with observations and inquieries thereupon*, Royal society, London (1665).

[2] *http://micro.magnet.fsu.edu/optics*, .

[3] E. Hecht, *Optics, 2nd ed.*, Addison-Wesley Publishing Company ISBN 0201116111 (1987).

[4] *Encyclopaedia Britannica*, (2003).

[5] *http://www.zeiss.com*, 2003 .

[6] D. J. Stephens and V. J. Allan, *Light microscopy techniques for live cell Imaging*, Science **300**, 82 (2003).

[7] J. R. Lakowicz, *Principles of Fluorescence Spectroscopy, 2nd ed.*, Plenum Pr ISBN 0306460939 (1999).

[8] J. C. H. Spence, *High-resolution electron microscopy, 3rd ed.*, Oxford University Press ISBN 0198509154 (2003).

[9] E. Meyer, H. J. Hug, and R. Bennewitz, *Scanning Probe microscopy: The lab on a tip, 1st ed.*, Springer Verlag ISBN 3540431802 (2003).

[10] B. Alberts, D. Bray, J. Lewis, M. Raff, K. Roberts, and J. D. Watson, *Molecular biology of the cell, 3rd ed*, Garland Publishing ISBN 0815316194 (1994).

[11] K. Richter, *Cutting artifacts on ultrathin cryosections of biological bulk specimens*, Micron **25**, 297 (1994).

[12] J. L. Alonso and W. Goldmann, *Feeling the forces: atomic force microscopy in cell biology*, Life Sci. **72**, 2553 (2003).

[13] C. LeGrimellec, E. Lesniewska, M. C. Giocondi, E. Finot, V. Vie, and J. P. Goudonnet, *Imaging of the Surface of Living Cells by Low-Force Contact-Mode Atomic Force Microscopy*, Biophys. J. **75**, 695 (1998).

[14] G. Binning, C. F. Quate, and C. Gerber, *Atomic Force Microscope*, Phys. Rev. Lett. **56**, 930 (1986).

[15] B. C. van der Aa, R. M. Michel, M. Asther, M. T. Zamora, P. G. Rouxhet, and Y. F. Dufrene, *Stretching cell surface macromolecules by atomic force*

microscopy, Langmuir **17**, 3116 (2001).

[16] Y. F. Dufrene, *Application of atomic force microscopy to microbial surfaces: from reconstituted cell surface layers to living cells*, Micron **32**, 153 (2001).

[17] F. Kienberger, C. Stroh, G. Kada, R. Moser, W. Baumgartner, V. Pastushenko, C. Rankl, U. Schmidt, H. Muller, E. Orlova, C. LeGrimellec, D. Drenckhahn, D. Blaas, and P. Hinterdorfer, *Dynamic force microscopy imaging of native membranes*, Ultramicroscopy **97**, 229 (2003).

[18] E. Henderson, P. G. Haydon, and D. S. Sakaguchi, *Actin Filament Dynamics in Living Glial Cells Imaged by Atomic Force Microscopy*, Science **257**, 1944 (1992).

[19] U. G. Hofmann, C. Rotsch, W. J. Parak, and M. Radmacher, *Investigating the cytoskeleton of chicken cardiocytes with the atomic force microscope*, J. Struct. Biol. **119**, 84 (1997).

[20] J. Domke, W. J. Parak, M. George, H. E. Gaub, and M. Radmacher, *Mapping the mechanical pulse of single cardiomyocytes with the atomic force microscope*, Eur. Biophys. J. **28**, 179 (1999).

[21] K. O. van der Werf, C. A. J. Putman, B. G. de Grooth, and J. Greve, *Adhesion force imaging in air and liquid by adhesion mode atomic force microscopy*, Appl. Phys. Lett. **65**, 1195 (1994).

[22] O. H. Willemsen, M. M. E. Snel, A. Cambi, J. Greve, B. G. de Grooth, and C. G. Figdor, *Biomolecular Interactions Measured by Atomic Force Microscopy*, Biophys. J. **79**, 3267 (2000).

[23] S. A. Vickery and R. C. Dunn, *Combining AFM and FRET for high resolution fluorescence microscopy*, J. Microscopy **202**, 408 (2001).

[24] Y. F. Dufrene, *Direct Characterization of the Physicochemical Properties of Fungal Spores Using Functionalized AFM Probes*, Biophys. J. **78**, 3286 (2000).

[25] S. B. Velegol and B. E. Logan, *Contributions of bacterial surface polymers, electrostatics, and cell elasticity to the shape of AFM force curves*, Langmuir **18**, 5256 (2002).

[26] W. H. Goldmann, R. Galneder, M. Ludwig, W. M. Xu, E. D. Adamson, N. Wang, and R. M. Ezzell, *Differences in elasticity of vinculin-deficient F9 cells measured by magnetometry and atomic force microscopy*, Exp. Cell Res. **239**, 235 (1998).

[27] U. Dammer, O. Popescu, P. Wagner, D. Anselmetti, H. J. Guntherodt, and G. N. Misevic, *Binding strength between cell-adhesion proteoglycans measured by atomic-force microscopy*, Science **267**, 1173 (1995).

[28] O. H. Willemsen, M. M. E. Snel, K. O. van der Werf, B. G. de Grooth, J. Greve, P. Hinterdorfer, H. J. Gruber, H. Schindler, Y. van Kooyk, and C. G.

Figdor, *Simultaneous height and adhesion imaging of antibody-antigen interactions by atomic force microscopy*, Biophys. J. **75**, 2220 (1998).

[29] D. W. Pohl, W. Denk, and M. Lanz, *Optical stethoscopy: Image recording with resolution l/20*, Appl. Phys. Lett. **44**, 651 (1984).

[30] E. Betzig and J. K. Trautman, *Near-field optics: microscopy, spectroscopy, and surface modification beyond the diffraction limit*, Science **257**, 189 (1992).

[31] M. A. Paesler and P. J. Moyer, *Near-field optics, theory, instrumentation and applications*, Wiley-Interscience ISBN 0471043117 (1996).

[32] A. J. Lacey, *Light microscopy in biology - a practical approach, 2nd ed.*, Oxford University Press ISBN 0199636699 (1999).

[33] E. Betzig, P. L. Finn, and J. S. Weiner, *Combined shear force and near-field scanning optical microscopy*, Appl. Phys. Lett **60**, 2484 (1992).

[34] N. F. van Hulst and M. H. P. Moers, *Biological application of near-field optical microscopy*, IEEE Eng. Med. Biol. Mag. **15**, 51 (1996).

[35] A. Lewis, A. Radko, N. Benami, D. Palanker, and K. Lieberman, *Integration of atomic force and confocal microscopy*, Trends Cell Biol. **9**, 70 (1999).

[36] M. Edidin, *The state of lipid rafts: from model membranes to cells*, Annu. Rev. Biophys. Biomol. Struct. **32**, 257 (2003).

[37] F. de Lange, A. Cambi, R. Huijbens, B. I. de Bakker, W. Rensen, M. F. Garcia-Parajo, N. F. van Hulst, and C. G. Figdor, *Cell biology beyond the diffraction limit: near-field scanning optical microscopy*, J. Cell Sci. **114**, 4153 (2001).

[38] M. M. Hao and F. R. Maxfield, *Analyzing microdomains in biological membranes using fluorescence techniques*, J. Fluor. **11**, 287 (2001).

[39] T. Enderle, T. Ha, D. S. Chemla, and S. Weiss, *Near-field fluorescence microsocpy of cells*, Ultramicroscopy **71**, 303 (1998).

[40] E. Betzig and R. J. Chichester, *Single molecules observed by near-field scanning optical microscopy*, Science **262**, 1422 (1993).

[41] N. F. van Hulst, M. F. Garcia-Parajo, M. H. P. Moers, J. A. Veerman, and A. G. T. Ruiter, *Near-field fluorescence imaging of genetic material: Toward the molecular limit*, J. Struct. Biol. **119**, 222 (1997).

[42] M. F. Garcia-Parajo, J. A. Veerman, S. J. T. van Noort, B. G. de Grooth, J. Greve, and N. F. van Hulst, *Near-field optical microscopy for DNA studies at the single molecular level*, Bioimaging **6**, 43 (1998).

[43] N. Billinton and A. W. Knight, *Seeing the wood through the trees: A review of techniques for distinguishing green fluorescent protein from endogenous autofluorescence*, Anal. Biochem. **291**, 175 (2001).

[44] M. Haitinger, *Fluoreszenz-Mikroskopie*, Akademische Varlagsgesellschaft, Geest und Portig K.-G., Leipzig (1959).

[45] A. H. Coons, H. J. Creech, and R. N. Jones, *Immunological properties of an antibody containing a fluorescent group*, Proc. Soc. Exp. Biol. Med. **47**, 200 (1941).

[46] R. Y. Tsien, *The green fluorescent protein*, Annu. Rev. Biochem. **67**, 509 (1998).

[47] A. Miyawaki, A. Sawano, and T. Kogure, *Lighting up cells: labelling proteins with fluorophores*, Nat. Cell Biol. S1 (2003).

[48] P. van Roessel and A. H. Brand, *Imaging into the future: visualizing gene expression and protein interactions with fluorescent proteins*, Nat. Cell Biol. **4**, E15 (2002).

[49] L. Cognet, F. Coussen, D. Choquet, and B. Lounis, *Fluorescence microscopy of single autofluorescent proteins for cellular biology*, Compt. Rend. Physique **3**, 645 (2002).

[50] J. B. Pawley, *Handbook of Biological Confocal Microscopy, 2nd ed.*, Plenum Press, New York ISBN 0306448262 (1995).

[51] R. H. Webb, *Confocal optical microscopy*, Rep. Prog. Phys. **59**, 427 (1996).

[52] D. W. Piston, *Imaging living cells and tissues by two-photon excitation microscopy*, Trends Cell Biol. **9**, 66 (1999).

[53] K. J. Halbhuber and K. Konig, *Modern laser scanning microscopy in biology, biotechnology and medicine*, Ann. Anat. **185**, 1 (2003).

[54] W. Denk, J. H. Strickler, and W. W. Webb, *Two-photon laser scanning fluorescence microscopy*, Science **248**, 73 (1990).

[55] F. Helmchen and W. Denk, *New developments in multiphoton microscopy*, Curr. Opin. Neurobiol. **12**, 593 (2002).

[56] S. W. Hell and E. H. K. Stelzer, *Properties of a 4Pi confocal fluorescence microscope*, J. Opt. Soc. Am. A **9**, 2159 (1992).

[57] S. W. Hell and J. Wichmann, *Breaking the diffraction resolution limit by stimulated emission: stimulated-emission-depletion fluorescence microscopy*, Opt. Lett. **19**, 780 (1994).

[58] S. Weiss, *Shattering the diffraction limit of light: A revolution in fluorescence microscopy?*, Proc. Natl. Acad. Sci. U.S.A. **97**, 8747 (2000).

[59] M. Schrader, K. Bahlmann, G. Giese, and S. W. Hell, *4Pi-confocal imaging in fixed biological specimens*, Biophys. J. **75**, 1659 (1998).

[60] K. Bahlmann, S. Jakobs, and S. W. Hell, *4Pi-confocal microscopy of live cells*, Ultramicroscopy **87**, 155 (2001).

[61] A. Egner, S. Jakobs, and S. W. Hell, *Fast 100-nm resolution three-dimensional microscope reveals structural plasticity of mitochondria in live*

yeast, Proc. Natl. Acad. Sci. U.S.A. **99**, 3376 (2002).

[62] M. D. Cahalan, I. Parker, S. H. Wei, and M. J. Miller, *Two photon tissue imaging: seeing the immune response in a fresh light*, Nat. Rev. Immunol. **2**, 872 (2002).

[63] M. J. Miller, A. S. Hejazi, S. H. Wei, M. D. Cahalan, and I. Parker, *T cell repertoire scanning is promoted by dynamic dendritic cell behavior and random T cell motility in the lymph node*, Proc. Natl. Acad. Sci. U.S.A. **101**, 998 (2004).

[64] T. A. Klar, S. Jakobs, M. Dyba, A. Egner, and S. W. Hell, *Fluorescence microscopy with diffraction resolution barrier broken by stimulated emission*, Proc. Natl. Acad. Sci. U.S.A. **97**, 8206 (2000).

[65] E. A. Jares-Erijman and T. M. Jovin, *FRET imaging*, Nat. Biotechnol. **21**, 1387 (2003).

[66] P. R. Selvin, *The renaissance of fluorescence resonance energy transfer*, Nat. Struct. Biol. **7**, 730 (2000).

[67] R. B. Sekar and A. Periasamy, *Fluorescence resonance energy transfer (FRET) microscopy imaging of live cell protein localizations*, J. Cell Biol. **160**, 629 (2003).

[68] D. Klostermeier and D. P. Millar, *RNA conformation and folding studied with fluorescence resonance energy transfer*, Methods **23**, 240 (2001).

[69] T. Heyduk, *Measuring protein conformational changes by FRET/LRET*, Curr. Opin. Biotechnol. **13**, 292 (2002).

[70] R. C. Dunn, *Near-field scanning optical microscopy*, Chem. Rev. **99**, 2891 (1999).

[71] E. Betzig, J. K. Trautman, T. D. Harris, J. S. Weiner, and R. L. Kostelak, *Breaking the diffraction barrier - optical microscopy on a nanometric scale*, Science **251**, 1468 (1991).

[72] J. A. Veerman, A. M. Otter, L. Kuipers, and N. F. van Hulst, *High definition aperture probes for near-field optical microscopy fabricated by focused ion beam milling*, Appl. Phys. Lett. **72**, 3115 (1998).

[73] A. G. T. Ruiter, J. A. Veerman, K. O. van der Werf, and N. F. van Hulst, *Dynamic behavior of tuning fork shear-force feedback*, Appl. Phys. Lett. **71**, 28 (1997).

[74] V. Subramaniam, A. K. Kirsch, and T. M. Jovin, *Cell biological applications of scanning near-field optical microscopy (SNOM)*, Cell Mol. Biol. **44**, 689 (1998).

[75] J. Hwang, L. A. Gheber, L. Margolis, and M. Edidin, *Domains in cell plasma membranes investigated by near-field scanning optical microscopy*, Biophys. J. **74**, 2184 (1998).

[76] T. Enderle, T. Ha, D. F. Ogletree, D. S. Chemla, C. Magowan, and S. Weiss, *Membrane specific mapping and colocalization of malarial and host skeletal proteins in the Plasmodium falciparum infected erythrocyte by dual-color near-field scanning optical microscopy*, Proc. Natl. Acad. Sci. U.S.A. **94**, 520 (1997).

[77] P. Nagy, A. Jenei, A. K. Kirsch, J. Szollosi, S. Damjanovich, and T. M. Jovin, *Activation-dependent clustering of the erbB2 receptor tyrosine kinase detected by scanning near-field optical microscopy*, J. Cell Sci. **112**, 1733 (1999).

[78] E. Betzig, R. J. Chichester, F. Lanni, and D. L. Taylor, *Near-field fluorescence imaging of cytoskeletal actin*, Bioimaging **1**, 129 (1993).

[79] A. K. Kirsch, V. Subramaniam, A. Jenei, and T. M. Jovin, *Fluorescence resonance energy transfer detected by scanning near-field optical microscopy*, J. Microsc. **194**, 448 (1999).

[80] S. B. Smith, Y. Cui, and C. Bustamante, *Optical-trap force transducer that operates by direct measurement of light momentum*, Biophoton., PT B, Methods enzymol. **361**, 134 (2003).

[81] K. Wang, J. G. Forbes, and A. J. Jin, *Single molecule measurements of titin elasticity*, Prog. Biophys. Mol. Biol. **77**, 1 (2001).

[82] A. D. Mehta, M. Rief, J. A. Spudich, D. A. Smith, and R. M. Simmons, *Single-molecule biomechanics with optical methods*, Science **283**, 1689 (1999).

[83] A. Engel and D. J. Muller, *Observing single biomolecules at work with the atomic force microscope*, Nat. Struct. Biol. **7**, 715 (2000).

[84] T. E. Fisher, P. E. Marszalek, and J. M. Fernandez, *Stretching single molecules into novel conformations using the atomic force microscope*, Nat. Struct. Biol. **7**, 719 (2000).

[85] M. Carrion-Vazquez, A. F. Oberhauser, T. E. Fisher, P. E. Marszalek, H. B. Li, and J. M. Fernandez, *Mechanical design of proteins-studied by single-molecule force spectroscopy and protein engineering*, Prog. Biophys. Mol. Biol. **74**, 63 (2000).

[86] T. Hugel and M. Seitz, *The study of molecular interactions by AFM force spectroscopy*, Macromol. Rapid Commun. **22**, 989 (2001).

[87] H. G. Hansma, *Surface biology of DNA by atomic force microscopy*, Annu. Rev. Phys. Chem. **52**, 71 (2001).

[88] S. M. Nie and R. N. Zare, *Optical detection of single molecules*, Annu. Rev. Biophys. Biomol. Struct. **26**, 567 (1997).

[89] X. S. Xie and J. K. Trautman, *Optical studies of single molecules at room temperature*, Annu. Rev. Phys. Chem. **49**, 441 (1998).

[90] W. E. Moerner and M. Orrit, *Illuminating Single Molecules in Condensed Matter*, Science **283**, 1670 (1999).

[91] A. Ishijima and T. Yanagida, *Single molecule nanobioscience*, Trends Biochem. Sci. **26**, 438 (2001).

[92] W. E. Moerner, *A dozen year of single-molecule spectroscopy in physics, chemistry, and biophysics*, J. Phys. Chem. B **106**, 910 (2002).

[93] M. Bohmer and J. Enderlein, *Fluorescence spectroscopy of single molecules under ambient conditions: Methodology and technology*, Chem. Phys. Chem. **4**, 793 (2003).

[94] W. E. Moerner and D. P. Fromm, *Methods of single-molecule fluorescence spectroscopy and microscopy*, Rev. Sci. Instrum. **74**, 3597 (2003).

[95] Y. Sako and T. Yanagida, *Single-molecule visualization in cell biology*, Nat. Cell Biol. SS1 (2003).

[96] J. Zhang, Q. Chi, A. M. Kuznetsov, A. G. Hansen, H. Wackerbarth, H. E. M. Christensen, J. E. T. Andersen, and J. Ulstrup, *Electronic properties of functional biomolecules at metal/aqueous solution interfaces*, J. Phys. Chem. B **106**, 1131 (2002).

[97] T. Ide and T. Yanagida, *An Artificial Lipid Bilayer Formed on an Agarose-Coated Glass for Simultaneous Electrical and Optical Measurement of Single Ion Channels*, Biochem. Biophys. Res. Commun. **265**, 595 (1999).

[98] S. Weiss, *Fluorescence spectroscopy of single biomolecules*, Science **283**, 1676 (1999).

[99] Y. L. Wang and D. L. T. (editor), *Fluorescence microscopy of living cells in culture, Part A*, Academic Press ISBN 0126847541 (1989).

[100] T. Schmidt, W. Baumgartner, G. J. Schutz, H. J. Gruber, and H. Schindler, *Imaging of single molecule diffusion*, Proc. Natl. Acad. Sci. U.S.A. **93**, 2926 (1996).

[101] V. Borisenko, T. Lougheed, J. Hesse, E. Fureder-Kitzmuller, N. Fertig, J. C. Behrends, G. A. Woolley, and G. J. Schutz, *Simultaneous optical and electrical recording of single gramicidin channels*, Biophys. J. **84**, 612 (2003).

[102] A. Sonnleitner, G. J. Schutz, and T. Schmidt, *Free brownian motion of individual lipid molecules in biomembranes*, Biophys. J. **77**, 2638 (1999).

[103] M. Vrljic, S. Y. Nishimura, S. Brasselet, W. E. Moerner, and H. M. McConnell, *Translational diffusion of individual class II MHC membrane proteins in cells*, Biophys. J. **83**, 2681 (2002).

[104] T. Kues, R. Peters, and U. Kubitscheck, *Visualization and tracking of single protein molecules in the cell nucleus*, Biophys. J. **80**, 2954 (2001).

[105] A. Femino, F. S. Fay, K. Fogarty, and R. H. Singer, *Visualization of single*

RNA transcripts in situ, Science **280**, 585 (1998).

[106] G. Seisenberger, M. U. Ried, T. Endress, H. Buning, M. Hallek, and C. Brauchle, *Real-time single-molecule imaging of the infection pathway of an adeno-associated virus*, Science **294**, 1929 (2001).

[107] G. S. Harms, L. Cognet, P. H. M. Lommerse, G. A. Blab, H. Kahr, R. Gamsjager, H. P. Spaink, N. M. Soldatov, C. Romanin, and T. Schmidt, *Single-molecule imaging of L-type Ca2+ channels in live cells*, Biophys. J. **81**, 2639 (2001).

[108] T. Ha, T. Enderle, D. F. Ogletree, D. S. Chemla, P. R. Selvin, and S. Weiss, *Probing the interaction between two single molecules: Fluorescence resonance energy transfer between a single donor and a single acceptor*, Proc. Natl. Acad. Sci. U.S.A. **93**, 6264 (1996).

[109] C. Eggeling, J. R. Fries, L. Brand, R. Gunther, and C. A. M. Seidel, *Monitoring conformational dynamics of a single molecule by selective fluorescence spectroscopy*, Proc. Natl. Acad. Sci. U.S.A. **95**, 1556 (1998).

[110] T. Ha, X. W. Zhuang, H. D. Kim, J. W. Orr, J. R. Williamson, and S. Chu, *Ligand-induced conformational changes observed in single RNA molecules*, Proc. Natl. Acad. Sci. U.S.A. **96**, 9077 (1999).

[111] D. S. Talaga, W. L. Lau, H. Roder, J. Y. Tang, Y. W. Jia, W. F. DeGrado, and R. M. Hochstrasser, *Dynamics and folding of single two-stranded coiled-coil peptides studied by fluorescent energy transfer confocal microscopy*, Proc. Natl. Acad. Sci. U.S.A. **97**, 13021 (2000).

[112] G. M. J. Segers-Nolten, C. Wyman, N. Wijgers, W. Vermeulen, A. T. M. Lenferink, J. H. J. Hoeijmakers, J. Greve, and C. Otto, *Scanning confocal fluorescence microscopy for single molecule analysis of nucleotide excision repair complexes*, Nucleic Acids Res. **30**, 4720 (2002).

[113] B. Schuler, E. A. Lipman, and W. A. Eaton, *Probing the free-energy surface for protein folding with single-molecule fluorescence spectroscopy*, Nature **419**, 743 (2002).

[114] E. A. Lipman, B. Schuler, O. Bakajin, and W. A. Eaton, *Single-molecule measurement of protein folding kinetics*, Science **301**, 1233 (2003).

[115] E. Rhoades, E. Gussakovsky, and G. Haran, *Watching proteins fold one molecule at a time*, Proc. Natl. Acad. Sci. U.S.A. **100**, 3197 (2003).

[116] G. J. Schutz and P. Hinterdorfer, *Single molecule fluorescence and force microscopy*, Exp. Gerontol. **37**, 1493 (2002).

[117] P. Schwille, U. Haupts, S. Maiti, and W. W. Webb, *Molecular dynamics in living cells observed by fluorescence correlation spectroscopy with one- and two-photon excitation*, Biophys. J. **77**, 2251 (1999).

[118] P. Schwille, S. Kummer, A. A. Heikal, W. E. Moerner, and W. W. Webb,

Fluorescence correlation spectroscopy reveals fast optical excitation-driven intramolecular dynamics of yellow fluorescent proteins, Proc. Natl. Acad. Sci. U.S.A. **97**, 151 (2000).

[119] P. Schwille, *Fluorescence correlation spectroscopy and its potential for intracellular applications*, Cell Biochem. Biophys. **34**, 383 (2001).

[120] T. A. Byassee, W. C. W. Chan, and S. M. Nie, *Probing single molecules in single living cells*, Anal. Chem. **72**, 5606 (2000).

[121] E. Haustein and P. Schwille, *Ultrasensitive investigations of biological systems by fuorescence correlation spectroscopy*, Methods **29**, 153 (2003).

[122] D. Axelrod, *Cell-substrate contacts illuminated by total internal reflection fluorescence*, J. Cell Biol. **89**, 141 (1981).

[123] D. Axelrod, *Total Internal Reflection Fluorescence Microscopy in Cell Biology*, Traffic **2**, 764 (2001).

[124] D. Toomre and D. J. Manstein, *Lighting up the cell surface with evanescent wave microscopy*, Trends Cell Biol. **11**, 298 (2001).

[125] T. Funatsu, Y. Harada, M. Tokunaga, K. Saito, and T. Yanagida, *Imaging of single fluorescent molecules and individual ATP turnovers by single myosin molecules in aqueous solution*, Nature **374**, 555 (1995).

[126] N. L. Thompson and B. C. Lagerholm, *Total internal reflection fluorescence: applications in cellular biophysics*, Curr. Opin. Biotechnol. **8**, 58 (1997).

[127] Y. Sako, S. Minoguchi, and T. Yanagida, *Single-molecule imaging of EGFR signalling on the surface of living cells*, Nat. Cell Biol. **2**, 168 (2002).

[128] Y. Ishii and T. Yanagida, *Single molecule detection in life science*, Single. Mol. **1**, 5 (2000).

[129] R. Iino, I. Koyama, and A. Kusumi, *Single molecule imaging of green fluorescent proteins in living cells: E-cadherin forms oligomers on the free cell surface*, Biophys. J. **80**, 2667 (2001).

[130] M. Ueda, Y. Sako, T. Tanaka, P. Devreotes, and T. Yanagida, *Single-molecule analysis of chemotactic signaling in dictyostelium cells*, Science **294**, 864 (2001).

[131] K. Hibino, T. M. Watanabe, J. Kozuka, A. H. Iwane, T. Okada, T. Kataoka, T. Yanagida, and Y. Sako, *Single- and multiple-molecule dynamics of the signaling from H-Ras to cRaf-1 visualized on the plasma membrane of living cells*, Chem. Phys. Chem. **4**, 748 (2003).

[132] K. F. Giebel, C. Bechinger, S. Herminghaus, M. Riedel, P. Leiderer, U. Weiland, and M. Bastmeyer, *Imaging of cell/substrate contacts of living cells with surface plasmon resonance microscopy*, Biophys. J. **76**, 509 (1999).

[133] M. Edidin, *Near-field scanning optical microscopy, a siren call to biology*,

Traffic **2**, 797 (2001).

[134] C. Hoppener, D. Molenda, H. Fuchs, and A. Naber, *Scanning near-field optical microscopy of a cell membrane in liquid*, J. Microsc. **210**, 288 (2003).

[135] L. A. Gheber, J. Hwang, and M. Edidin, *Design and optimization of a near-field scanning optical microscope for imaging biological samples in liquid*, Appl. Optics **37**, 3574 (1998).

[136] C. A. Janeway, P. Travers, M. Walport, and M. Shlomchik, *Immunobiology, 5th ed.*, Garland Publishing ISBN 081533642 (2001).

[137] D. A. Brown and E. London, *Structure and function of sphingolipid- and cholestorol-rich membrane rafts*, J. Biol. Chem. **275**, 17221 (2000).

[138] K. Jacobson and C. Dietrich, *Looking at lipid rafts?*, Trends Cell Biol. **9**, 87 (1999).

[139] R. G. W. Anderson and K. Jacobson, *Cell biology - A role for lipid shells in targeting proteins to caveolae, rafts, and other lipid domains*, Science **296**, 1821 (2002).

[140] M. Koopman, B. I. de Bakker, M. F. Garcia-Parajo, and N. F. van Hulst, *Shear force imaging of soft samples in liquid using a diving bell concept*, Appl. Phys. Lett. **83**, 5083 (2003).

[141] B. Hecht, B. Sick, U. P. Wild, V. Deckert, R. Zenobi, O. J. F. Martin, and D. W. Pohl, *Scanning near-field optical microscopy with aperture probes: Fundamentals and applications*, J. Chem. Phys. **112**, 7761 (2000).

[142] G. A. Valaskovic, M. Holton, and G. H. Morrison, *Parameter control, characterization, and optimization in the fabrication of optical-fiber near-field probes*, Appl. Optics **34**, 1215 (1995).

[143] H. Heinzelmann, J. M. Freyland, R. Eckert, T. Huser, G. Schurman, W. Noell, U. Staufer, and N. F. de Rooij, *Towards better scanning near-field optical microscopy probes - progress and new developments*, J. Microsc. **194**, 365 (1999).

[144] K. Karrai and R. D. Grober, *Piezoelectric tip-sample distance control for near-field optical microscopes*, Appl. Phys. Lett. **66**, 1842 (1995).

[145] W. H. J. Rensen, *Tuning fork tunes, exploring new scanning probe techniques*, Ph.D. Thesis ISBN 9036517532 (2002).

[146] T. Schmidt, G. J. Schutz, W. Baumgartner, H. J. Gruber, and H. Schindler, *Characterization of photophysics and mobility of single molecules in a fluid lipid membrane*, J. Phys. Chem. **99**, 17662 (1995).

[147] G. J. Schutz, H. Schindler, and T. Schmidt, *Single-molecule microscopy on model membranes reveals anomalous diffusion*, Biophys. J. **73**, 1073 (1997).

[148] A. M. van Oijen, J. Kohler, J. Schmidt, M. Muller, and G. J. Brakenhoff, *3-Dimensional super-resolution by spectrally selective imaging*, Chem. Phys.

Lett. **292**, 183 (1998).

[149] G. J. Schutz, J. Hesse, G. Freudenthaler, V. P. Pastushenko, H. G. Knaus, B. Pragl, and H. G. Schindler, *3D Mapping of individual ion channels on living cells*, Single Mol. **1**, 153 (2000).

[150] T. D. Lacoste, X. Michalet, F. Pinaud, D. S. Chemla, A. P. Alivisatos, and S. Weiss, *Ultrahigh-resolution multicolor colocalization of single fluorescent probes*, Proc. Natl. Acad. Sci. U.S.A. **97**, 9461 (2000).

[151] M. Schmidt, M. Nagorni, and S. W. Hell, *Subresolution axial distance measurements in far-field fluorescence microscopy with precision of 1 nanometer*, Rev. Sci. Instrum. **71**, 2742 (2000).

[152] X. Michalet, T. D. Lacoste, and S. Weiss, *Ultrahigh-resolution colocalization of spectrally separable point-like fluorescent probes*, Methods **25**, 87 (2001).

[153] A. Bloess, Y. Durand, M. Matsushita, H. van der Meer, G. J. Brakenhoff, and J. Schmidt, *Optical far-field microscopy of single molecules with 3.4 nm lateral resolution*, J. Microsc. **205**, 76 (2002).

[154] H. A. Bethe, *Theory of diffraction by small holes*, Phys. Rev. **66**, 163 (1944).

[155] C. J. Bouwkamp, *On Bethe's theory of diffraction by small holes*, Philips Res. Rep. **5**, 321 (1950).

[156] H. Gersen, M. F. Garcia-Parajo, L. Novotny, J. A. Veerman, L. Kuipers, and N. F. van Hulst, *Influencing the Angular Emission of a Single Molecule*, Phys. Rev. Lett. **85**, 5312 (2000).

[157] N. Bobroff, *Position measurement with a resolution and noise-limited instrument*, Rev. Sci. Instrum. **57**, 1152 (1986).

[158] K. P. Ni and H. C. O'Neill, *Improved FACS analysis confirms generation of immature dendritic cells in long-term stromal-dependent spleen cultures*, Immunol. Cell Biol. **78**, 196 (2000).

[159] S. J. Bell, R. Rigby, N. English, S. D. Mann, S. C. Knight, M. A. Kamm, and A. J. Stagg, *Migration and maturation of human colonic dendritic cells*, J. Immunol. **166**, 4958 (2001).

[160] A.Grakoui, S. Bromley, C.Sumen, M. Davis, A. Shaw, P. Allen, and M. Dustin, *The Immunological Synapse: A Molecular Machine Controlling T Cell Activation*, Science **285**, 221 (1999).

[161] A. Engering, T. B. H. Geijtenbeek, S. J. van Vliet, M. Wijers, E. van Liempt, N. Demaurex, A. Lanzavecchia, J. Fransen, C. G. Figdor, V. Piguet, , and Y. van Kooyk, *The dendritic cell-specific adhesion receptor DC-SIGN internalizes antigen for presentation to T cells*, J. Immunol. **168**, 2118 (2002).

[162] T. B. H. Geijtenbeek, R. Torensma, S. J. van Vliet, G. C. F. van Duijnhoven, G. J. Adema, Y. van Kooyk, and G. C. Figdor, *Identification of*

DC-SIGN, a novel dendritic cell-Specific ICAM-3 receptor that supports primary immune response, Cell **100**, 575 (2000).

[163] D. A. Bleijs, T. B. H. Geijtenbeek, C. G. Figdor, and Y. van Kooijk, *DC-SIGN and LFA-1: a battle for ligand*, Trends Immunol. **22**, 457 (2001).

[164] R. M. Steinman, *The dendritic cell system and its role in immunogenicity*, Annu. Rev. Immunol. **9**, 271 (1991).

[165] J. Banchereau and R. M. Steinman, *Dendritic cells and the control of immunity*, Nature **392**, 245 (1998).

[166] E. J. Soilleux, *DC-SIGN (dendritic cell-specific ICAM-grabbing non-integrin) and DC-SIGN-related (DC-SIGNR): friend or foe?*, Clin. Sci. **104**, 437 (2003).

[167] T. B. H. Geijtenbeek, D. J. E. B. Krooshoop, D. A. Bleijs, S. J. van Vliet, G. C. F. van Duijnhoven, V. Grabovsky, R. Alon, C. G. Figdor, and Y. van Kooyk, *DC-SIGN ICAM-2 interaction mediates dendritic cell trafficking*, Nat. Immunol. **1**, 353 (2000).

[168] B. Tassaneetrithep, T. H. Burgess, A. Granelli-Piperno, C. Trumpfherer, J. Finke, W. Sun, M. A. Eller, K. Pattanapanyasat, S. Sarasombath, D. L. Birx, R. M. Steinman, S. Schlesinger, and M. A. Marovich, *DC-SIGN (CD209) mediates dengue virus infection of human dendritic cells*, J. Exp. Med. **197**, 823 (2003).

[169] F. Halary, A. Amara, H. Lortat-Jacob, M. Messerle, T. Delaunay, C. Houles, F. Fieschi, F. Arenzana-Seisdedos, J. F. Moreau, and J. Dechanet-Merville, *Human cytomegalovirus binding to DC-SIGN is required for dendritic cell infection and target cell trans-infection*, Immunity **17**, 653 (2002).

[170] C. P. Alvarez, F. Lasala, J. Carrillo, O. Muniz, A. L. Corbi, and R. Delgado, *C-type lectins DC-SIGN and L-SIGN mediate cellular entry by Ebola virus in cis and in trans*, J. Virol. **76**, 6841 (2002).

[171] P. Y. Lozach, H. Lortat-Jacobs, A. D. de Lavalette, I. Staropoli, S. Foung, A. Amara, C. Houles, F. Fieschi, O. Schwarz, J. L. Virelizier, F. Arenzana-Seisdedos, and R. Altmeyer, *DC-SIGN and L-SIGN are high affinity binding receptors for hepatitis C virus glycoprotein E2*, J. Biol. Chem. **278**, 20358 (2003).

[172] S. Pohlmann, J. Zhang, F. Baribaud, Z. W. Chen, G. Leslie, G. Lin, A. Granelli-Piperno, R. W. Dom, C. M. Rice, and J. A. McsKeating, *Hepatitis C virus glycoproteins interact with DC-SIGN and DC-SIGNR*, J. Virol. **77**, 4070 (2003).

[173] M. Colmenares, A. Puig-Kroger, O. M. Pello, A. L. Corbi, and L. Rivas, *Dendritic cell (DC)-specific intercellular adhesion molecule 3 (ICAM-3)-grabbing nonintegrin (DC-SIGN, CD209), a C-type surface lectin in human*

DCs, is a receptor for Leishmania amastigotes, J. Biol. Chem. **277**, 36766 (2002).

[174] A. Cambi, K. Gijzen, J. M. de Vries, R. Torensma, B. Joosten, G. J. Adema, M. G. Netea, B. J. Kullberg, L. Romani, and C. G. Figdor, *The C-type lectin DC-SIGN (CD209) is an antigen-uptake receptor for Candida albicans on dendritic cells*, Eur. J. Immunol. **33**, 532 (2003).

[175] T. B. H. Geijtenbeek, S. J. van Vliet, E. A. Koppel, M. Sanchez-Hernandez, C. M. J. E. Vandenbroucke-Grauls, B. Appelmelk, and Y. van Kooyk, *Mycobacteria target DC-SIGN to suppress dendritic cell function*, J. Exp. Med. **197**, 7 (2003).

[176] L. Tailleux, O. Schwartz, J. L. Herrmann, E. Pivert, M. Jackson, A. Amara, L. Legres, D. Dreher, L. P. Nicod, J. C. Gluckman, P. H. Lagrange, B. Gicquel, and O. Neyrolles, *DC-SIGN is the major Mycobacterium tuberculosis receptor on human dendritic cells*, J. Exp. Med. **197**, 121 (2003).

[177] N. Maeda, J. Nigou, J. L. Herrmann, M. Jackson, A. Amara, P. H. Lagrange, G. Puzo, B. Gicquel, and O. Neyrolles, *The cell surface receptor DC-SIGN discriminates between Mycobacterium species through selective recognition of the mannose caps on lipoarabinomannan*, J. Biol. Chem. **278**, 5513 (2003).

[178] I. van Die, S. J. van Vliet, A. K. Nyame, R. D. Cummings, C. M. C. Bank, B. Appelmelk, T. B. H. Geijtenbeek, and Y. van Kooyk, *The dendritic cell-specific C-type lectin DC-SIGN is a receptor for Schistosoma mansoni egg antigens and recognizes the glycan antigen Lewis x*, Glycobiology **13**, 471 (2003).

[179] C. M. Rosenberger, J. H. Brumell, and B. B. Finlay, *Microbial pathogenesis: Lipid rafts as pathogen portals*, Curr. Biol. **10**, R823 (2000).

[180] P. J. Clark and F. C. Evans, *Distance to nearest neighbor as a measure of spatial relationships in populations*, Ecology **35**, 445 (1954).

[181] D. A. Mitchell, A. J. Fadden, and K. Drickamer, *A novel mechanism of carbohydrate recognition by the C-type lectins DC-SIGN and DC-SIGNR - Subunit organization and binding to multivalent ligands*, J. Biol. Chem. **276**, 28939 (2001).

[182] S. Manes, R. A. Lacalle, C. Gomez-Mouton, G. del Real, E. Mira, and A. C. Martinez, *Membrane raft microdomains in chemokine receptor function*, Semin. Immunol. **13**, 147 (2001).

[183] Y. Percherancier, B. Lagane, T. Planchenault, I. Staropoli, R. Altmeyer, J. L. Virelizier, F. Arenzana-Seisdedos, D. C. Hoessli, and F. Bachelerie, *HIV-1 entry into T-cells is not dependent on CD4 and CCR5 localization to sphingolipid-enriched, detergent-resistant, raft membrane domains*, J. Biol.

Chem. **278**, 3153 (2003).

[184] A. Cambi, F. de Lange, N. M. van Maarseveen, M. Nijhuis, B. Joosten, E. M. H. P. van Dijk, B. I. de Bakker, J. A. M. Fransen, P. H. M. Bovee-Geurts, F. N. van Leeuwen, N. F. van Hulst, and C. G. Figdor, *Microdomains of the C-type Lectin DC-SIGN are portals for virus entry into Dendritic Cells*, J. Cell Biol. **164**, 145 (2004).

[185] D. A. Brown and E. London, *Structure and function of sphingolipid- and cholesterol-rich membrane rafts*, J. Biol. Chem. **275**, 17221 (2000).

[186] Y. van Kooyk and C. G. Figor, *Avidity regulation of integrins: the driving force in leukocyte adhesion*, Curr. Opin. Cell Biol. **12**, 542 (2000).

[187] C. R. F. Monks, B. A. Freiberg, H. Kupfer, N. Sciaky, and A. Kupfer, *Three-dimensional segregation of supramolecular activiation clusters in T cells*, Nature **395**, 82 (1998).

[188] P. A. van der Merwe and S. J. Davis, *The immunological synapse- a multitasking system*, Science **295**, 1479 (2002).

[189] M. L. Dustin, *Membrane domains and the immunological synapse: keeping T cells resting and ready*, J. Clin. Invest. **109**, 155 (2002).

[190] K. H. Lee, A. R. Dinner, C. Tu, G. Campi, S. Raychaudhuri, R. Varma, T. N. Sims, W. R. Burack, H. Wu, O. Kanagawa, M. Markiewicz, P. M. Allen, M. L. Dustin, A. K. Chakraborty, and A. S. Shaw, *The immunological synapse balances T cell receptor signaling and degradation*, Science **302**, 1218 (2003).

[191] F. Lafont, G. T. van Nhieu, K. Hanada, P. Sansonetti, and F. G. van der Groot, *Initial steps of Shigella infection depend on the cholesterol/sphingolipid raft-mediated CD44-IpaB interaction*, EMBO J. **21**, 4449 (2002).

[192] J. Gatfield and J. Pieters, *Essential role for cholesterol in entry of mycobacteria into macrophages*, Science **288**, 1647 (2000).

[193] G. Vereb, J. Szollosi, J. Matko, P. Nagy, T. Farkas, L. Vigh, L. Matyus, T. A. Waldmann, and S. Damjanovich, *Dynamic, yet structured: The cell membrane three decades after the Singer Nicolson model*, Proc. Natl. Acad. Sci. U.S.A. **100**, 8053 (2003).

[194] M. Edidin, *Shrinking patches and slippery rafts: scales of domains in the plasma membrane*, Trends Cell Biol. **11**, 492 (2001).

[195] K. Simons and E. Ikonen, *Functional rafts in cell membranes*, Nature **387**, 569 (1997).

[196] J. C. Adams, *Molecular organisation of cell matrix contacts: essential multiprotein assemblies in cell and tissue*, Expert Rev. Mol. Med. 1 (2002).

[197] F. Sanchez-Madrid and M. A. del Pozo, *Leukocyte polarization in cell mi-*

gration and immune interactions, EMBO J. **18**, 501 (1999).

[198] D. J. Webb, C. M. Brown, and A. F. Horwitz, *Illuminating adhesion complexes in migrating cells: moving toward a bright future*, Curr. Opin. Cell Biol. **15**, 614 (2003).

[199] S. Damjanovich, L. Bene, J. Matko, A. Alileche, C. K. Goldman, S. Sharrow, and T. A. Waldmann, *Preassembly of interleukin 2 (IL-2) receptor subunits on resting Kit 225 K6 T cells and their modulation by IL-2, IL-7, and IL-15: A fluorescence resonance energy transfer study*, Proc. Natl. Acad. Sci. U.S.A. **94**, 13134 (1997).

[200] G. Vereb, J. Matko, G. Vamosi, S. M. Ibrahim, E. Magyar, S. Varga, J. Szollosi, A. Jenei, R. Gaspar, T. Waldmann, and S. Damjanovich, *Cholesterol-dependent clustering of IL-2Rα and its colocalization with HLA and CD48 on T lymphoma cells suggest their functional association with lipid rafts*, Proc. Natl. Acad. Sci. U.S.A. **97**, 6013 (2000).

[201] J. Matko, A. Bodnar, G. Vereb, L. Bene, G. Vamosi, G. Szentesi, J. Szollosi, R. G. jr, V. Horejsi, T. A. Waldmann, and S. Damjanovich, *GPI-microdomains (membrane rafts) and signaling of the multi-chain interleukin-2 receptor in human lymphoma/leukemia T cell lines*, Eur. J. Biochem. **269**, 1199 (2002).

[202] F. Murphy, C. Fauquet, A. J. M.A. Mayo, S. Ghabrial, M. Summers, G. Martelli, and D. Bishop, *Sixth Report of the International Committee on Taxonomy of Viruses - Archives of Virology*, Springer Verlag, Wien, New York (1995).

[203] universal virus database of the international committee on taxonomy of viruses, *http://www.ncbi.nlm.nih.gov/ICTVdb/*, 2003 .

[204] department of bacteriology university of wisconsin madison, *http://www.bact.wisc.edu*, 2003 .

[205] *http://www.mold.ph/candida.htm*, 2003 .

[206] B. M. Curtis, S. Scharnowske, and A. J. Watson, *Sequence and expression of a membrane-associated C-type lectin that exhibits CD4-independent binding of human immunodeficiency virus envelope glycoprotein gp120*, Proc. Natl. Acad. Sci. U.S.A. **89**, 8356 (1992).

[207] R. J. Kuhn, W. Zhang, M. G. Rossmann, S. V. Pletnev, J. Corver, E. Lenches, C. T. Jones, S. Mukhopadhyay, P. R. Chipman, E. G. Strauss, T. S. Baker, and J. H. Strauss, *Structure of Dengue Virus: Implications for Flavivirus organization, maturation, and fusion*, Cell **108**, 717 (2002).

[208] W. S. Hlavacek, R. G. Posner, and A. S. Perelson, *Steric effects on multivalent ligand-receptor binding: Exclusion of ligand sites by bound cell surface receptors*, Biophys. J. **76**, 3031 (1999).

[209] A. Chen and V. T. Moy, *Cross-linking of cell surface receptors enhances cooperativity of molecular adhesion*, Biophys. J. **78**, 2814 (2000).

[210] E. Betzig, *Proposed method for molecular optical imaging*, Optics Lett. **20**, 237 (1995).

[211] M. Heilemann, D. P. Herten, R. Heintzmann, C. Cremer, C. Muller, P. Tinnefeld, K. D. Weston, J. Wolfrum, and M. Sauer, *High-resolution colocalization of single dye molecules by fluorescence lifetime imaging microscopy*, Anal. Chem. **74**, 3511 (2002).

[212] M. F. Garcia-Parajo, M. Koopman, E. M. H. P. van Dijk, V. Subramaniam, and N. F. van Hulst, *The nature of fluorescence emission in the red fluorescent protein DsRed, revealed by single-molecule detection*, Proc. Natl. Acad. Sci. U.S.A. **98**, 14392 (2001).

[213] T. Vosch, M. Cotlet, J. Hofkens, K. van der Biest, M. Lor, K. Weston, P. Tinnefeld, M. Sauer, L. Latterini, K. Mullen, and F. C. de Schryver, *Probing Forster type energy pathways in a first generation rigid dendrimer bearing two Perylene Imide chromophores*, J. Phys. Chem. A **107**, 6920 (2003).

[214] J. Hernando, M. van der Schaaf, E. M. H. P. van Dijk, M. Sauer, M. F. Garcia-Parajo, and N. F. van Hulst, *Excitonic behavior of Rhodamine dimers: a single-molecule study*, J. Phys. Chem. A **107**, 43 (2003).

[215] T. Schmidt, G. J. Schutz, H. J. Gruber, and H. Schindler, *Local stoichiometries determined by counting individual molecules*, Anal. Chem. **68**, 4397 (1996).

[216] T. A. Fehniger, M. A. Cooper, and M. A. Caligiuri, *Interleukin-2 and interleukin-15: immunotherapy for cancer*, Cytokine Growth Factor Rev. **13**, 169 (2002).

[217] T. A. Waldmann, S. Dubois, and Y. Tagaya, *Contrasting roles of IL-2 and IL-15 in the life and death of lymphocytes: Implications for immunotherapy*, Immunity **14**, 105 (2001).

[218] J. P. Lodolce, P. R. Burkett, R. M. Koka, D. L. Boone, and A. Ma, *Regulation of lymphoid homeostasis by interleukin-15*, Cytokine Growth Factor Rev. **13**, 429 (2002).

[219] S. L. Gaffen, *Signaling domains of the interleukin 2 receptor*, Cytokine **14**, 63 (2001).

[220] M. J. Lenardo, *Fas and the art of lymphocyte maintenance*, J. Exp. Med. **183**, 721 (1996).

[221] D. M. Eicher, S. Damjanovich, and T. A. Waldmann, *Oligomerization of IL-2Rα*, Cytokine **17**, 82 (2002).

[222] J. G. Giri, S. Kumaki, M. Ahdieh, D. J. Friend, A. Loomis, K. Shanebeck,

R. DuBose, D. Cosman, L. S. Park, and D. M. Anderson, *Identification and cloning of a novel IL-15 binding protein that is structurally related to the alpha chain of the IL-2 receptor*, EMBO J. **14**, 3654 (1995).

[223] T. A. Waldmann, *The contrasting roles of IL-2 and IL-15 in the life and death of lymphocytes: implications for the immunotherapy of rheumatological diseases*, Arthritis Res. **4**, S161 (2002).

[224] T. A. Waldmann, R. Levy, and B. S. Coller, *Emerging therapies: spectrum of applications of monoclonal antibody therapy*, Hematology **1**, 394 (2000).

[225] A. Jenei and S. Damjanovich, *(personal communication)*, (2003).

[226] K. Simons and D. Toomre, *Lipid rafts and signal transduction*, Nat. Rev. Mol. Cell Biol. **1**, 31 (2000).

Summary

In the last decades, research in biology has developed towards progressively smaller scales and has now entered a nanoscale world where molecular interactions become visible, functioning of molecular motors can be measured, direction and speed of movement of molecules can be followed and protein structures are revealed. In parallel the required technologies, enabling to address, visualize and analyze molecules, follow the same trend of miniaturization. To investigate single molecules at ambient conditions, *in vitro* as well as *in vivo*, requires high resolution, molecular specificity and sensitivity. Near-field optics has the promise to fulfill these requirements. In this research we have developed a dedicated near-field scanning optical microscope (NSOM) for molecular biology and applied it to study the spatial organization of (fluorescently labeled) proteins at the cell surface. For the first time, protein clusters and individual molecules are resolved at the cell membrane with nanometer resolution using an optical method.

A short history of microscopy and its importance for cell biology is given in Chapter 1 of this thesis. Different types of fluorescence microscopy methodologies are described as well as their applicability for the investigation of biological specimens. In addition, an overview of available optical single molecule methods and their working principles is given. The spatial resolution of conventional optical microscopy methods is diffraction limited, allowing single molecule detection on an area with a low molecular density of only a few molecules per square micrometer. In addition, the relatively large depth of illumination (hundreds of nanometers) induces a large background contribution when studying cells. These problems are overcome by near-field optical techniques, where an exponentially decaying field illuminates the sample to a depth of below 100 nm. In NSOM a subwavelength aperture at the end of a sharp fiber probe is used as light source. In this way, the illumination volume is confined in three dimensions, resulting in the smallest possible illumination volume by optical means. The chapter is concluded with an overview of the human immune system, particularly focussing on the function of dendritic cells and T cells, placing the studied protein systems in a wider perspective.

Chapter 2 describes the technical details of the combined near-field/confocal scanning optical microscope. The microscope allows both near-field as well as a confocal type of illumination and has one sensitive detection path allowing single molecule detection in a polarization or wavelength dependent manner. The confocal part of the microscope is used to perform a quick pre-study of the sample and select an area for further in depth near-field investigation. In this chapter, the performance of the microscope is shown on the basis of measurements of fluorescently labeled molecules on cells, demonstrating three main advantages of NSOM over confocal microscopy in cell studies: 1) NSOM provides a high localization accuracy and spatial resolution, allowing to distinguish molecular entities in densely packed systems; 2) NSOM has a low penetration depth, avoiding intracellular autofluorescence; 3) NSOM provides simultaneous optical and topographical information. These advantages have been exploited in the following chapters for studying different types of proteins on the membrane of intact cells at the single molecular level.

In Chapter 3 the spatial organization of proteins (DC-SIGN) on the cell membrane of immature dendritic cells (imDCs) is investigated. These cells bind different types of pathogens such as viruses and bacteria, using DC-SIGN. We have investigated the spatial organization of DC-SIGN on the membrane as this is thought to be related to the pathogen binding capability of the cell. Near-field optical images of DC-SIGN proteins, labeled via antibodies with Cy5, show a full coverage of the membrane with individual fluorescent spots of variable intensities. Amongst the large number of spots, only a few show single molecule emission. The typical single molecule intensity of Cy5 molecules is measured and used to relate the intensity of each fluorescent spot to the number of Cy5 molecules present at that location. The spots contain from 1 to over 200 Cy5 molecules and more than 80 % of all spots are molecular domains. Despite the large variety in molecular content, the distribution of measured domain sizes is rather narrow and peaks at 200 nm. Correlation of the domain sizes with the number of molecules in each domain reveals a large variety in molecular density. Assuming an average labeling efficiency of 3.5 Cy5 molecules per antibody - which is explicitly measured in Chapter 5 - and a one to one ratio between antibody and protein, the average nearest neighbor distance (*nnd*) between DC-SIGN proteins within a domain is estimated to be 39 nm. Distances between the domains indicate a random domain distribution pattern. Thus, we have recognized a two-layer hierarchical organization of DC-SIGN spacing, where DC-SIGN resides in domains (layer 1), which are randomly spread (layer 2). As DC-SIGN binds to various pathogens with different affinities, we hypothesize that 1) DC-SIGN makes use of variable molecular densities to allow binding to different types of pathogens; 2) DC-SIGN domains are randomly distributed to maximize the probability of hitting a pathogen in an accidental encounter of a cell and a pathogen.

Clustering of membrane molecules into domains, such as found in Chapter 3, is a common phenomenon in cell biology and known to facilitate specific cell functions. In chapter 4 a simple, two-dimensional model is introduced to explain the advantages of clustering and investigate the importance of domain size and molecular packing density in a domain. The model describes the probability for an object of certain size hitting a minimum number of receptor molecules on the cell membrane in an accidental object-cell encounter. We have introduced Monte Carlo simulations, enabling the use of distributions of domain properties. We have performed simulations using realistic numbers for the domain properties and investigated the binding capabilities of the immature dendritic cell. Using a constant total number of surface molecules and various types of spatial organization, the simulations show that 1) domains are beneficial over a random spread of individual molecules if more than a specific number of hits is needed in an encounter to obtain a stable object-cell bond; 2) domain properties are particularly important for the hit probability if the object size is comparable to the domain size; 3) the origin of molecular packing density, given either by domain size or domain content, is important to achieve a high hit probability if the object is larger than the domain; 4) an optimum exists for the spatial distribution of receptor molecules to bind objects of specific size with a specific number of receptors in the object-cell contact area. Simulations including distributions of the domain properties of DC-SIGN show that the wide spread in domain content ensures a larger number of hit receptors compared to an area with domains having one average size and content. Moreover, the spatial organization of DC-SIGN seems to be optimized for small virus-like objects.

In Chapter 5, the sudden termination of single molecule fluorescence, i.e. discrete photobleaching, is used as a specific time dependent single molecule property to count the number of fluorophores and localize fluorophores within densely packed areas. The labeling efficiency of Cy5-labeled antibodies was determined by recording the fluorescence emission from the densely packed Cy5 fluorophores in time and counting the number of discrete photobleaching steps. Similar time dependent studies on densely packed molecular domains show first a bulk-like exponential decay of the fluorescence intensity. Because the decrease in intensity is accompanied by a decrease in shot noise, discrete photobleaching steps of the remaining fluorophores can be counted when the shot noise falls below the signal level of a single molecule. Photobleaching is further exploited by counting and localizing single molecules in an area of densely packed fluorophores. Using NSOM, the area is sequentially imaged. As the fluorophore density decreases in each image, single fluorophores become gradually visible, which enables to count them as well as to pinpoint them individually. This method reveals the real spatial distribution of fluorophores and unravels the molecular composition of domains.

In Chapter 6, the spatial organization of membrane proteins on T cells is investigated. The proteins of interest are IL-2Rα and IL-15Rα, subunits of the Interleukin receptor trimers IL-2R and IL-15R, respectively. These receptors perform a distinct function for the cell from the DC-SIGN proteins studied in Chapter 3. IL-2R and IL-15R bind specifically to Interleukins IL-2 and IL-15, respectively. Upon binding, signals are transmitted to the T cell, stimulating cell growth, cell differentiation and cell death. Interestingly, although both receptors are structurally similar, sometimes they seem to have contrasting effects on the course of life of a T cell. We have studied the α-subunits because they are thought to be essential for these contrasting effects. Near-field fluorescence images of Cy5-labeled IL-2Rα and IL-15Rα show domains as well as individual entities on the cell surface. Also single Cy5 molecules are visible, allowing to build a single molecule intensity distribution which is used to relate the intensity to the number of present Cy5 molecules. For both IL-2Rα and IL-15Rα, the intensity distributions of all fluorescent spots show two populations, i.e. one consisting of single proteins and the other of protein domains. This quantitative analysis also reveals the number of molecules residing within and outside domains. The domains of IL-2Rα and IL-15Rα are similar in size having a rather constant diameter of about 400 nm. Dual color near-field experiments show that IL-2Rα and IL-15Rα co-localize on the membrane, which is thought to be essential for the signaling capability of both IL-2R and IL-15R. A fundamental difference between the IL-2Rα/IL-15Rα and DC-SIGN domains is found when correlating domain size with number of proteins within the domain. Namely, both IL-2Rα and IL-15Rα show a constant molecular packing density for all domains of 1350 IL-2Rα/μm^2 and 120 IL-15Rα/μm^2, respectively. This difference in spatial organization for adhesion and signaling molecules indicates the close structure-function relation between spatial membrane organization and cell function.

This thesis shows the value of near-field scanning optical microscopy combined with single molecule sensitivity for cellular and molecular biology. In addition, it shows the possible ways to exploit this technique for revealing the nanometric organization of molecules on the cell membrane.

Samenvatting

In de afgelopen decennia is biologisch onderzoek zich steeds meer gaan richten op processen die zich afspelen op de micrometer - en zelfs nanometerschaal. Dit heeft ervoor gezorgd dat moleculaire interacties zichtbaar kunnen worden gemaakt, krachtinteracties van moleculaire motoren kunnen worden gemeten, moleculaire bewegingen kunnen worden gevolgd in tijd en ruimte, en moleculaire structuren kunnen worden ontrafeld. Tegelijkertijd volgen de hiervoor benodigde technologieën eenzelfde miniaturisatietrend, die het mogelijk heeft gemaakt om individuele moleculen afzonderlijk te adresseren, te visualiseren en te analyseren. Om individuele moleculen te onderzoeken onder normale omgevingscondities zijn een hoge resolutie, moleculaire specificiteit en een hoge gevoeligheid van de meetmethode noodzakelijk. Nabije-veld optica heeft de potentie om aan deze voorwaarden te voldoen. In het hier gepresenteerde onderzoek is een nabije-veld scannende optische microscoop (NSOM) ontwikkeld voor moleculair biologisch onderzoek. Met deze microscoop is de ruimtelijke organisatie van (fluorescent gemarkeerde) proteïnes aan het celoppervlak onderzocht. Voor de allereerste keer zijn met behulp van een optische methode proteïneclusters en afzonderlijke moleculen op het celoppervlak met nanometer resolutie zichtbaar gemaakt.

Hoofdstuk 1 beschrijft in het kort de geschiedenis van de microscopie en het belang van deze onderzoeksmethode voor de celbiologie. Verscheidene vormen van fluorescentiemicroscopie worden beschreven evenals hun toepassingsmogelijkheden voor onderzoek aan biologische preparaten. Tevens wordt een overzicht gegeven van beschikbare optische methoden voor het detecteren van individuele moleculen. Het oplossend vermogen van conventionele optische microscopie is diffractie gelimiteerd, waardoor detectie van individuele moleculen alleen mogelijk is op een dunbevolkt gebied met een dichtheid van slechts enkele moleculen per vierkante micrometer. Daarnaast zorgt de relatief grote optische indringdiepte (honderden nanometers) voor een hoge achtergrond bij het bestuderen van cellen. Deze problemen zijn oplosbaar door nabije-veld optische technieken te gebruiken, waarbij een exponentieel afnemend optisch veld het preparaat belicht tot een diepte van minder dan honderd nanometer. In NSOM wordt een kleine opening aan het uiteinde van een scherpe glasvezeltip als lichtbron gebruikt. Hierdoor is het belichtingsvolume in drie dimensies begrensd en tevens het kleinst haalbare in optische microscopie. Het hoofdstuk eindigt met een overzicht van het menselijke immuunsysteem, waarbij in het bijzonder aandacht gegeven wordt aan het functioneren van dendritische- en T cellen, om op die manier de hier onderzochte proteïnesystemen in een breder perspectief te plaatsen.

Hoofdstuk 2 geeft de technische beschrijving van de ontwikkelde nabije-veld - confocaal scannende optische microscoop. Met de microscoop kan het preparaat zowel in het nabije-veld als confocaal worden belicht. Er is één gezamenlijk detectiekanaal waarmee de fluorescentie van een individueel molecuul zowel polarisatie - als golflengtegevoelig gemeten kan worden. Met behulp van confocale microscopie kan een snel vooronderzoek van het preparaat gedaan worden en een gebied voor verder diepgaand nabije-veld onderzoek worden geselecteerd. In dit hoofdstuk wordt de prestatie van de microscoop beschreven aan de hand van metingen aan fluorescent gemarkeerde moleculen die zich op het oppervlak van een cel bevinden. Hieruit volgen drie belangrijke voordelen van NSOM ten opzichte van confocale microscopie bij cel onderzoek: 1) NSOM heeft een hoge lokalisatienauwkeurigheid en optische resolutie, waarmee het mogelijk wordt om moleculen in dichtbevolkte systemen te onderscheiden; 2) NSOM heeft een kleine indringdiepte, waardoor intracellulaire autofluorescentie wordt geminimaliseerd; 3) NSOM geeft tegelijkertijd optische - en topografische informatie. In de volgende hoofdstukken worden deze voordelen benut voor het bestuderen van verschillende membraanproteïnes op het niveau van individuele moleculen.

In hoofdstuk 3 is de ruimtelijke verdeling van een bindingsproteïne (DC-SIGN) op het celmembraan van onvolgroeide dendritische cellen (imDCs) onderzocht. Deze cellen binden met behulp van dit proteïne aan ziekteverwekkers zoals virussen en bacteriën. Wij hebben de ruimtelijke organisatie van DC-SIGN, die mogelijk verband houdt met de bindingscapaciteit van de cel, onderzocht. De DC-SIGN proteïnes zijn fluorescent gemarkeerd via antilichamen met Cy5. Optisch nabije-veld metingen van DC-SIGN laten afzonderlijke fluorescerende vlekken op het celmembraan zien die variëren in intensiteit. Slechts enkele van de vele fluorescerende vlekken kunnen worden toegekend aan de emissie van een individueel molecuul. De gemeten emissie van een enkel Cy5 molecuul wordt gebruikt om de intensiteit van elke fluorescerende vlek te relateren aan het aantal Cy5 moleculen op die plaats. De vlekken bevatten tussen 1 en 200 Cy5 moleculen en het merendeel ($> 80\,\%$) van alle vlekken zijn moleculaire clusters met meer dan tien moleculen. Ondanks de grote verscheidenheid in moleculaire bezetting, is de verdeling van de gemeten clustergroottes redelijk smal met een typische clustergrootte van ongeveer 200 nanometer. Een grote verscheidenheid in moleculaire dichtheid wordt zichtbaar door de clustergrootte en het aantal moleculen binnen een cluster te correleren. Uitgaande van een gemiddelde markeerefficiëntie van 3.5 Cy5 moleculen per antilichaam wordt aangenomen - wat expliciet gemeten wordt in Hoofdstuk 5 - en een één-op-één verhouding tussen antilichaam en proteïne, wordt de gemiddelde 'naaste - buur' afstand (*nnd*) tussen DC-SIGN proteïnes binnen een cluster geschat op 39 nm. De onderlinge clusterafstanden geven aan dat de clusters willekeurig verdeeld zijn. Hiermee hebben we een hiërarchische structuur met twee lagen in de ruimtelijke verdeling van DC-SIGN ontdekt, waarin DC-SIGN clustert in clusters (laag 1), die willekeurig verdeeld zijn op het cel oppervlak (laag 2). Omdat DC-SIGN met verschillende affiniteit aan verschillende ziekteverwekkers bindt, veronderstellen we dat 1) DC-SIGN gebruik maakt van variërende moleculaire dichtheden binnen de clusters om te kunnen binden met verschillende ziekteverwekkers; 2) DC-SIGN clusters willekeurig verdeeld zijn op het oppervlak om de kans op het raken van een ziekteverwekker, in een toevallige ontmoeting tussen de cel en de ziekteverwekker, te maximaliseren.

Het clusteren van membraanmoleculen, zoals beschreven in Hoofdstuk 3, is een veelvoorkomend verschijnsel in de celbiologie, waarvan het bekend is dat het specifieke celfuncties mogelijk maakt. In Hoofdstuk 4 wordt een eenvoudig tweedimensionaal model geïntroduceerd om de voordelen van clusteren uit te leggen en het belang van clustereigenschappen, zoals clustergrootte en moleculaire dichtheid, voor de bindingseigenschappen van een cel te onderzoeken. Het model beschrijft de kans waarop een object (virus of bacterie) met een gegeven grootte een minimum aantal bindingsreceptoren (membraanmoleculen) raakt in een toevallige ontmoeting tussen object en cel. De bindingssterkte tussen object en cel neemt toe met het aantal receptoren dat geraakt wordt. Wij hebben Monte Carlo simulaties geïntroduceerd, die het mogelijk maken om naast vaste simulatieparameters, zoals clustergrootte en moleculaire dichtheid, ook met verdelingen van clustereigenschappen te simuleren. We hebben simulaties uitgevoerd met realistische, gemeten waarden voor de eigenschappen van DC-SIGN clusters en hebben de bindingscapaciteit van de dendritische cel onderzocht. Simulaties met een constant totaal aantal receptormoleculen en verschillende soorten ruimtelijke verdelingen, laten zien dat 1) clustervorming gunstiger is dan een willekeurige verdeling van individuele moleculen indien er meer dan een bepaald aantal rakende moleculen nodig zijn voor het verkrijgen van een stabiele object-cel verbinding; 2) clustereigenschappen van grote invloed zijn op de raakkans als de grootte van het object vergelijkbaar is met de grootte van de clusters; 3) de manier waarop de cel een bepaalde moleculaire dichtheid creëert, door clustergrootte of clusterinhoud aan te passen, de raakkans beïnvloedt wanneer het object kleiner is dan het domein; 4) er een optimale ruimtelijke verdeling is van receptor moleculen in een cluster om objecten van een specifieke grootte te binden met een bepaald aantal receptoren in het contact vlak tussen object en cel. Simulaties waarin verdelingen van DC-SIGN clustereigenschappen worden meegenomen, laten zien dat de grote spreiding in receptordichtheid binnen een cluster de cel verzekert van een groot aantal rakende receptoren in vergelijking met een oppervlak dat clusters met een constante grootte en dichtheid bevat. Daarbij lijkt de ruimtelijke verdeling van DC-SIGN geoptimaliseerd voor kleine virusachtige objecten.

In hoofdstuk 5 wordt de plotselinge emissiestop van een individueel molecuul, 'discrete fotodissociatie' of 'bleking' genoemd, gebruikt als een tijdafhankelijke eigenschap van individuele moleculen om het aantal fluorescerende moleculen te tellen en hun posities te bepalen. We hebben fotodissociatie gebruikt om de markeringsefficiëntie van antilichamen met Cy5 moleculen te bepalen door een tijdopgeloste fluorescentiemeting te doen en het aantal discrete fotodissociatie stappen te tellen. Vergelijkbare tijdafhankelijke metingen van dichtgepakte moleculaire clusters laten in het begin een exponentiële afname van de fluorescentie zien. Omdat de intensiteitafname samen gaat met een afname in fotonruis, kunnen discrete fotodissociatie stappen worden geteld zodra de ruis kleiner dan het emissieniveau van een individueel molecuul wordt. Fotodissociatie is verder toegepast bij het tellen en lokaliseren van individuele moleculen in een dichtbevolkt gebied van fluorescerende moleculen. Hiervoor is met behulp van NSOM herhaaldelijke keren over hetzelfde gebied gescand. Terwijl in elk plaatje de dichtheid van fluorescerende moleculen door fotodissociatie afneemt, worden individuele moleculen geleidelijk zichtbaar, zodat ze uiteindelijk afzonderlijk geteld en nauwkeurig ge-lokaliseerd kunnen worden. Deze methode onthult de echte ruimtelijke verdeling van fluorescerende moleculen en ontrafelt de moleculaire samenstelling van clusters.

In hoofdstuk 6 wordt de ruimtelijke organisatie van membraanproteïnes op T cellen onderzocht. De onderzochte proteïnes zijn IL-2Rα en IL-15Rα, die een onderdeel zijn van de respectievelijke receptoren IL-2R en IL-15R. Deze membraanproteïnes hebben heel andere functies voor de cel dan de DC-SIGN proteïnes uit Hoofdstuk 3. IL-2R en IL-15R binden specifiek aan Interleukin moleculen IL-2 en IL-15. Voor beide receptoren geldt dat bij binding signalen worden afgegeven aan de T cel die celgroei, celdeling maar ook celsterfte kunnen stimuleren. Hoewel beide receptoren wat structuur betreft vergelijkbaar zijn, lijken ze soms een tegengesteld effect te hebben op de levensloop van een T cel. We hebben specifiek de α proteïnes onderzocht omdat zij een essentiële rol lijken te spelen bij deze effecten. Optische nabije-veld metingen van met Cy5 gemarkeerde IL-2Rα en IL-15Rα proteïnes laten zowel proteïne clusters als individuele proteïnes op het celoppervlak zien. Ook individuele Cy5 moleculen zijn zichtbaar, waarmee het typische emissieniveau van een individueel Cy5 molecuul kan worden afgeleid. Dit wordt gebruikt om een gemeten cluster intensiteit te relateren aan het aantal aanwezige Cy5 moleculen. De intensiteitverdelingen van zowel IL-2Rα als IL-15Rα laten twee populaties zien; één bestaande uit individuele proteines en de andere bestaande uit clusters. Deze kwantitatieve analyse onthult ook het aantal moleculen dat zich binnen en buiten de clusters bevindt. De clusters van IL-2Rα en IL-15Rα zijn vergelijkbaar in grootte en hebben een redelijk constante diameter van typisch ongeveer 400 nm. Tweekleuren nabije-veld experimenten laten zien dat IL-2Rα en IL-15Rα clusters colokaliseren op het membraan, wat waarschijnlijk gerelateerd is met hun soms tegengestelde rol in celsignalering. Hoewel IL-2Rα/IL-15Rα net als DC-SIGN clusters vormen op het celmembraan is er een groot verschil tussen beide vormen van clusters. Dit komt aan het licht bij correlatie van de clustergrootte met het aantal proteïnes in het cluster. Zowel IL-2Rα en IL-15Rα hebben een constante moleculaire dichtheid voor alle clusters van respectievelijk 1350 IL-2Rα/μm^2 en 120 IL-15Rα/μm^2. In tegenstelling daarmee laten DC-SIGN clusters een grote spreiding zien in moleculaire dichtheid. Dit verschil in ruimtelijke verdeling tussen bindings- en signaleringsmoleculen is waarschijnlijk te wijten aan de specifieke functie van beide soorten moleculen.

Dit proefschrift laat de waarde zien van nabije-veld scannende optische microscopie gecombineerd met individuele moleculaire gevoeligheid voor cellulaire en moleculaire biologie. Het geeft bovendien inzage in de mogelijke manieren om deze techniek te benutten voor het onthullen en bestuderen van de ruimtelijke verdeling op nanometerschaal van moleculen op het celoppervlak.